INFORMATION TO USERS

This material was produced from a microfilm copy of the original document. While the most advanced technological means to photograph and reproduce this document have been used, the quality is heavily dependent upon the quality of the original submitted.

The following explanation of techniques is provided to help you understand markings or patterns which may appear on this reproduction.

1. The sign or "target" for pages apparently lacking from the document photographed is "Missing Page(s)". If it was possible to obtain the missing page(s) or section, they are spliced into the film along with adjacent pages. This may have necessitated cutting thru an image and duplicating adjacent pages to insure you complete continuity.

2. When an image on the film is obliterated with a large round black mark, it is an indication that the photographer suspected that the copy may have moved during exposure and thus cause a blurred image. You will find a good image of the page in the adjacent frame.

3. When a map, drawing or chart, etc., was part of the material being photographed the photographer followed a definite method in "sectioning" the material. It is customary to begin photoing at the upper left hand corner of a large sheet and to continue photoing from left to right in equal sections with a small overlap. If necessary, sectioning is continued again — beginning below the first row and continuing on until complete.

4. The majority of users indicate that the textual content is of greatest value, however, a somewhat higher quality reproduction could be made from "photographs" if essential to the understanding of the dissertation. Silver prints of "photographs" may be ordered at additional charge by writing the Order Department, giving the catalog number, title, author and specific pages you wish reproduced.

5. PLEASE NOTE: Some pages may have indistinct print. Filmed as received.

Xerox University Microfilms

300 North Zeeb Road
Ann Arbor, Michigan 48106

76-30,417

MCQUADE, Arthur W., 1942-
EXPERIMENTAL INVESTIGATION OF ANOMALOUS ABSORPTION OF ELECTROMAGNETIC WAVES IN A MAGNETIZED PLASMA.

City University of New York, Ph.D., 1976
Physics, fluid and plasma

Xerox University Microfilms, Ann Arbor, Michigan 48106

EXPERIMENTAL INVESTIGATION OF ANOMALOUS ABSORPTION OF ELECTROMAGNETIC WAVES IN A MAGNETIZED PLASMA

by

ARTHUR W. MCQUADE

A dissertation submitted to the Graduate Faculty in Physics in partial fulfillment of the requirements for the degree of Doctor of Philosophy, The City University of New York.

1976

This manuscript has been read and accepted for the Graduate Faculty in Physics in satisfaction of the dissertation requirement for the degree of Doctor of Philosophy.

6/30/76
Date

L. G. Ferrari
Chairman of Examining Committee

7/7/76
Date

Myriam P. Sarachik
Executive Officer

Lee Bienenstock

Wayne E. Cox

Supervisory Committee

The City University of New York

ABSTRACT

A left circularly polarized electromagnetic wave (f = 2.45GHz) is launched into an overdense electron cyclotron plasma ($n \approx 2 \times 10^{11}$ cm^{-3}, $T_e \approx 8$eV). The wave is observed to be anomalously transmitted for a period of time after which it is essentially completely absorbed with a concurrent increase in electron temperature of up to 50%. At the time of absorption, radio frequency probe measurements indicate the excitation of electrostatic plasma waveguide modes at frequencies both below the electron cyclotron plasma frequency and above the electron plasma frequency. Measurements of the frequencies, wavenumbers and azimuthal orders were made and have identified these waves as Gould - Trivelpiece type modes. The excitation and subsequent damping of these modes is interpreted to be the mechanism for the absorption of the incident left wave.

TABLE OF CONTENTS

TABLE OF CONTENTS (CONTINUED)

I - INTRODUCTION

The study of the propagation of electromagnetic waves in plasma has recently received much attention. Radio frequency plasma heating where electromagnetic energy is converted into thermal motion of charged particles is of interest because of its application in controlled thermonuclear fusion experiments; therefore, it is important to understand the mechanism by which electromagnetic waves can be absorbed and transfer their energy to a plasma. We thusly begin with a brief review of electromagnetic wave propagation in a magnetized plasma.

In general, when a high frequency electromagnetic wave is incident on a magnetized unbounded plasma, the resulting dispersion relation can be very complex and predicts several modes of propagation.[1] However, we will only consider propagation along the uniform static field $\vec{B}_o = B_o\hat{z}$. Under these circumstances the dispersion relation simplifies and three possible modes result. One of these describes longitudinal plasma oscillations at the plasma frequency. The other two modes are left and right hand circularly polarized electromagnetic waves. The dispersion relations for these modes propagating in a cold unbounded plasma parallel to $\vec{B}_o$ are given by[1]

$$\frac{c^2 k_{L,R}^2}{\omega^2} = n_{L,R}^2 = 1 - \frac{\omega_p^2/\omega^2}{\left(1 \mp \frac{\omega_{ci}}{\omega}\right)\left(1 \pm \frac{\omega_{ce}}{\omega}\right)} \qquad (1)$$

with the upper choice of signs for the left wave and lower signs for the right hand mode. The subscripts on the cyclotron frequency $\omega_c = |eB_o/m|$ refer to the ions and electrons while the plasma frequency $\omega_p^2 = \omega_{pe}^2 + \omega_{pi}^2$ can be just taken as $\omega_p^2 = ne^2/m_e\epsilon_o$ because of the large mass differences between the two species.

Examination of the dispersion relation near the electron cyclotron frequency i.e. $\omega_{ci} \ll \omega \simeq \omega_{ce}$ reveals several interesting features. If $\omega_{ce}/\omega < 1$ and $\omega_p/\omega < 1$ the right hand wave can propagate for large values of ω, but as ω decreases and approaches the value such that $\omega_{ce}/\omega = 1 - (\omega_p/\omega)^2$ then the refractive index n_R approaches zero and the wave is reflected.[2] If however $\omega_p/\omega > 1$, the index of refraction is always imaginary and the wave is cutoff. When $\omega_{ce}/\omega > 1$ the wave can propagate for all frequencies, but as ω approaches ω_{ce}, the refractive index diverges and the wave undergoes resonance at this point. Thus a wave can propagate from a high field to a low field region and if the magnetic field variation is such that $\omega_{ce} = \omega$ at some point, the perpendicular energy of the electron is irreversibly increased and the wave is absorbed through this energy transfer. This type of arrangement is known as a magnetic beach[3] and the electron cyclotron damping of the right hand component of the incident wave with the electrons is the method used to create plasma in this experiment.

In a similar manner the left wave will resonant with the ions when $\omega = \omega_{ci}$, however at frequencies near the electron cyclotron frequency, the dispersion relation simply predicts that this wave will either pro-

pagate or be reflected depending on whether ω_{ce}/ω is respectively greater or less than $(\omega_p/\omega)^2 - 1$.

In a warm plasma, thermal effects influence the wave propagation. The primary effect of finite temperature is that now the electrons will experience a Doppler shifted frequency $\omega - k_z v_z$ and thus resonance can occur for any electron with the appropriate $T_{||}$. Also, whereas in cold plasma theory all the electrons were in phase with the incident wave, now thermal motions will cause the electron to be out of phase. As a result of these warm plasma effects, the cold plasma behavior must be modified. Now the index of refraction for the right wave n_R does not diverge at resonance but rather warm theory predicts a minimum value of λ ; this is because not all the electrons are participating in the resonance. In the solution of the warm plasma dispersion relation, an integral with a simple pole at $\omega - k_z v_z = \omega_c$ is obtained and thus k_z is complex and subsequently the waves can now undergo growth or damping. There is thus a mechanism for cyclotron damping in a warm plasma which did not exist in the cold theory.

The above discussion treated the case of an infinite plasma in which any boundary effects were neglected. In the present experiment, a wave is launched from a rectangular waveguide into a vacuum chamber, the inside of which has a stainless steel liner. Since this liner acts as a cylindrical waveguide, the effects on the modes of propagation and the cutoff frequencies must be considered when the appropriate boundary conditions are applied. This problem of wave propagation in a plasma

filled cylindrical waveguide has been treated by Bers [4]. It is noted that the effect of the boundaries is to increase the plasma cutoff frequency or, at a fixed frequency to cause cutoff at a lower density than for the unbounded case.

The problem of wave absorption at the resonance zone is an important one and several theories have been proposed in an attempt to understand this problem. Kuckes [5] approached this problem by explicitly considering the particle motion in a non-uniform magnetic field near the resonant region and constructed self consistent wave solutions in which the wavenumber depends upon position. He found that away from the resonant zone the plasma obeys the cold plasma relations, but near the plane of resonance it was necessary to add a resistive sheet to his model. At low densities the wave is relatively unaffected and it is transmitted except for a small amount of energy which is absorbed by the sheet, but at higher densities it is expected that the conductivity of the resonant region would increase, thus reducing the problem to that of an electromagnetic wave incident upon a perfect conductor. This should result in the complete reflection of the waves; however, his calculations predict that the wave is not reflected and that above a certain critical density complete absorption takes place.

Brambilla [6] took a similar self consistent approach to the problem, but obtained the result that at most 50% of the wave is absorbed. This is in direct variance with Kuckes calculation. However in a later report [7] Brambilla modified his calculations now giving results more consistent with

those of Kuckes. Now, the "current sheet" model was extended to include non-linear effects which modify the electron motion in the resonant region. It is found that these effects give rise to reflection of the wave from the resonant plane, thus limiting the absorption. Only at higher densities does the absorption result of the linear regime hold because the field is decreased in the resonant region. Therefore at high power levels, the wave energy is effectively coupled to the plasma only if the density is high enough to reduce the intensity of the electric field in the resonant region to a level such that the linear theory applies.

There have also been several experiments performed to investigate wave absorption in both electron and ion cyclotron plasma. For most experiments involving ion cyclotron resonance, the waves were launched with a "Stix coil" [8] and propagated into a magnetic beach where plasma heating in the resonant zone was studied. An example of this was the experiment performed by Uman and Hooke [9] where they used magnetic probes to measure the relative wave amplitude and phase ahead of the resonant zone. Although their measurements showed reasonable agreement with theory, their results cannot be deemed conclusive because the large experimental error allows the data to fit the theoretical predictions even when the latter varies by a factor of two. It is also noted from the design of the magnetic probes that any decrease in B_z can be interpreted as cyclotron absorption and in addition no account was made of any mode conversion effects nor were any results regarding the fraction of power absorbed reported.

More recently electron cyclotron resonance has been used as a method to heat a hot electron plasma [10]. This method has been used at Oak Ridge [11, 12] in mirror machines as well as in the Tokamak T M-3 at Kurchatov [13]. For the most part electron resonance experiments are primarily concerned with heating, i.e., they try to maximize the perpendicular plasma pressure $nkT_{\perp}$, the diamagnetism or the X-ray emission by varying the magnetic field and gas pressure; little attention is given to the details of the wave propagation.

In the experiments reported in this thesis we observe the cyclotron absorption of the right hand wave but in addition, the non-resonant left wave (to which the plasma is overdense) is also observed to be almost completely absorbed. Absorption of electromagnetic radiation under these circumstances is of interest because of its applications in laser fusion. [14]

Several years ago Gekker and Sizukhin [15] reported a similar non-resonant anomalous absorption. They measured the reflection coefficient of an electromagnetic wave incident on an overdense plasma in a cylindrical waveguide. At low power levels ($E_o << 100$ V/cm) they found that the wave was completely reflected in agreement with cold plasma theory, but as the wave electric field was increased beyond 100 V/cm both the reflection and transmission of the wave decreased indicating anomalous absorption. Unfortunately, no measurements were made of either the field or density distribution within the plasma.

Kaw, Valeo, and Dawson [16] interpreted the above anomalous absorption as being caused by a parametric instability in which the incident

wave of frequency ω_1, decays into an electron plasma wave of frequency ω_2 and an ion acoustic wave of frequency ω_3. The electron plasma wave then transfers its energy to the plasma by Landau damping[17]. In order for such a decay to take place, the parametric selection rules[18] must be obeyed, namely

$$\omega_1 = \omega_2 + \omega_3 \tag{2}$$

$$\vec{k}_1 = \vec{k}_2 + \vec{k}_3 \tag{3}$$

$$m_1 = m_2 + m_3 \tag{4}$$

where the $\vec{k}$ is the propagation constant and the m is the azimuthal mode order. This interpretation of the anomalous absorption has not been verified as no observation of the excited plasma and ion acoustic waves was made by Gekker and Sizukhin.

Since the original experiment of Gekker and Sizukhin, several reports of anomalous absorption have appeared in the literature. In 1971 Demirkhanov et al[19], investigated the behavior of a highly ionized plasma in which a longitudinal high frequency current flowed. They observed that for frequencies close to the plasma frequency, the high frequency power is effectively absorbed and collisionless plasma heating results. They interpret their results as apparently due to the development of high frequency plasma waves under conditions of parametric resonance.

Sergeichen and Trofimov[20] studied the effects of wave absorption and electron heating in a uniform plasma layer. Their experiment was

performed with a uniform density plasma stream traversing a rectangular waveguide perpendicular to the broad wall. They measured the absorption and reflection coefficients with electric fields varying from 1V/cm to 7kV/cm for different concentration of particles. The measurements show that there is a simultaneous heating of the electrons with the absorption of the microwave energy and this anomalous dissipation of power is characterized by large values of an effective collision frequency of at least three or four orders higher than the electron - ion collision frequency. The average effective collision frequency was found to increase as E_o^2 and possibly even more rapidly.

In similar experiments, Batanov and Sarksyan[21], Chu and Hendel[22], and Dreicer et al[23], all find similar results. They report anomalous absorption of microwaves at frequencies close to the plasma frequency which is interpreted as due to a parametric decay instability.

In the experiments reported here a linearly polarized electromagnetic wave (f = 2.45 GHz) is launched into a cylindrical waveguide from a high field to low field mirror geometry. The right hand component of the incident wave produces plasma via electron cyclotron resonance. For typical densities obtained here ($n \simeq 2 \times 10^{11} cm^{-3}$) the left wave should be cutoff; however, it is initially observed to propagate for a short period of time following the beginning of the incident power pulse. Dynamic measurements of the density and electromagnetic field profiles during this period of anomalous transmission show that both the density and field distributions evolve from the expected peaked on axis profiles to

annular configurations.

In addition, following this period of transmission, the left wave is observed to be almost completely non-resonantly absorbed with a concurrent increase in electron temperature of up to 50%.

At the time of this anomalous absorption, RF probe measurements indicate the excitation of electrostatic waveguide modes at frequencies both below the electron cyclotron frequency and above the electron plasma frequency. Measurements of the frequencies, wavenumbers and azimuthal orders are presented. The results indicate that these modes are of the type discovered by Gould and Trivelpiece [24].

1 - REFERENCES

1. G. Schmidt, Physics of High Temperature Plasmas, Academic Press (1966) pp. 230-237.

2. J. Stix, The Theory of Plasma Waves, McGraw-Hill Book Co. (1962) pp. 235-240.

3. J. Stix, Physics of Fluids, 1, 308 (1958).

4. W. P. Allis, S. J. Buchsbaum, and A. Bers, Waves in Anisotropic Plasmas, M.I.T. Press, Cambridge, Mass., (1963), Chapters 9 and 10.

5. A. F. Kuckes, Plasma Physics, 10, 367 (1968).

6. M. Brambilla, Plasma Physics, 10, 359 (1968).

7. M. Brambilla, Nuclear Fusion, 9, 343 (1969).

8. R. M. Sinclair, M. A. Rothman, J. C. Hosea, Plasma Physics, 12, 639 (1970).

9. M. F. Uman and W. M. Hooke, Princeton University Plasma Physics Lab., Report Matt 634, August 1968.

10. O. Eldridge, Proceedings of the First Topical Conference on RF Plasma Heating, Texas Tech University, July 6-8, 1972.

11. R.A. Dandl et al, Nuclear Fusion 4, 344 (1964).

12. W.B. Ard et al, Physical Review Letters 10, 87 (1963).

13. V.V. Alikaev et al, Plasma Physics 10, 753 (1968).

14. N.A. Amherd and G.C. Vlases, Applied Physics Letters 24, 93 (1974).

15. I.R. Gekker and O.V. Sizukhin, JETP Letters 9, 243 (1969).

16. P. Kaw, E. Valeo, and J.M. Dawson, Phys. Rev. Letters 25, 430 (1970).

17. L. Landau, J. Phys. U.S.S.R. 10, 25 (1946).

18. G. Van Hoven and D. A. Phelps, Physics of Fluids 16, 495 (1973).

19. R.A. Demirkhanov, G. L. Khorasanov, I. K. Sidorova, JEPT 32, 1013 (1971).

20. K. F. Sergeichev and V. E. Trofirnov, JEPT 13, 166 (1971).

21. G.M. Batanov and K.A. Sarksyan, JEPT Letters 13, 384 (1971).

22. T. K. Chu and H.W. Hendel, Physical Review Letters 29, 634 (1972).

23. H. Dreicer, D.B. Hendersen, J.C. Ingraham, Physical Review Letters 26, 1616 (1971).

24. A.W. Trivelpiece and R.W. Gould, Journal of Applied Physics 30, 1784 (1959).

II - THEORY

1 - WAVE PROPAGATION IN A COLD UNBOUNDED PLASMA

The dispersion relation for an electromagnetic wave propagating in a uniformly magnetized plasma is obtained by treating the plasma as a dielectric medium and defining an equivalent dielectric coefficient tensor. The plasma is assumed to be cold i.e., the thermal motion of the particles is neglected; they respond only to the applied electromagnetic fields. The equation of motion for either species (ions or electrons) is given by:[1]

$$m \frac{d\vec{v}}{dt} = e\left(\vec{E} + \vec{v} \times \vec{B}\right) \tag{5}$$

where the appropriate mass and charge is used. For generality, the effects of collisions with other plasma particles or neutrals should be included. These forces can be accounted for phenomenalogically by a collision frequency ν and a force correction $-\nu m\vec{v}$ included on the right hand side of (5). In the experiments reported in this thesis, the collision frequency of electrons with either ions or neutrals is about 10^6 sec^{-1} but since we are interested in frequencies of order 10^{10} sec^{-1}, collisional damping should be negligible. The linear cold theory also allows us to replace $\frac{d}{dt}$ with $\frac{\partial}{\partial t}$ and to neglect the effects of the wave magnetic field. The problem to be concerned with is, therefore, particle motion in a static magnetic field $\vec{B}_o$ when an oscillating electric field is applied.

When the fields are assumed to vary as $\exp i(\vec{k}\cdot\vec{r} - \omega t)$, Maxwell's equations (MKS units) can be written as:[2]

$$\vec{k} \cdot \vec{D} = 0 \tag{6}$$

$$\vec{k} \times \vec{E} = \omega \vec{B} \tag{7}$$

$$\vec{k} \cdot \vec{B} = 0 \tag{8}$$

$$i \vec{k} \times \vec{H} = \vec{J} - i\omega \vec{D} \tag{9}$$

The wave induces a plasma current density of:

$$\vec{J} = \Sigma q n \vec{v} \tag{10}$$

where n is the density and the sum is over each species. With $\vec{v}$ determined from (5), (10) can be written as:

$$\vec{J} = \vec{\vec{\sigma}} \cdot \vec{E} \tag{11}$$

where $\vec{\vec{\sigma}}$ is the conductivity tensor. When this is inserted into equation (9) it yields

$$\vec{k} \times \vec{H} = -\epsilon_0 \omega \vec{\vec{K}} \cdot \vec{E} \tag{12}$$

where the equivalent dielectric tensor $\vec{\vec{K}}$ is defined as [3]

$$\vec{\vec{K}} = \vec{\vec{I}} + \frac{\vec{\vec{\sigma}}}{i\omega\epsilon_0} \tag{13}$$

In Cartesian coordinates $\vec{\vec{K}}$ has the form

$$\vec{\vec{K}} = \begin{pmatrix} K_\perp & -K_x & 0 \\ K_x & K_\perp & 0 \\ 0 & 0 & K_{||} \end{pmatrix} \tag{14}$$

where

$$K_\perp = \frac{K_L + K_R}{2} \tag{15}$$

$$K_x = \frac{i(K_L - K_R)}{2} \tag{16}$$

and

$$K_L = 1 - \frac{\omega_p^2/\omega^2}{\left(1 + \frac{\omega_{ce}}{\omega}\right)\left(1 - \frac{\omega_{ci}}{\omega}\right)} \tag{17}$$

$$K_R = 1 - \frac{\omega_p^2/\omega^2}{\left(1 - \frac{\omega_{ce}}{\omega}\right)\left(1 + \frac{\omega_{ci}}{\omega}\right)} \tag{18}$$

$$K_\parallel = 1 - \omega_p^2/\omega^2 \tag{19}$$

where

$$\omega_p^2 = \omega_{pe}^2 + \omega_{pi}^2 \tag{20}$$

is the plasma frequency, but because of the mass difference between ions and electrons, it is usually written

$$\omega_p^2 = \frac{q^2 n}{m_e \epsilon_0} \tag{21}$$

and the cyclotron frequency ω_c is given by

$$\omega_{ci} = \left|\frac{e}{m_i} B_0\right| \tag{22}$$

$$\omega_{ce} = \left|\frac{e}{m_e} B_0\right| \tag{23}$$

By combining Maxwell's equations (7) and (12), we obtain the wave equation

$$\vec{k} \times (\vec{k} \times \vec{E}) + k_0^2 \overleftrightarrow{K} \cdot \vec{E} = 0 \tag{24}$$

where $k_0 = \omega/c$ is the propagation constant for free space. Equation (24)

represents a set of three linear homogeneous equations for the three components of $\vec{E}$. In order that a non-trivial solution exist, the determinant of the coefficients of $\vec{E}$ must vanish. This gives rise to a dispersion relation. If we let θ be the angle between $\vec{k}$ and $\vec{B}_o$ the dispersion relation can be written as

$$\tan^2\theta = -\frac{K_{\parallel}(n^2-K_R)(n^2-K_L)}{(n^2-K_{\parallel})(K_{\perp}n^2-K_LK_R)} \tag{25}$$

where

$$n = \frac{ck}{\omega} \tag{26}$$

is an index of refraction.

For propagation along the field ($\theta = 0$) there are three modes possible. The first one of these is $K_{\parallel} = 0$ or

$$\omega^2 = \omega_{pe}^2 + \omega_{pi}^2 \tag{27}$$

This describes the longitudinal plasma oscillations which are unaffected by the presence of the static magnetic field $\vec{B}_o$. This mode was first observed by Tonks and Langmuir.[4]

Two other modes exist, $n^2 = K_R$ and $n^2 = K_L$. This dispersion relation for the first of these is

$$\frac{k^2c^2}{\omega^2} = 1 - \frac{\omega_p^2/\omega^2}{\left(1-\frac{\omega_{ce}}{\omega}\right)\left(1+\frac{\omega_{ci}}{\omega}\right)} \tag{28}$$

which is known as the electron cyclotron wave. This mode is right hand circularly polarized ($\vec{E}$ rotates clockwise, i.e., the same sense as electrons, when looking along $\vec{B}_o$) and resonates with the electrons at

the electron cyclotron frequency. In the cold plasma approximation, when $\omega \to \omega_{ce}$, $k_z \to \infty$ and $\lambda \to 0$. This mode can propagate at all frequencies below the electron cyclotron frequency but is cutoff at higher frequencies where k_z becomes negative. It is thus possible for this mode to propagate from a high field to low field region.

The dispersion relation for the other mode is given by

$$\frac{c^2 k_z^2}{\omega^2} = 1 - \frac{\omega_p^2/\omega^2}{\left(1+\frac{\omega_{ce}}{\omega}\right)\left(1-\frac{\omega_{ci}}{\omega}\right)} \qquad (29)$$

and is termed the ion cyclotron wave. This wave is left hand circularly polarized (rotates counter-clockwise with the ions) and resonates at the ion cyclotron frequency.

It is noted that the left wave does not propagate for all frequencies. At frequencies of interest here, i.e. $\omega \simeq \omega_{ce} \gg \omega_{ci}$ and $\omega_p/\omega \gtrsim 1$ we note that the right hand side of (29) is negative. This mode is evanescent, i.e. $\vec{k}_z$ is purely imaginary and the wave is spacially damped as exp $(-|k_z|z)$. This mode is cutoff and the plasma is said to be overdense.

2 - WARM PLASMA EFFECTS

As was seen above, near resonance the dispersion relation for the right hand wave, equation (28), predicts that the wavenumber diverges when $\omega \rightarrow \omega_c$. Thermal motion of the plasma particles can no longer be neglected and the cold plasma theory is no longer valid. In order that the wave magnetic field remain finite for a finite electric field, Maxwell's induction equation (7) requires that $\vec{k}$ become parallel to $\vec{E}$ in the cold theory. Also the wave magnetic field which was neglected in the linearization of the equation of motion (5), must now be included. It is found that thermal effects can considerably alter wave propagation and thus it is necessary to modify the cold theory.

If the plasma particles have components of velocity parallel to the wave propagation, they will now experience an electric field with a Doppler-shifted frequency of $\omega \pm k_z v_z$ where

$$v_z \approx \sqrt{\frac{k T_e}{m_e}} \tag{30}$$

for a Maxwellian distribution. It is now possible for any plasma particle to undergo resonance if it has an appropriate velocity according to the condition

$$\omega_c = \omega \pm k_z v_z \tag{31}$$

The induced plasma currents must now be weighted by an appropriate distribution function such as the Maxwell-Boltzman distribution which then leads to an equivalent dielectric tensor which now includes ther-

mal effects.

When the warm plasma dielectric tensor components are used in the dispersion relation for the left and right hand modes, $n^2 = K_L$ and $n^2 = K_R$, the corresponding warm dispersion relations are obtained:[5]

$$\frac{k_z^2 c^2}{\omega^2} = 1 - \frac{i}{2} \sum_j \frac{\omega_{pj}^2}{k_z \omega} \left(\frac{k T_j}{m_j} \right) \times \left[\langle \textcircled{H} \rangle_1 (1+\epsilon) + \langle \textcircled{H} \rangle_{-1} (1-\epsilon) \right]_j \tag{32}$$

$$\frac{k_z^2 c^2}{\omega^2} = 1 - \frac{i}{2} \sum_j \frac{\omega_{pj}^2}{k_z \omega} \left(\frac{k T_j}{m_j} \right) \times \left[\langle \textcircled{H} \rangle_1 (1-\epsilon) + \langle \textcircled{H} \rangle_{-1} (1+\epsilon) \right]_j \tag{33}$$

where ϵ is the sign of the charge of each of the species j and $\langle \textcircled{H} \rangle_n$ is given by

$$\langle \textcircled{H} \rangle_n = -2 \left(\frac{m}{2kT} \right) F_0(\alpha_n) \tag{34}$$

where $i F_0(\alpha_n)$ is the plasma dispersion function tabulated by Fried and Conte[6] and

$$\alpha_n \equiv \frac{\omega + n\omega_c}{k_z} \left(\frac{m}{2kT} \right)^{1/2}. \tag{35}$$

In the electron cyclotron approximation i.e. $\omega \simeq \omega_{ce} \gg \omega_{ci}$, the dispersion relations (32) and (33) can be written as

$$\frac{k_z^2 c^2}{\omega^2} = 1 + i \frac{\omega_p^2}{k_z \omega} \left(\frac{m_e}{2 k T_e} \right)^{1/2} F_0(\alpha_{\pm 1}^e) \tag{36}$$

where the upper sign is for the left hand mode and the lower sign is for the right hand mode. Far from resonance an approximate form for $F_0(\alpha)$ is used

$$F_0 = \frac{\pi^{1/2} k_z}{|k_z|} e^{-\alpha_n^2} + \frac{i}{\alpha_n}\left(1 + \frac{1}{2\alpha_n^2} + \cdots\right) \qquad (37)$$

When (37)is put into (36) the warm dispersion relations, valid in a region away from resonance are obtained:

$$\frac{k_z^2 c^2}{\omega^2} = 1 - \frac{\omega_p^2}{\omega^2} \frac{\omega}{\omega \pm \omega_c}\left[1 + \left(\frac{k T_e}{m_e}\right) \frac{k_z^2}{(\omega \pm \omega_c)^2}\right] \qquad (38)$$

If the temperature is allowed to approach zero, the cold plasma results (equations 28 and 29) are recovered. It is expected that the dispersion relation for the left hand wave and the dispersion relation for the right hand wave away from the resonance region would not be significantly different from the cold plasma results. This is because, far from resonance, very few elections in a Maxwellian distribution, have velocities high enough to meet the resonant condition (31).

Close to resonance a different condition exists. Now for the right hand mode, electrons need not have very high velocities in order to achieve resonance, thus it is expected that the warm dispersion relation will be quite different from the cold result near the resonant region. Another approximate form for $F_0(\alpha)$which is valid close to resonance is

used:

$$F_o = \frac{\pi^{1/2} k_z}{|k_z|} e^{-\alpha_n^2} + 2i\alpha_n + \cdots \qquad (39)$$

The dispersion relation for the right hand mode becomes

$$\frac{k_z^2 c^2}{\omega^2} \approx 1 - \frac{\omega_p^2}{k_z^2}\left(\frac{m_e}{k T_e}\right)\left(\frac{\omega-\omega_c}{\omega}\right) + i\,\frac{\omega_p^2}{\omega^2}\left(\frac{m_e \pi}{2 k T_e}\right)^{1/2}\frac{\omega}{k_z} \qquad (40)$$

The wavenumber is now complex which allows for non collisional damping (electron cyclotron damping).

The real and imaginary parts of the wavenumber for the right hand wave are plotted in Figure 1 along with a comparison of the cold plasma result. It is seen that except within 5% of resonance, the cold theory adequately predicts the behavior of the right hand wave. At less than 5% the real part of k_z deviates from the cold k_z. Whereas, in the cold plasma case the wavenumber diverges at resonance, the wavelength for the warm plasma case approaches a minimum value. In the same region an imaginary part of k_z appears. This gives rise to cyclotron damping.[7]

The power flow for the right hand wave can be calculated from

$$\frac{P}{P_o} = e^{-2\int \mathrm{Im}\, k_z(z)\, dz} \qquad (41)$$

The results of this calculation are shown in Figure 2. The wave enters the machine at z = +22 cm (see Figure 16 in the apparatus

FIGURE CAPTIONS

Fig. 1. The real and imaginary parts of the wavenumber for the right hand wave at a density of 2×10^{11} cm^{-3}, $T_e = 8eV$ and a frequency of 2.45 GHz are plotted as a function of the ratio of the electron cyclotron frequency ω_c to the wave frequency ω. The cold plasma result is also shown for comparison.

Fig. 2. The percent transmitted right wave power is plotted as a function of axial position. The power damping is calculated from the imaginary part of the wavenumber in Figure 1 and the axial magnetic field profile (Figure 17).

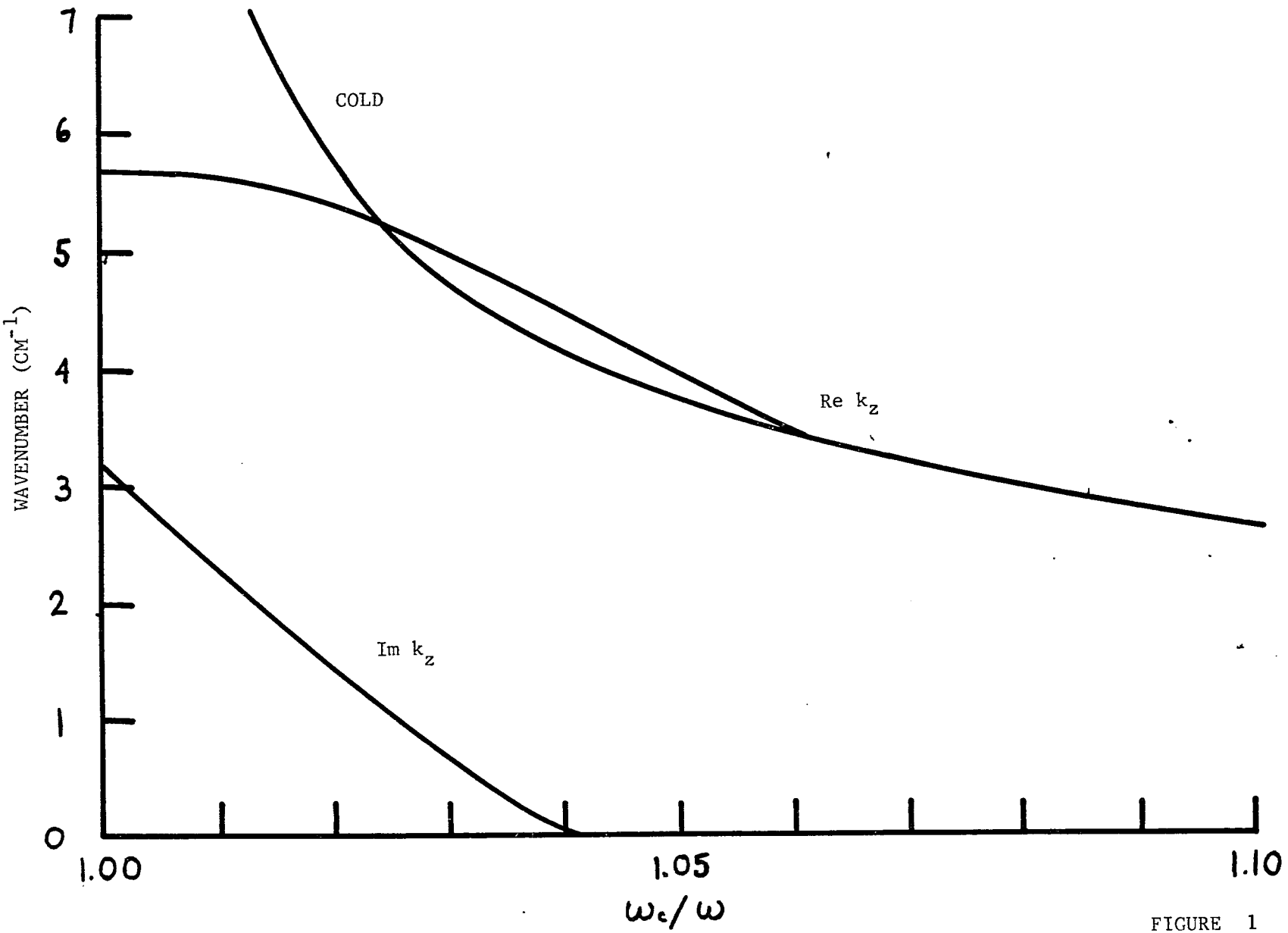
7
6
5
4
3
2
1
0
WAVENUMBER (CM^{-1})
COLD
Re k_z
Im k_z
1.00
1.05
1.10
ω_c/ω

FIGURE 1

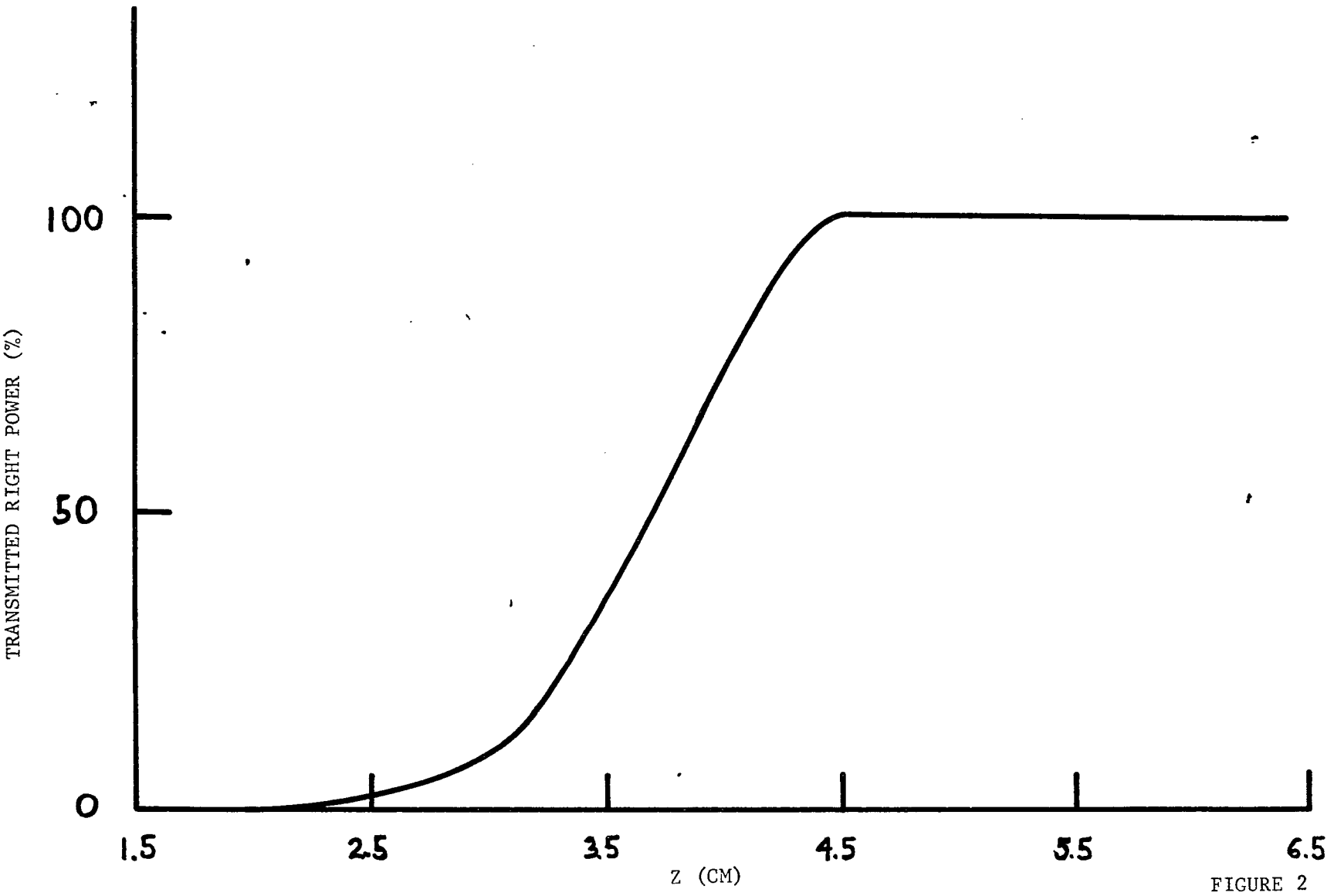

FIGURE 2

section) where $\omega_c/\omega = 1.2$ and propagates along a decreasing magnetic field until it reaches the resonance region located at about $z = 1.5$ cm. This type of arrangement is known as a magnetic beach.[8]

3 - WAVE PROPAGATION IN A COLD BOUNDED PLASMA

In this experiment the plasma is contained in a cylindrical waveguide of radius a = 4.394 cm., (vacuum cutoff frequency = 2.00 GHz). It is therefcre, necessary to calculate the effects that a conducting boundary would have on the cold plasma results. Boundary conditions require that $E_\theta = E_Z = 0$ at r = a.

We will assume the fields have z dependence of the form exp $(ik_z z)$ and, in addition, a radial dependence of exp $(i\vec{p}\cdot\vec{r}_T)$ as well as an azimuthal dependence given by exp $(-im\theta)$. The subscript T stands for transverse. It is convenient to separate the fields and operators into their transverse and z components.[9] Thus

$$\vec{E} = \vec{E}_T + E_z\,\hat{z} \tag{42}$$

$$\vec{H} = \vec{H}_T + H_z\,\hat{z} \tag{43}$$

$$\nabla = \nabla_T + \hat{z}\frac{\partial}{\partial z} = \nabla_T + i k_z \hat{z} \tag{44}$$

$$\vec{K}\cdot\vec{E} = \vec{K}_T\cdot\vec{E}_T + \hat{z}\,K_{11}E_z \tag{45}$$

where

$$\vec{K}_T\cdot\vec{E}_T = K_\perp \vec{E}_T + K_x\,\hat{z}\times\vec{E}_T \tag{46}$$

and $\hat{z}$ is a unit vector in the z direction.

When (42) - (46) are put into the wave equation

$$\nabla^2\vec{E} + k_o^2\vec{K}\cdot\vec{E} - \nabla(\nabla\cdot\vec{E}) = 0 \tag{47}$$

coupled wave equations of the form

$$\nabla_T^2 E_z + a\,E_z = b\,H_z \tag{48}$$

$$\nabla_T^2 H_z + c\,H_z = d\,E_z \tag{49}$$

are obtained.

These can be transformed to an uncoupled set of forth order equations:

$$\left[\nabla_T^4 + (a+c)\nabla_T^2 + (ac-bd)\right] E_z = 0 \tag{50}$$

$$\left[\nabla_T^4 + (a+c)\nabla_T^2 + (ac-bd)\right] H_z = 0 \tag{51}$$

The radial dependence $\exp(i\vec{p}\cdot\vec{r}_T)$ where p is the perpendicular wave number is inserted to obtain

$$p^4 - (a+c)p^2 + (ac-bd) = 0 \tag{52}$$

This is the dispersion relation. Explicitly

$$p^4 - \left[-k_z^2\left(\frac{K_{11}}{K_\perp}+1\right) + k_0^2\left(K_{11} + \frac{K_R K_L}{K_\perp}\right)\right] p^2 + \frac{K_{11}}{K_\perp}\left(-k_z^2 + k_0^2 K_R\right)\left(-k_z^2 + k_0^2 K_L\right) = 0 \tag{53}$$

where the form of the solution for E_z is given by

$$(\nabla_T^2 + p_i^2)\, E_{zi} = 0 \tag{54}$$

for each value of p^2.

For a longitudinally magnetized, cylindrical waveguide the general solutions to (54) are

$$E_{z1} = A\, J_m(p_1 r)\, e^{im\theta} \tag{55}$$

$$E_{z2} = B\, J_m(p_2 r)\, e^{im\theta} \tag{56}$$

where J_m is the ordinary Bessel function and A and B are arbitrary constants. Applying the boundary conditions $E_z = E_\theta = 0$ at r = a determines

the relative values of A and B

$$\frac{B}{A} = -\frac{J_m(p_1 a)}{J_m(p_2 a)} \tag{57}$$

and yields the determinantal equation

$$g_2 p_1 J_m'(p_1 a)\, J_m(p_2 a) - g_1 p_2 J_m'(p_2 a)\, J_m(p_1 a) = m i k_0^2 K_x \frac{p_2^2 - p_1^2}{a} J_m(p_1 a)\, J_m(p_2 a) \tag{58}$$

where

$$g_{1,2} = \left(k_0^2 K_\perp - k_z^2\right)^2 + \left(k_0^2 K_x\right)^2 - \left(k_0^2 K_\perp - k_z^2\right) p_{1,2} \tag{59}$$

and the prime denotes the derivative with respect to the argument. The simultaneous solution of the dispersion relation and the determinantal equation yield values of k_z and p for any given plasma parameters and frequencies.

At cutoff, the propagation constant vanishes, i.e. $k_z = 0$ and the right hand sides of equations (48) and (49) also vanish, thus yielding two uncoupled wave equations for E_z and H_z. It is therefore possible to have separate E and H waves. For H waves, the cutoff condition is given by

$$(p_h a)\, \frac{J_m'(p_h a)}{J_m(p_h a)} = -i m \frac{K_x}{K_\perp} \tag{60}$$

where

$$p_h^2 = k_0^2 \frac{K_R K_L}{K_\perp} \tag{61}$$

For E waves, the cutoff frequency is

$$\omega_{co}^2 = \omega_p^2 + (p_e c)^2 \tag{62}$$

where

$$p_e a = \epsilon_{mn} \tag{63}$$

where ϵ_{mn} is the n^{th} zero of the m^{th} - order Bessel function.

The results of the calculations of the dispersion relation for the m = +1 mode are shown in Figures 3,4,5,and 6. Figure 3 gives a schematic representation of the dispersion characteristics. It is seen that the dispersion relation divides into two main branches. The lower branch propagates at all frequencies below the cyclotron frequency and has a resonance at $\omega = \omega_c$. The right hand wave propagating in this mode along a magnetic beach is the mechanism of generating plasma in this experiment. The upper branch allows propagation for frequencies $\omega_p < \omega < \omega_{UH}$ where

$$\omega_{UH}^2 = \omega_{pe}^2 + \omega_{ce}^2 \tag{64}$$

is the upper hybrid frequency. Also note that in this branch, the phase velocity ω/k is positive while the group velocity $d\omega/dk$ is negative. A wave having this property of oppositely directed phase and group velocities is known as a backward wave.

Figure 4 shows the results of the exact cold plasma calculation. Note that there are many roots of the dispersion relation as well as the lowest root shown in Figure 3 . A difficulty arises in the calculation of these roots, in that it is possible for a root which is near another root for which one of the p^2 goes through zero, to pass through this region. When one of the values of p^2 is zero the solution is trivial, i.e. all field components vanish. It is also noted that when a value of p is imaginary, the ordinary J_m Bessel functions must be replaced with the modified Bessel functions I_m.

The low branch clearly shows $k_z \longrightarrow \infty$ as $\omega \rightarrow \omega_c$ in agreement

with Figure 3 , the upper branch however is more complicated. Now there are many roots appearing, approaching ω_p for large k_z and ω_{UH} at cutoff. The cutoff frequencies of these roots for $\omega \lesssim \omega_{UH}$ have been identified as the cutoff frequencies of H waves from the solution of equation (60) .

Figures 5 and 6 show these same dispersion characteristics for typical frequencies, one in the low branch (1780 MHz) and one in the high branch (3980 MHz) but now the propagation constant is plotted as a function of density. It should also be noted that when the above calculations are performed for the m = 0 mode, similar results are obtained.

It is noted that the fields have the form $\exp(ik_z z - i\omega t - im\theta)$ where m is an integer. For a point of constant phase at a fixed z it is seen that

$$\frac{d\theta}{dt} = -\frac{\omega}{m} \tag{65}$$

therefore waves with m = +1 will rotate oppositely from those with m = -1. In this notation modes with $m < 0$ rotate clockwise (when viewed along $\vec{B}_o$) and correspond to the right hand wave while modes with $m > 0$ rotate counter-clockwise and correspond to the left hand mode in the unbounded case.

In Figure 7 there is a comparison of the bounded and unbounded theories for the right hand wave. As would be expected the boundaries have little effect on k_z, because at resonance λ goes to a minimum

FIGURE CAPTIONS

Fig. 3. A schematic diagram of the dispersion relation of a longitudinally magnetized cold plasma in a cylindrical waveguide for the $m = +1$ mode.

Fig. 4. The dispersion characteristics, the simultaneous solution of equations (53) and (58), are plotted for the $m = +1$ mode. Waveguide radius $a = 4.39$ cm, $n = 2 \times 10^{11}$ cm^{-3} and $f_c = \omega_c/2\pi = 2.7$ GHz ($\omega_c/\omega = 1.1$).

Fig. 5. The wavenumber is plotted as a function of the density for a frequency of 1780 MHz. $a = 4.39$ cm, $f_c = 2.7$ GHz.

Fig. 6. The wavenumber is plotted as a function of the density for a frequency of 3980 MHz. $a = 4.39$ cm, $f_c = 2.7$ GHz.

Fig. 7. The wavenumber for both the bounded and unbounded cold right wave are plotted as a function of ω_c/ω for typical parameters in this experiment. The perpendicular wavenumbers p_1 and p_2 are also shown.

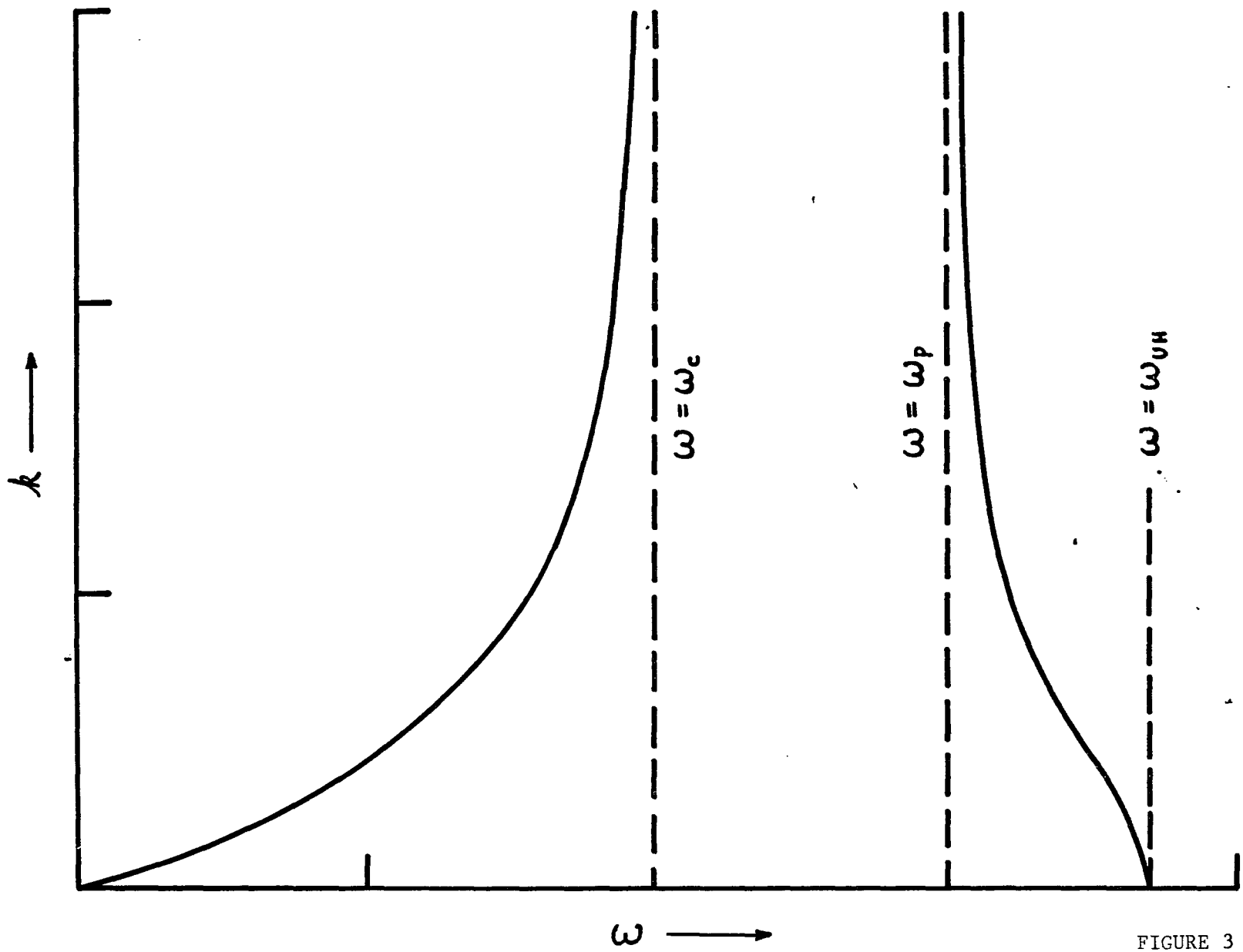

FIGURE 3

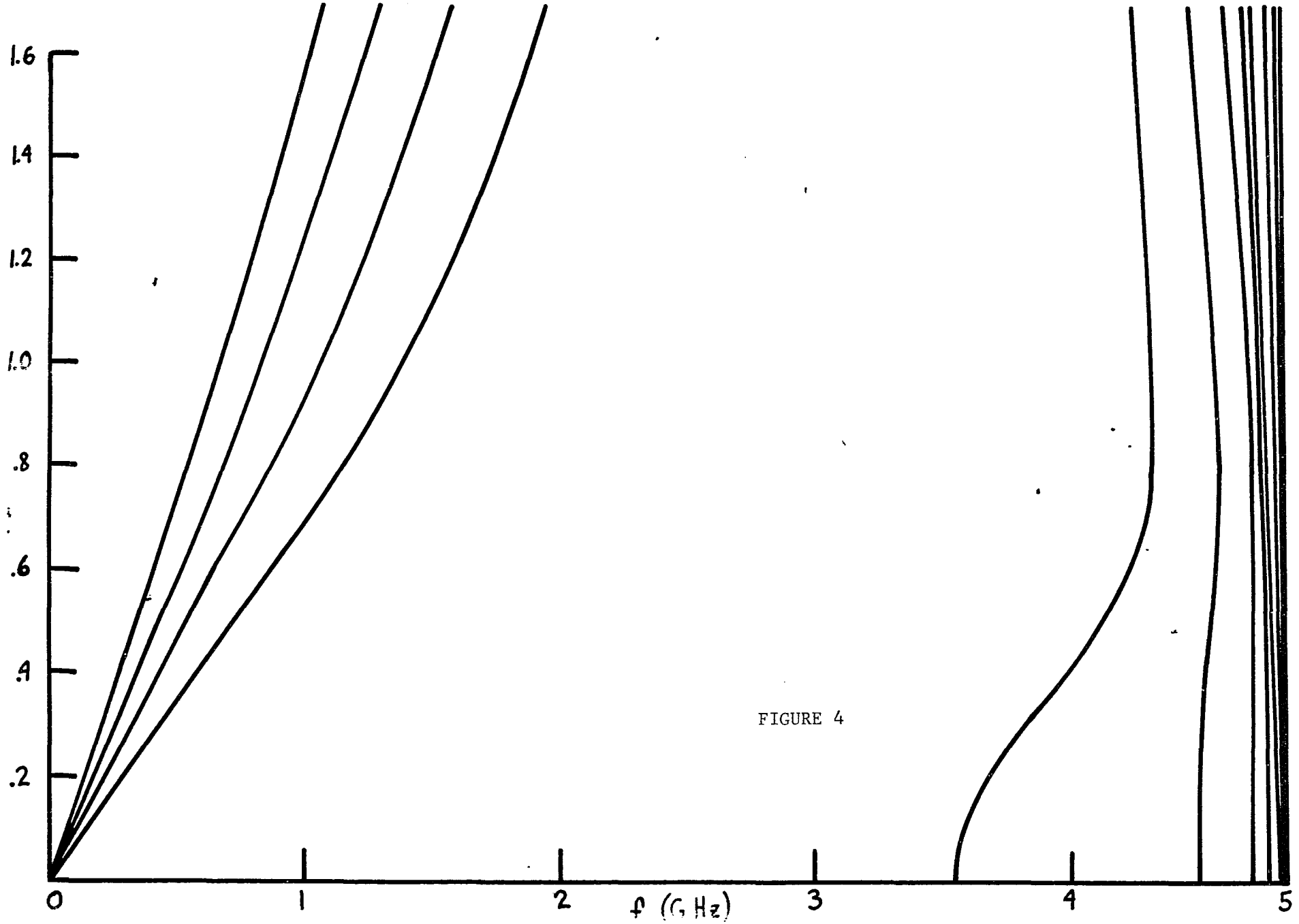

FIGURE 4

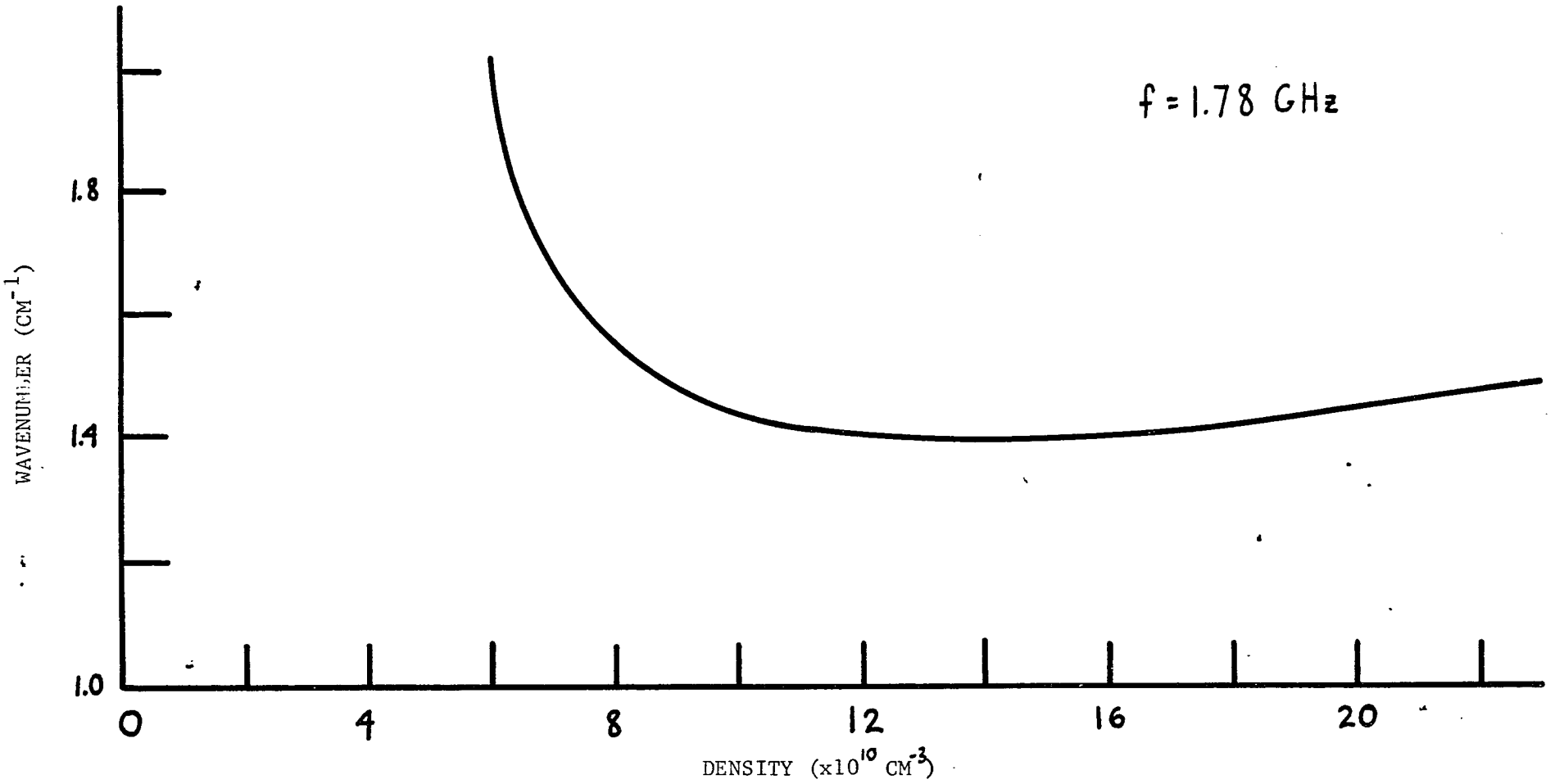
f = 1.78 GHz
1.8
1.4
1.0
WAVENUMBER (CM^{-1})
0
4
8
12
16
20
DENSITY (x10^{10} CM^{-3})

FIGURE 5

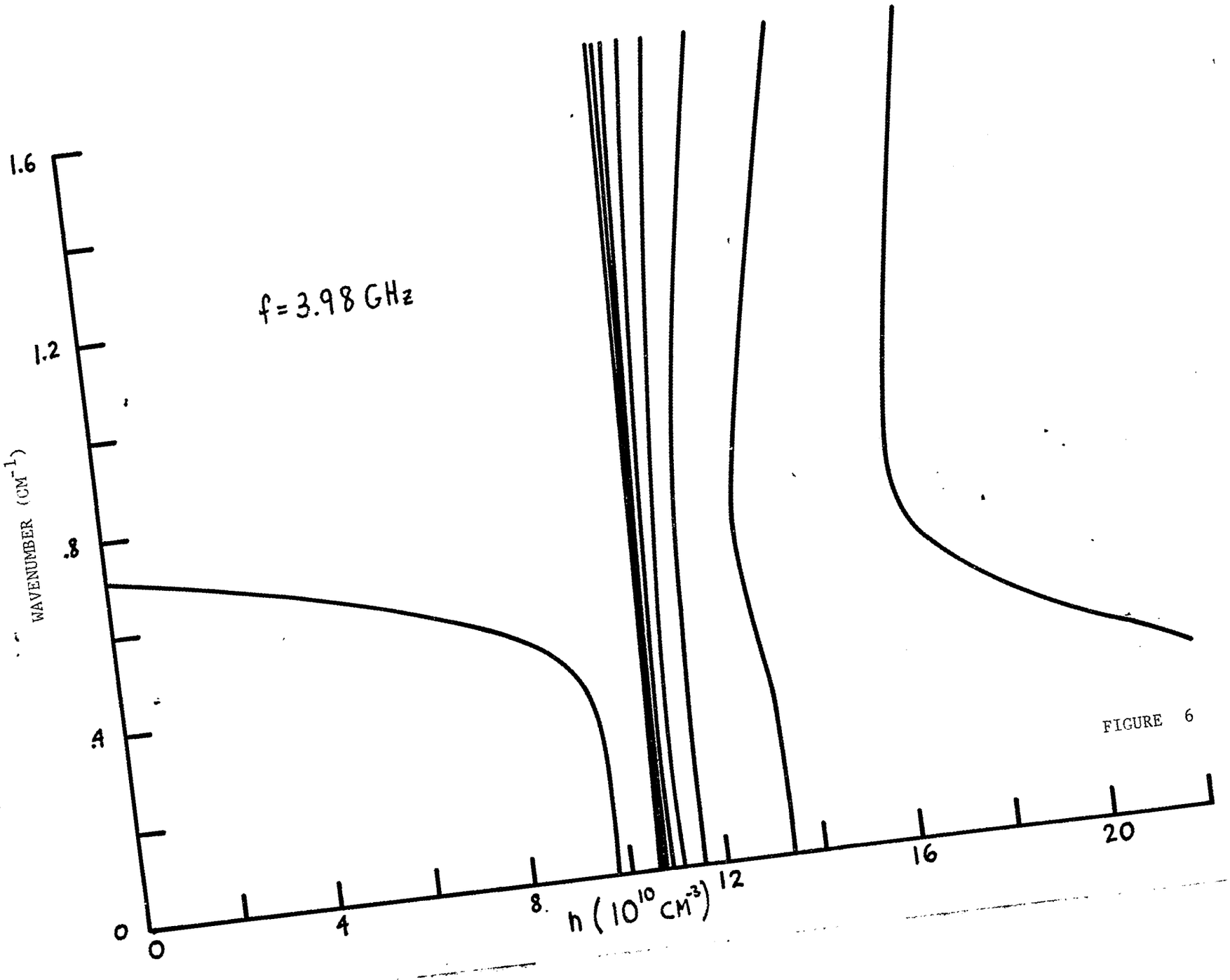

FIGURE 6

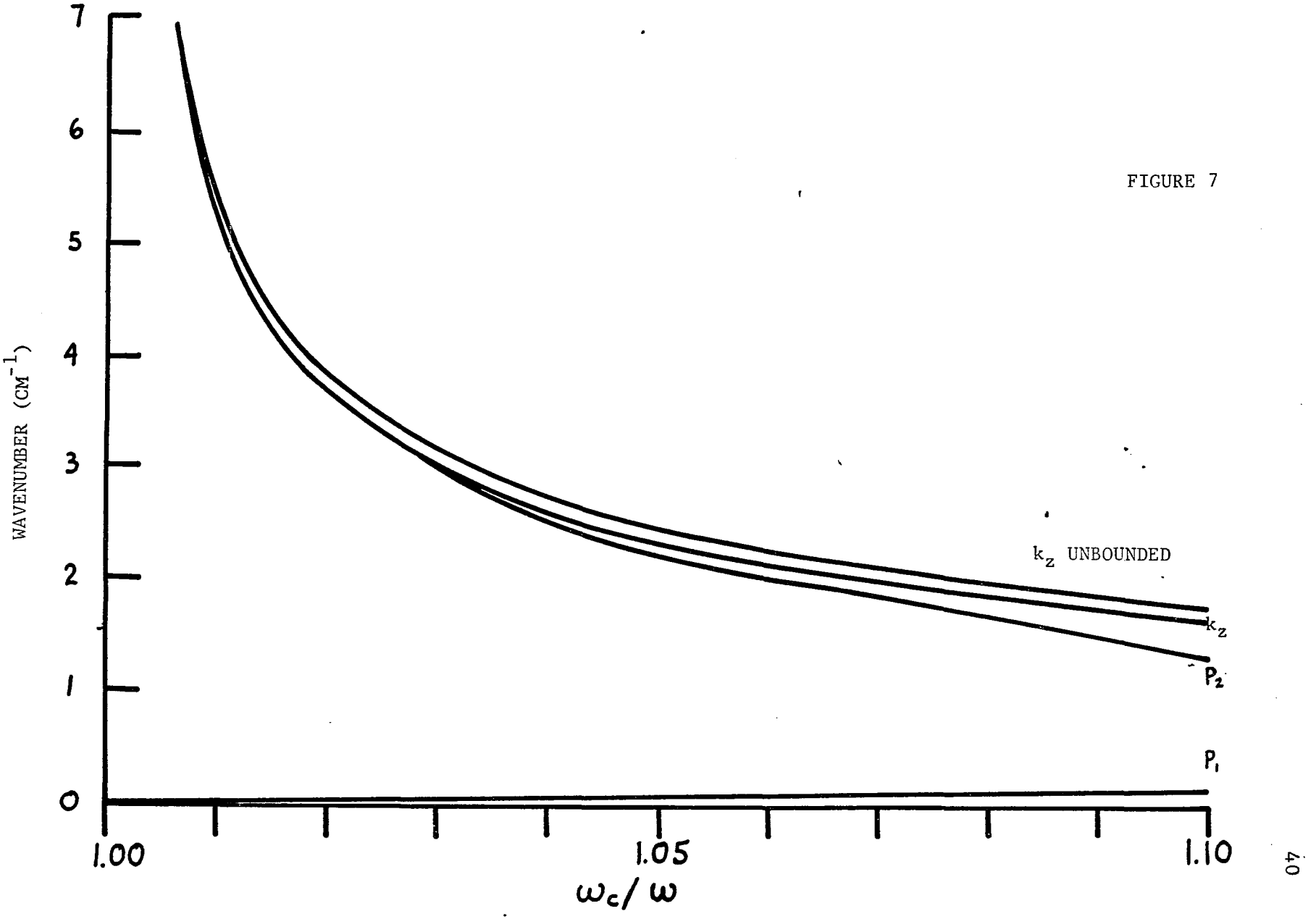
7
6
5
4
3
2
1
0
WAVENUMBER (CM^{-1})
k_z UNBOUNDED
k_z
P_2
P_1
1.00
1.05
1.10
ω_c/ω

FIGURE 7

and thus becomes small compared to the guide radius.

A comparison of the bounded and unbounded theories for the left wave is made in Figure 8 , but now the cutoff frequency is plotted against density rather than k_z versus ω_c/ω. It is seen that introducing a magnetized plasma into the waveguide has the effect of raising the cutoff frequency while surrounding the plasma with a conductor has the effect of lowering the cutoff density.

The complete field solutions can now be obtained by inserting equations (42) - (46)into Maxwell's equations. The results are:

$$E_z = \left[A J_m(p_1 r) + B J_m(p_2 r) \right] e^{im\theta} \tag{66}$$

$$E_r = A \left[l_2 p_1 J_m'(p_1 r) - \frac{im}{r} L_2 J_m(p_1 r) \right] e^{im\theta} + B \left[l_1 p_2 J_m'(p_2 r) - \frac{im}{r} L_1 J_m(p_2 r) \right] e^{im\theta} \tag{67}$$

$$E_\theta = A \left[\frac{im}{r} l_2 J_m(p_1 r) + L_2 p_1 J_m'(p_1 r) \right] e^{im\theta} + B \left[\frac{im}{r} l_1 J_m(p_2 r) + L_1 p_2 J_m'(p_2 r) \right] e^{im\theta} \tag{68}$$

$$H_z = \left[A h_1 J_m(p_1 r) + B h_2 J_m(p_2 r) \right] e^{im\theta} \tag{69}$$

$$H_r = A\left[y_2\, p_1\, J_m'(p_1 r) - \frac{im}{r}\, Y_2\, J_m(p_1 r)\right] e^{im\theta}$$
$$+ B\left[y_1\, p_2\, J_m'(p_2 r) - \frac{im}{r}\, Y_1\, J_m(p_2 r)\right] e^{im\theta} \qquad (70)$$

$$H_\theta = A\left[\frac{im}{r}\, y_2 J_m(p_1 r) + Y_2\, p_1\, J_m'(p_1 r)\right] e^{im\theta}$$
$$+ B\left[\frac{im}{r}\, y_1 J_m(p_2 r) + Y_1\, p_2\, J_m'(p_2 r)\right] e^{im\theta} \qquad (71)$$

where

$$l_{1,2} = \frac{i}{k_z}\left[1 - \frac{k_0^2 K_\perp p_{1,2}^2}{(k_0^2 K_\perp - k_z^2)^2 + (k_0^2 K_x)^2}\right] \qquad (72)$$

$$L_{1,2} = \frac{i}{k_z}\frac{K_\perp}{K_x}\left[1 - \frac{p_{1,2}^2 (k_0^2 K_\perp - k_z^2)}{(k_0^2 K_\perp - k_z^2)^2 + (k_0^2 K_x)^2}\right] \qquad (73)$$

$$h_{1,2} = \frac{K_\perp p_{1,2}^2 - K_{||}(k_0^2 K_\perp - k_z^2)}{\omega \mu_0 k_z K_x} \qquad (74)$$

$$y_{1,2} = \frac{K_\perp}{i\omega\mu_0 K_x}\left[\frac{p_{1,2}^2 (k_0^2 K_\perp - k_z^2) + (k_0^2 K_\perp - k_z^2)^2 + (k_0^2 K_x)^2}{(k_0^2 K_\perp - k_z^2)^2 + (k_0^2 K_x)^2}\right] \qquad (75)$$

$$Y_{1,2} = \frac{k_0^2 K_\perp p_{1,2}^2}{i\omega\mu_0\left[\left(k_0^2 K_\perp - k_z^2\right) + \left(k_0^2 K_x\right)^2\right]} \tag{76}$$

For the parameters in this experiment, $n = 2\times10^{11}$ cm^{-3} and $f = 2.45$ GHz, the right mode propagates but the left mode is cutoff. The cutoff density for the left wave is shown in Figure 9 while Figure 10 shows the evanescent electric field profile for this mode.

FIGURE CAPTIONS

Fig. 8. The cutoff frequency of the left wave is plotted against density for both the bounded and unbounded cases. a = 4.39 cm for the bounded calculation and f_c = 2.7 GHz.

Fig. 9. The wavenumber squared for the bounded left wave is plotted against density for f_c = 2.7 GHz. The wavenumber passes through zero at a density of 6.6×10^{10} cm^{-3}.

Fig. 10. The calculated electric field profiles in arbitrary units are plotted as a function of the normalized radial position for the m = +1 left wave at conditions typical of this experiment.

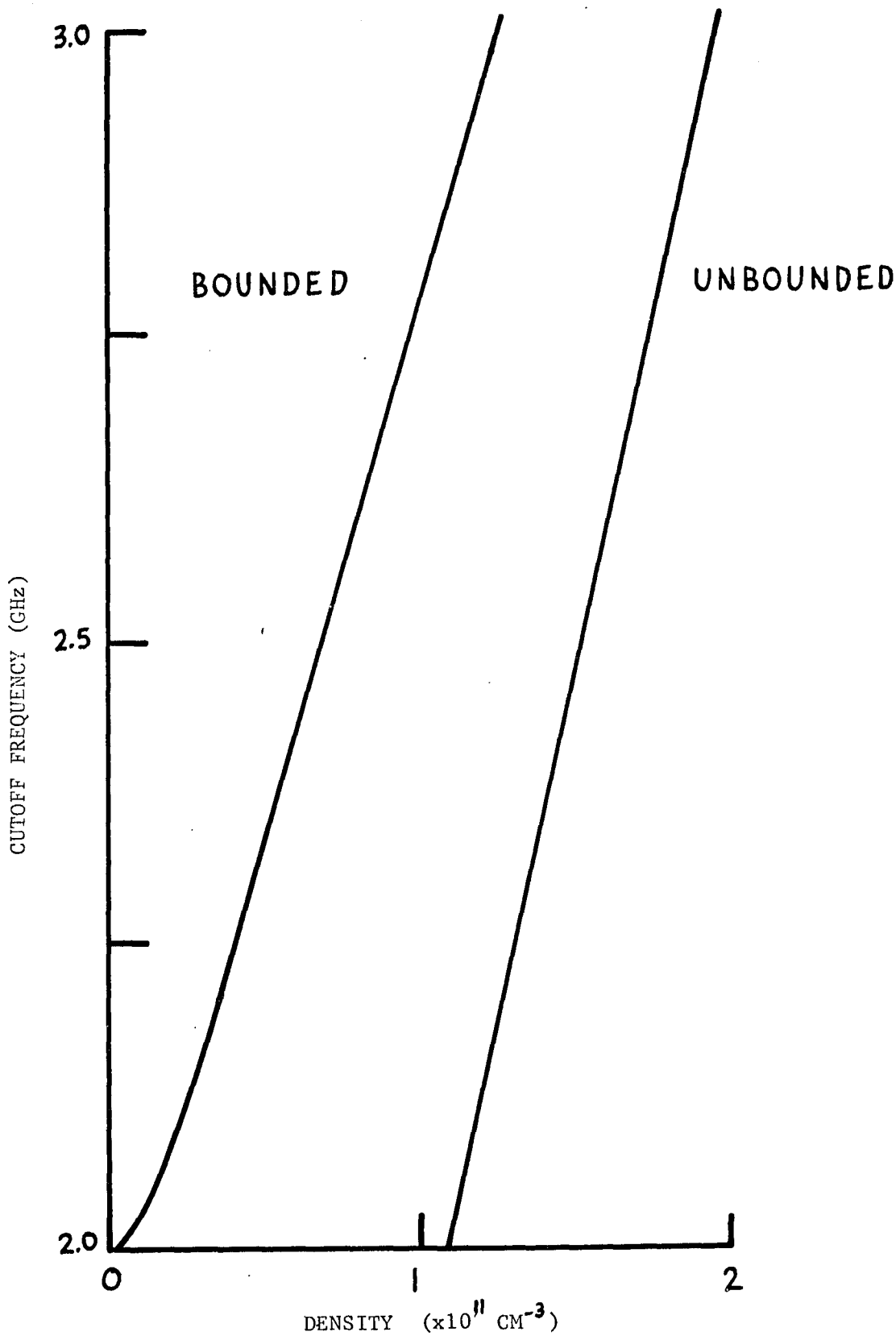
3.0
2.5
2.0
BOUNDED
UNBOUNDED
CUTOFF FREQUENCY (GHz)
0
1
2
DENSITY (x10^11 CM^-3)

FIGURE 8

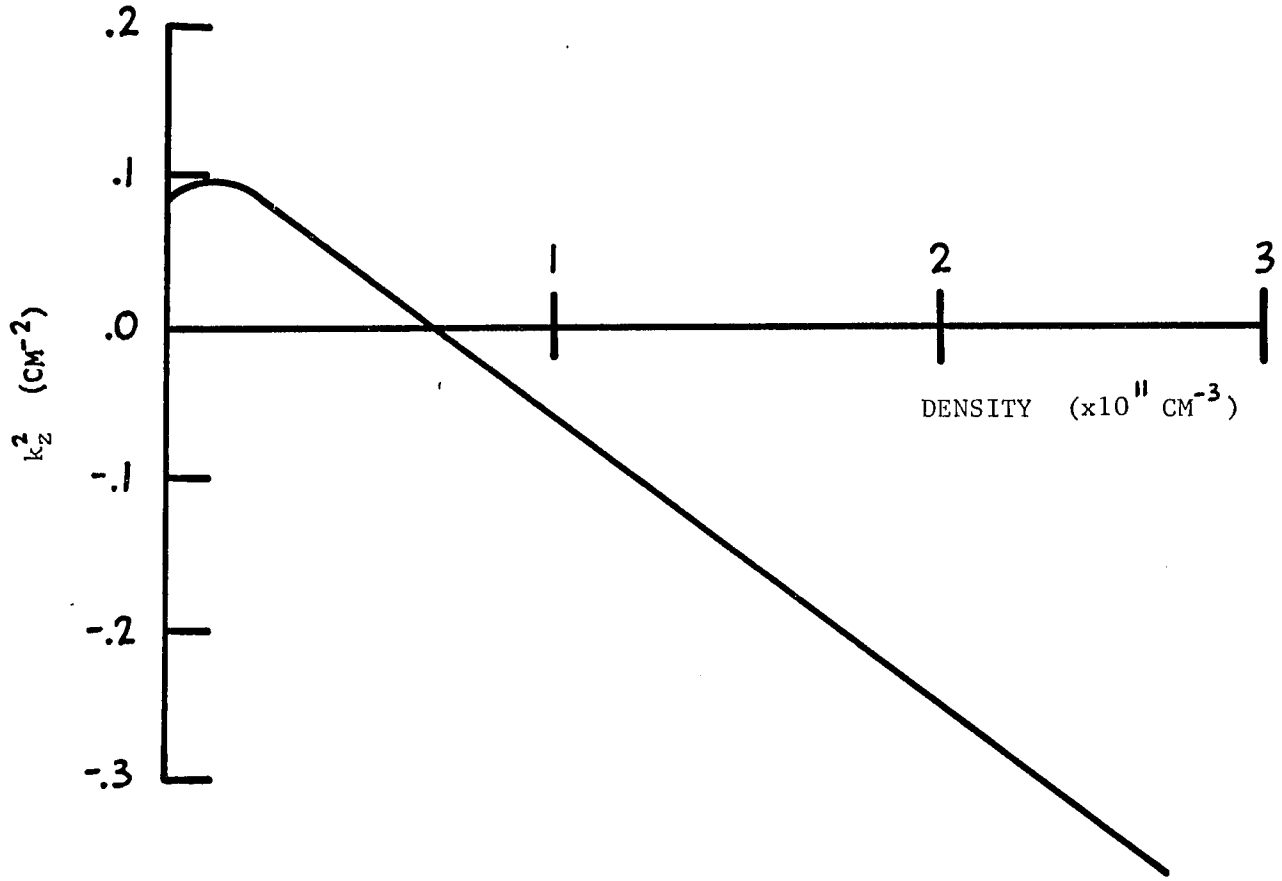

FIGURE 9

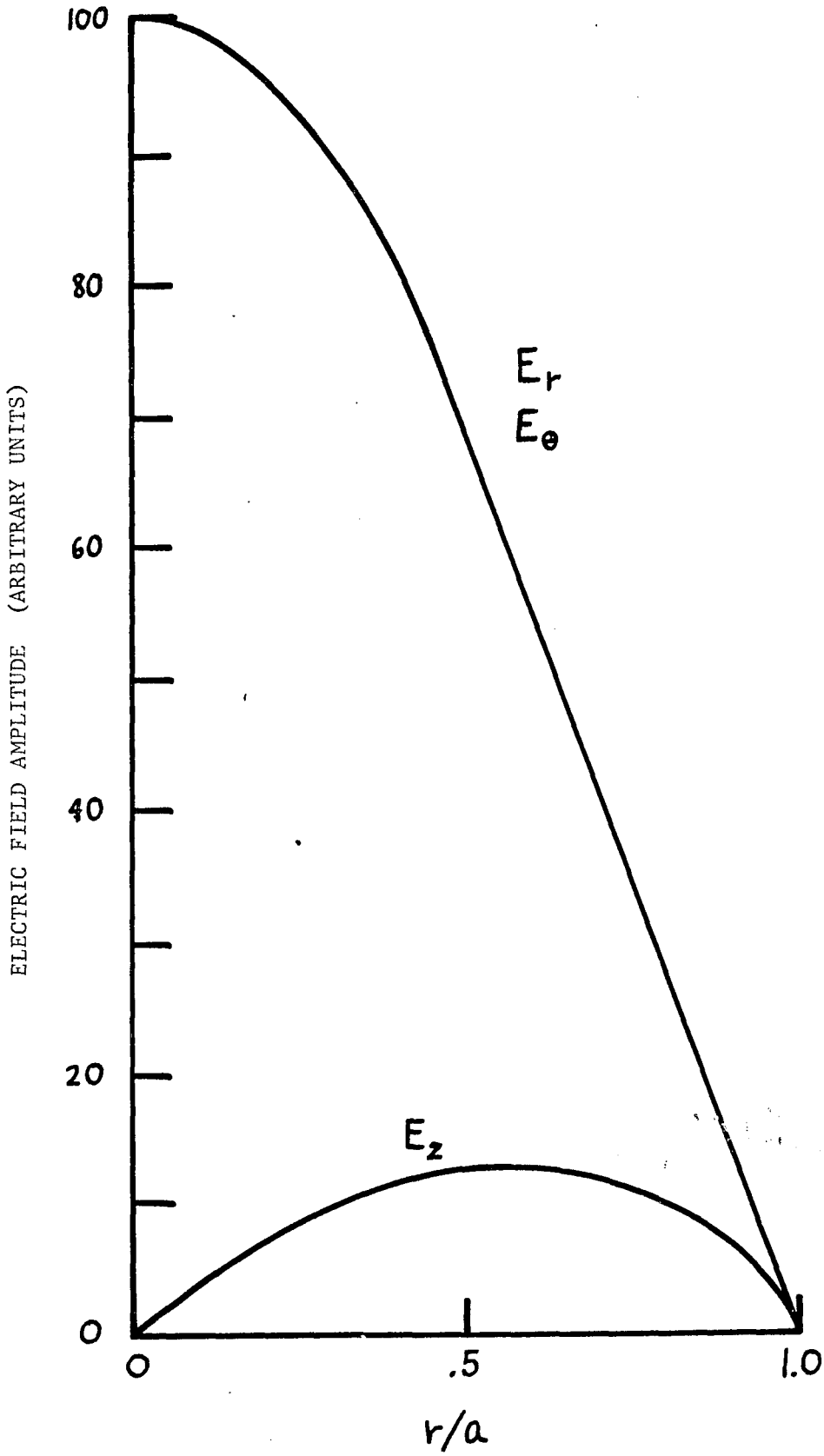
100
80
60
40
20
0
ELECTRIC FIELD AMPLITUDE (ARBITRARY UNITS)
E_r
E_θ
E_z
0
.5
1.0
r/a

FIGURE 10

4 - COMPARISON OF VARIOUS THEORIES

For electromagnetic waves propagating along a static magnetic field there are two possible modes i.e., both the left and right hand circularly polarized waves. As was seen in Figure 1 , more than 5% from resonance the cold unbounded theory suffices for the right hand $m = -1$ mode, however when less than 5% from resonance the cold theory fails, predicting that the wavenumber diverges as ω approaches ω_{ce} . In this region it is necessary to include thermal effects. The warm theory now predicts that the wavelength approached a minimum value at resonance and the wave can undergo cyclotron damping. The receipe then for the right hand wave would be to use the cold bounded theory when greater than 5% from the resonance region and the unbounded warm theory when less than 5% from resonance. It should be noted that the bounded warm theory was not applied because this problem cannot be solved in closed form. Swanson[10] found that when boundary conditions are applied to the warm theory, a set of infinite order differential equations are obtained (since they contain an infinite series of Bessel functions). If n^{th} order terms are included, then $2(n+1)$ boundary conditions are required to determine the solution.

For the left wave a different situation exists. Here the cold and warm theories give almost identical results which one would expect since we are several orders of magnitude away from the resonant frequency of this mode. An ion cyclotron wave behaves linearly near electron cyclotron resonance. However, the boundaries become all important

when considering this case. This is because the m = +1 mode is near cutoff in the vicinity of $\omega \approx \omega_{ce}$. At cutoff, λ approaches infinity and thus it is comparable to the waveguide dimensions. Cold bounded theory predicts that if the density is below the cutoff density, the wave will propagate unattenuated, however if the plasma density is above the cutoff density (overdense) the wave will be completely reflected at the cutoff point.

5 - ELECTROSTATIC APPROXIMATION

One of the properties of plasma waveguides is that they can propagate slow waves having phase velocities smaller than c. An approximate field solution for these waves can be obtained by regarding the velocity of light to be infinite and thus the fields essentially static. This analysis of wave propagation in a magnetized plasma waveguide was first done by Trivelpiece and Gould.[11]

If we assume that the first order magnetic field is negligible we can write

$$\nabla \times \vec{E} = 0 \tag{77}$$

and

$$\nabla \cdot (\epsilon_0 \overleftrightarrow{K} \cdot \vec{E}) = 0 \tag{78}$$

It is then possible to derive the electric field from a scalar potential ϕ. Thus

$$\vec{E} = -\nabla \phi \tag{79}$$

Putting (79) into (78) we get

$$\nabla \cdot (\overleftrightarrow{K} \cdot \nabla \phi) = 0 \tag{80}$$

which leads to the wave equation

$$K_\perp \nabla_T^2 \phi + K_{11} \frac{\partial^2 \phi}{\partial z^2} = 0 \tag{81}$$

Assume that $\phi \sim e^{-ikz}$. Then

$$\nabla_T^2 \phi - k^2 \frac{K_{\parallel}}{K_{\perp}} \phi = 0 \tag{82}$$

In cylindrical coordinates, the solution to (82) is

$$\phi = A J_m(pr)\, e^{ikz}\, e^{im\theta} \tag{83}$$

where

$$p^2 = -k^2 \frac{K_{\parallel}}{K_{\perp}} \tag{84}$$

or

$$k = \pm p \left[\frac{-\omega^2(\omega^2 - \omega_p^2 - \omega_c^2)}{(\omega^2 - \omega_p^2)(\omega^2 - \omega_c^2)} \right]^{1/2} \tag{85}$$

where $K_{\parallel}$ and $K_{\perp}$ have been evaluated in the electron cyclotron limit i.e. $\omega \approx \omega_{ce} = \omega_c$ and $\omega \gg \omega_{ci}$. Applying the boundary condition namely $E_z = 0$ at $r = a$ requires that

$$p = \frac{\chi_{mn}}{a} \tag{86}$$

where χ_{mn} is the n^{th} root of $J_m(pr) = 0$. The dispersion relation then reads

$$ka = \pm \chi_{mn} \left[\frac{-\omega(\omega^2 - \omega_p^2 - \omega_c^2)}{(\omega^2 - \omega_p^2)(\omega^2 - \omega_c^2)} \right]^{1/2} \tag{87}$$

and is plotted in Figure 11 for typical parameters. It is noted that two branches appear. A low frequency branch approaching ω_c and a high frequency branch approaching ω_p for $\omega_c < \omega_p$. When $\omega_c > \omega_p$ these two branches reverse. Figure 12 shows these modes plotted

FIGURE CAPTIONS

Fig. 11. The dispersion relation for the Gould-Trivelpiece modes is plotted for two different densities, $n_1 = 0.5 \times 10^{11}$ cm^{-3} and $n_2 = 2.0 \times 10^{11}$ cm^{-3}. Note that for n_1, the low frequency branch approaches the plasma frequency for that density and the high frequency branch approaches the cyclotron frequency; however for n_2 the low branch approaches the cyclotron frequency and the high branch approaches the plasma frequency for that density.

Fig. 12. The wavenumber versus density is plotted for two typical frequencies, one in the low branch and one in the high branch. $m = 0$, $f_c = 2.45$ GHz and $a = 4.39$ cm.

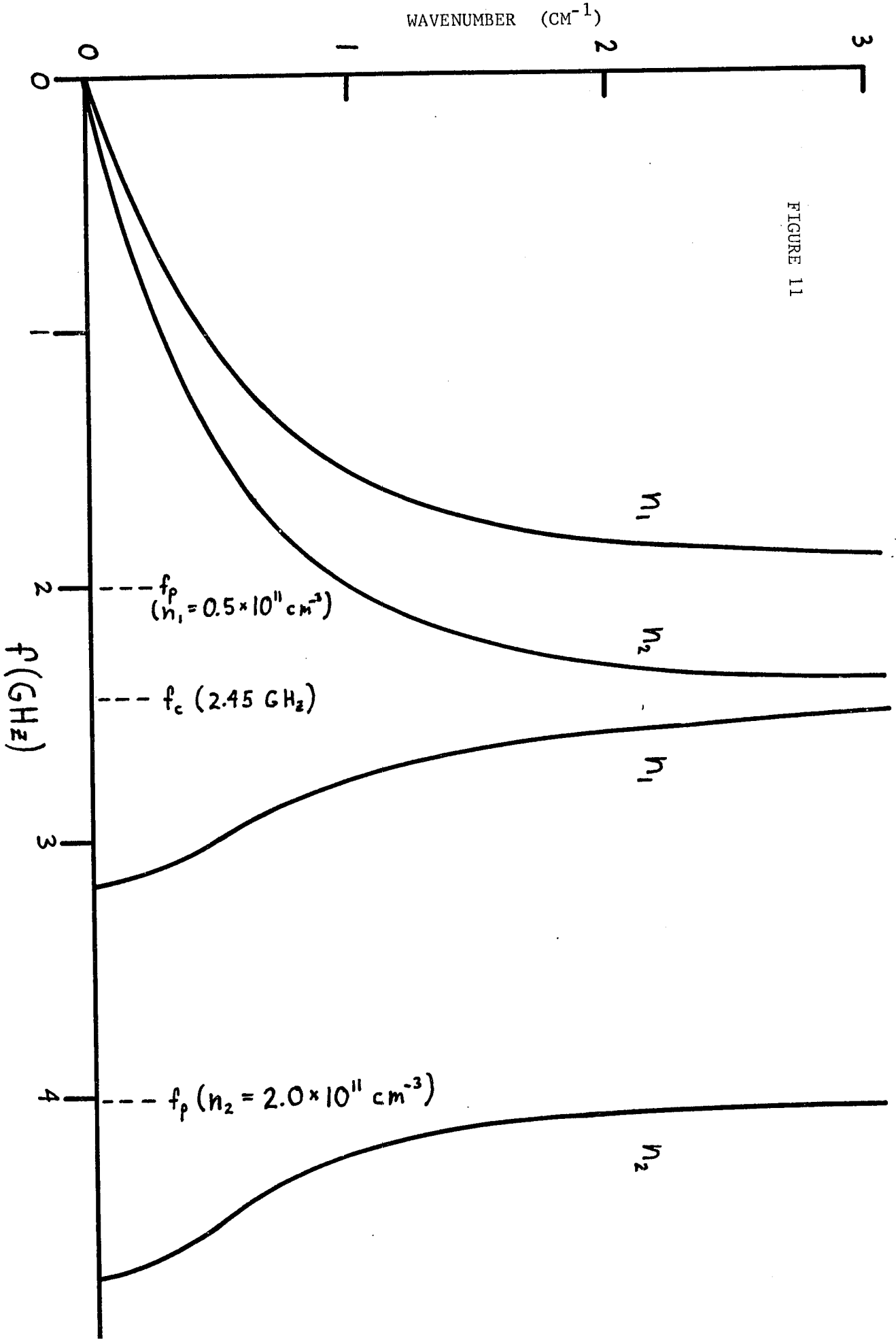
WAVENUMBER (CM^{-1})
0
1
2
3
f (GHz)
0
1
2
3
4
f_p ($n_1 = 0.5 \times 10^{11}$ cm^{-3})
f_c (2.45 GHz)
f_p ($n_2 = 2.0 \times 10^{11}$ cm^{-3})
n_1
n_2
n_1
n_2

FIGURE 11

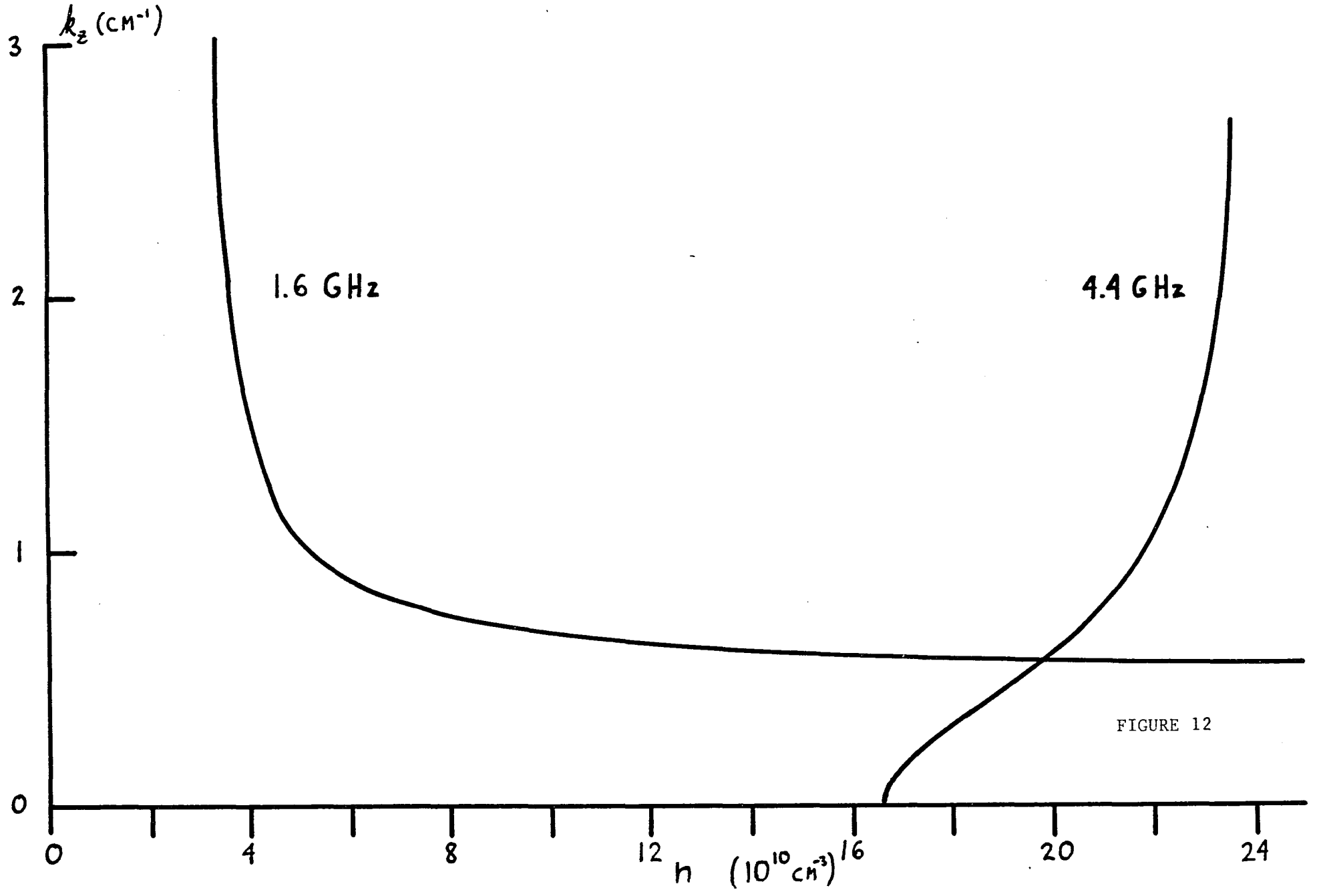

FIGURE 12

against density. Figure 13 shows the magnetic field profiles for the low frequency branch while Figure 14 is for the high frequency branch. The magnetic fields are computed from[12]

$$\nabla \times \vec{H} = i\omega \epsilon_o \overleftrightarrow{K} \cdot \vec{E} \tag{88}$$

The complete field solutions are given as:

$$E_r = -A p J_m'(pr) e^{im\theta} \tag{89}$$

$$E_\theta = \frac{-iAm}{r} J_m(pr) e^{im\theta} \tag{90}$$

$$E_z = iA k J_m(pr) e^{im\theta} \tag{91}$$

$$H_r = AY_1\left[pJ_m'(pr) - \frac{m}{r}\frac{\omega_c}{\omega} J_m(pr)\right]e^{im\theta} - iBkJ_m'(ikr)e^{im\theta} \tag{92}$$

$$H_\theta = iAY_1\left[\frac{m}{r}J_m(pr) - p\frac{\omega_c}{\omega}J_m'(pr)\right]e^{im\theta} - \frac{iBm}{r}J_m(ikr)e^{im\theta} \tag{93}$$

$$H_z = AY_3 ikJ_m(pr)e^{im\theta} + BikJ_m(ikr)e^{im\theta} \tag{94}$$

where

$$B = \frac{pJ_m'(pa)}{ikJ_m'(ika)} AY_1 \tag{95}$$

and

$$Y_1 = \frac{\epsilon_0 \omega^2 (\omega^2 - \omega_p^2 - \omega_c^2)}{i k \omega_c (\omega^2 - \omega_c^2)} \tag{96}$$

$$Y_3 = - \frac{\epsilon_0 (\omega^2 - \omega_p^2)}{i k \omega_c} \tag{97}$$

and the boundary condition $H_r = 0$ at $r = a$ requires that

$$p = \frac{\chi_{mn}}{a} \tag{98}$$

where χ_{mn} is the n^{th} root of J_m.

In the electrostatic approximation, damping can be easily included in the calculations. The $-m_e \nu \vec{V}$ collisional term which was previously omitted can now be included into (87) by replacing m_e with the quantity $m_e (\omega - i\nu)/\omega$.[13] Thus

$$\omega_p^2 \longrightarrow \frac{\omega_p^2}{1 - i\frac{\nu}{\omega}} \tag{99}$$

and

$$\omega_c \longrightarrow \frac{\omega_c}{1 - i\frac{\nu}{\omega}} \tag{100}$$

The results of this calculation for the low frequency branch is shown in Figure 15. It is seen that the inclusion of a collision frequency has the effect of increasing the wavelength.

FIGURE CAPTIONS

Fig. 13. The radial magnetic field profiles for f = 1780 MHz, a typical frequency in the lower branch. The relative field amplitude is plotted against the normalized radial position. $n = 2.0 \times 10^{11}$ cm^{-3}, $f_c = 2.45$GHz and a = 4.39 cm.

Fig. 14. The radial magnetic field profiles for f = 4070 MHz, a typical frequency in the high branch. The relative field amplitude is plotted against the normalized radial position. $n = 2.0 \times 10^{11}$ cm^{-3}, $f_c = 2.45$GHz and a = 4.39 cm.

Fig. 15. The real and imaginary parts of the wavenumber are plotted against density for various values of collision frequency for the m = 0 electrostatic mode. f = 1780 MHz, f_c = 2.7 GHz and a = 4.39 cm.

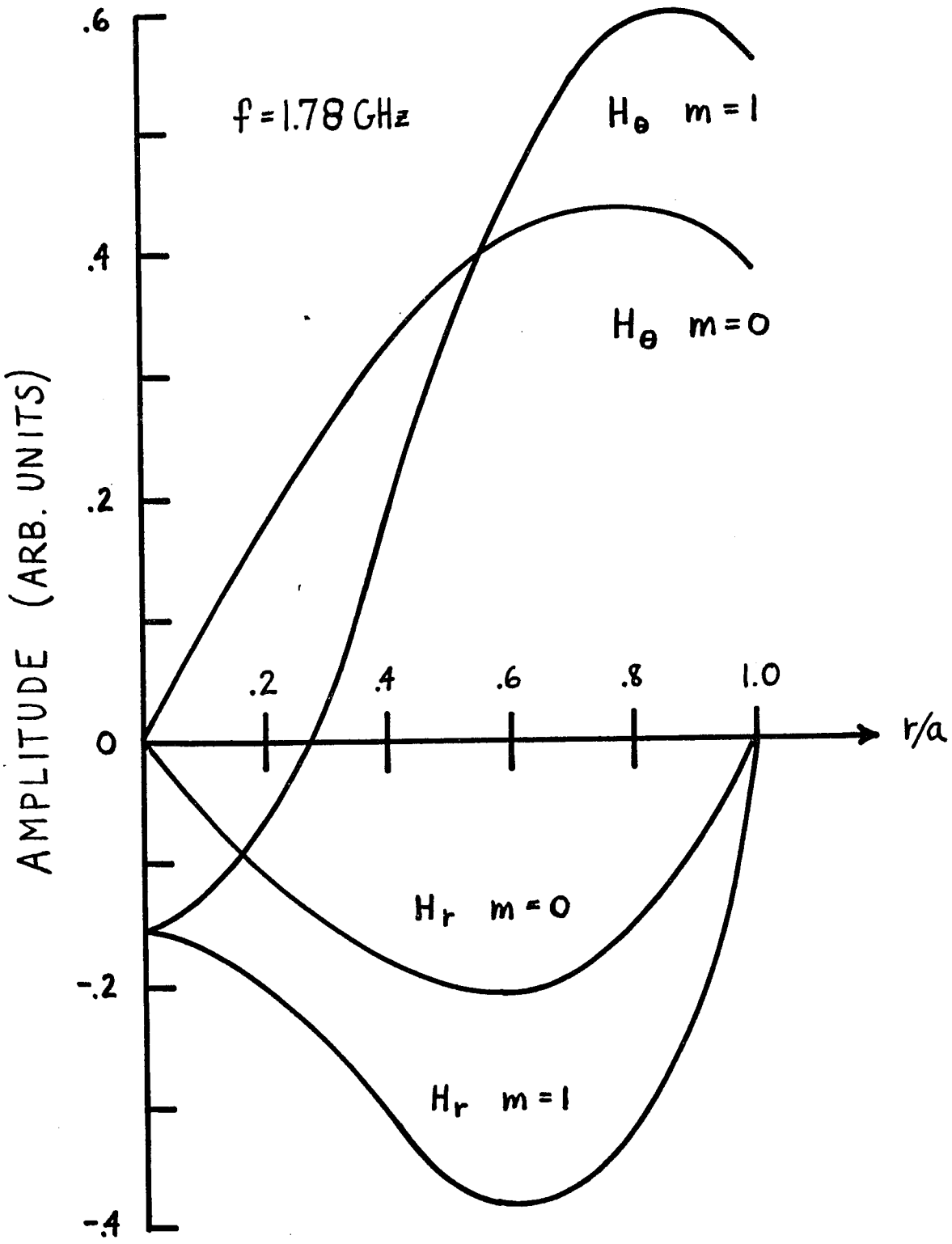
f = 1.78 GHz
H_θ m = 1
H_θ m = 0
H_r m = 0
H_r m = 1
AMPLITUDE (ARB. UNITS)
.6
.4
.2
0
-.2
-.4
.2
.4
.6
.8
1.0
r/a

FIGURE 13

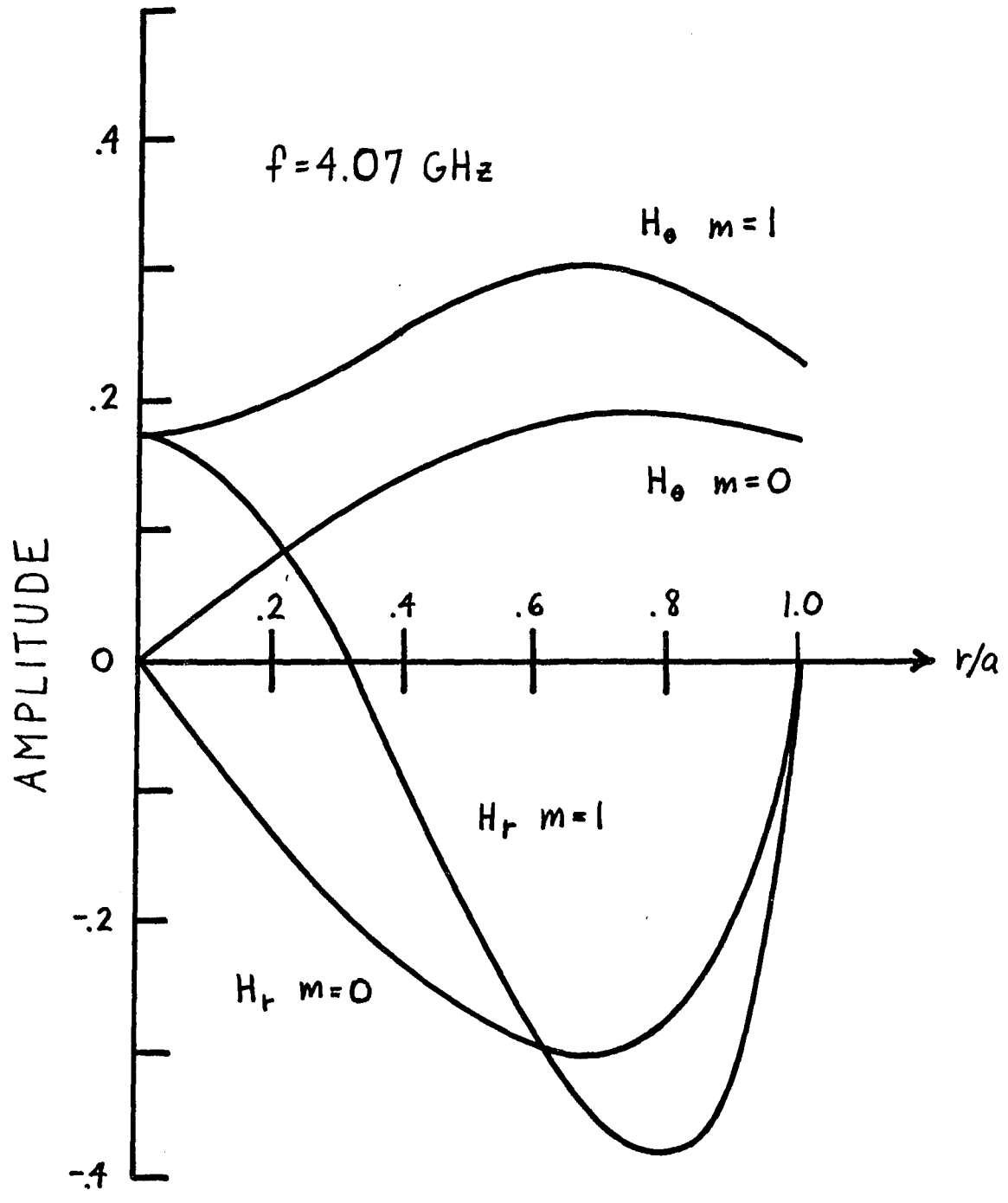
f=4.07 GHz
H_θ m=1
H_θ m=0
H_r m=1
H_r m=0
AMPLITUDE
.4
.2
0
-.2
-.4
.2
.4
.6
.8
1.0
r/a

FIGURE 14

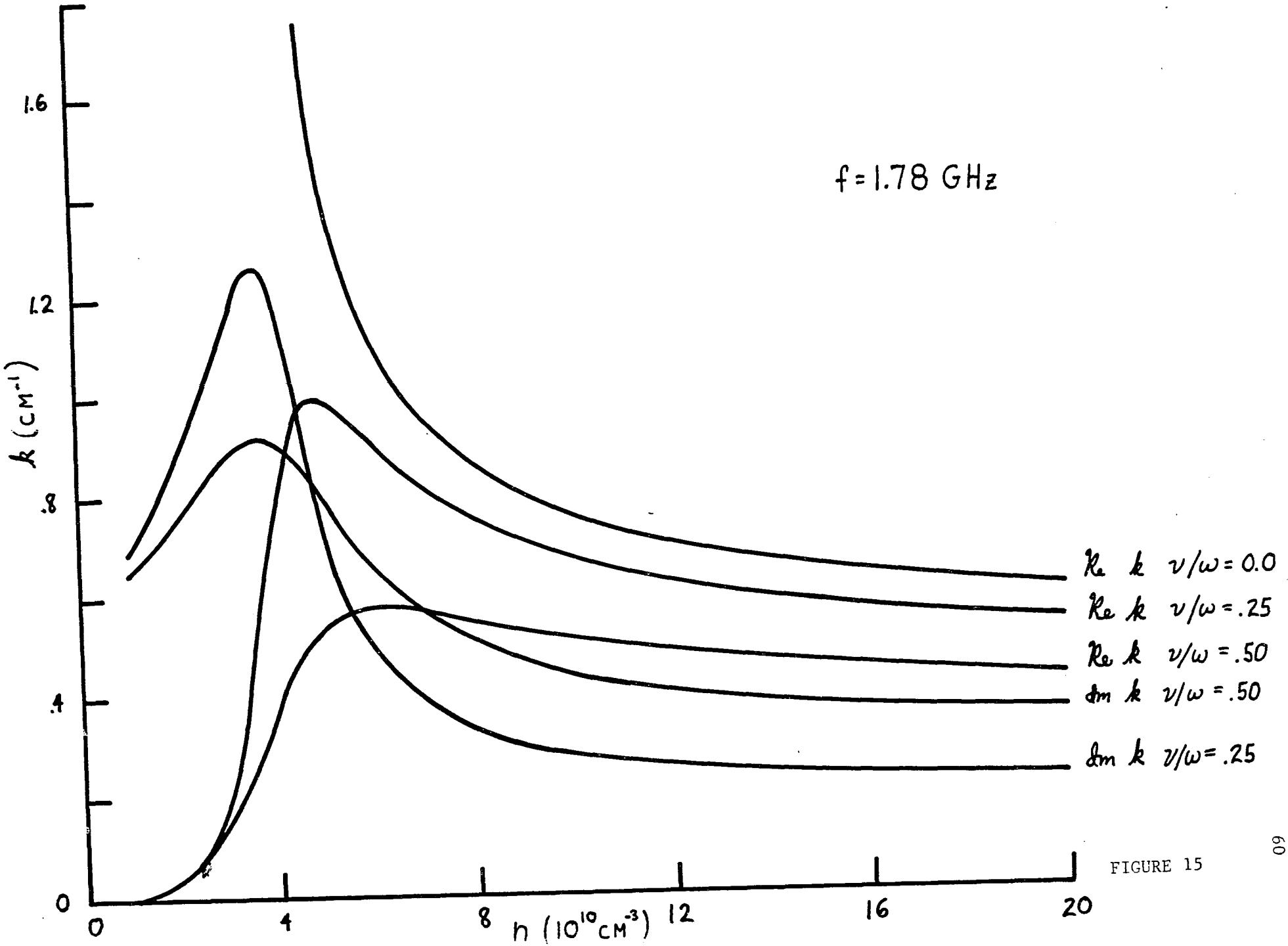
f = 1.78 GHz
k (CM⁻¹)
1.6
1.2
.8
.4
0
0
4
8
12
16
20
n (10¹⁰ CM⁻³)
Re k ν/ω = 0.0
Re k ν/ω = .25
Re k ν/ω = .50
Im k ν/ω = .50
Im k ν/ω = .25

FIGURE 15

6 - REFERENCES

1. G. Schmidt, Physics of High Temperature Plasmas, Academic Press (1966) pp. 5-9.

2. W.P. Allis, S.J. Buchsbaum and A. Bers, Waves In Anisotropic Plasmas, M.I.T. Press (1963), Chapt. 1.

3. J. Stix, The Theory of Plasma Waves, McGraw-Hill Book Co. (1962) pp. 9-12.

4. L. Tonks and I. Langmuir, Physical Review 33, 195 (1929).

5. Reference 3, Chapter 9.

6. B.D. Fried and S.D. Conte, The Plasma Dispersion Function, Academic Press (1961).

7. B.D. McVey and J.E. Scharer, Physics of Fluids 17, 142 (1974).

8. J.H. Stix, Physics of Fluids 1, 308 (1958).

9. Reference 2, Chapter 9.

10. D.G. Swanson, Physics of Fluids 10, 428 (1967).

11. A.W. Trivelpiece and R.W. Gould, Journal of Applied Physics 30, 1784 (1959).

12. Reference 2, pp. 253-254.

13. Reference 3, p. 39.

III APPARATUS AND DIAGNOSTICS

1 - APPARATUS

Figure 16 shows the experimental apparatus. An electromagnetic wave is launched from a rectangular S-band waveguide into the vacuum chamber. The wave then propagates in the vacuum chamber liner which acts as a cylindrical waveguide. The magnetic field profile is designed so that the wave will enter a resonant zone and create a plasma via electron cyclotron resonance which is then contained in the mirror geometry field.

The magnetic field is created by four water cooled coils which are powered by a 15 kilowatt, low ripple, D.C. power supply (Bertan Associates, model 1064). The four coils are equipped with a set of flux return bars which concentrate the return flux so that the field strength inside the coils is approximately that of an infinite solenoid. The field profile is shown in Figure 17. The coils are spaced so that the mirror ratio is 1.25 and the distance between the regions of maxium field is approximately 31 cm. The magnet current is adjusted ($\sim$28.5 amps) so that the electron cyclotron resonant zones are located about 1.5 cm on either side of the midplane. At the resonant zone the field is about 876 Gauss and has a gradient of 7 G/cm.

The vacuum chamber itself is made of 5 inch I.D. stainless steel tubing and the liner consists of a length of thin wall (.51 mm), stainless steel tubing with an I.D. of 8.78 cm. A vacuum seal is made between the rectangular waveguide and the resonant iris. Note that an aluminum baffel

was placed flush with the iris in order to reduce the mismatch between the rectangular and cylindrical waveguide. A radio frequency probe (dipole or loop) or a Langmuir probe can be inserted in the end flange via a vacuum feed through. The feed through is designed so that these probes cannot only be moved axially but can also be swept transversely so that radial profiles can also be measured. Another Langmuir probe can be inserted into the side of the chamber so that radial profiles can be taken on the midplane.

A diamagnetic coil which surrounds the stainless steel liner is located just off the midplane. It is used to monitor the perpendicular plasma pressure $nkT_{e\perp}$. Side ports (not shown in Figure 16) in the chamber also provide access for a K-band microwave interferometer used to measure the average density of the plasma volume at the midplane.

The microwave feed line is shown in Figure 18. S-band microwaves of frequency 2.45 GH_z are generated by an Amperex DX-20G magnetron at power levels of about 1 kW. The magnetron is operated in a pulsed mode controlled by a pulse forming network. The pulse form, shown in Figure 19, has a relatively flat amplitude for about 4 m secs, the entire pulse lasting for about 6 1/2 m secs.

The chamber is evacuated with a 2 inch oil diffusion pump and a liquid nitrogen cold trap pumping system which is capable of a base pressure of about 10^{-7} torr. The working gas is hydrogen at neutral pressures in the 10^{-4} torr range. It is metered into the vacuum chamber by means of a variable leak.

FIGURE CAPTIONS

Fig. 16. Schematic diagram of the experimental appartus. The inside diameter of the cylindrical waveguide is 8.78 cm, the rectangular input waveguide ends at z = +22 cm and the base pressure is $\sim 10^{-7}$ torr.

Fig. 17. The axial magnetic field profile. The mirror ratio is 1.25 and the field at the resonance zones ($z = \pm 1.5$ cm) is about 876 Gauss.

Fig. 18. Schematic of the input microwave system which feeds power into the vacuum chamber. Rectangular S-band waveguide is used throughout.

Fig. 19. Oscillogram of typical data. The upper trace is the integrated diamagnetic coil signal, the middle trace is the microwave power in the plasma volume and the lower trace is the input microwave power pulse (crystal rectified). The time scale is 1 ms/cm.

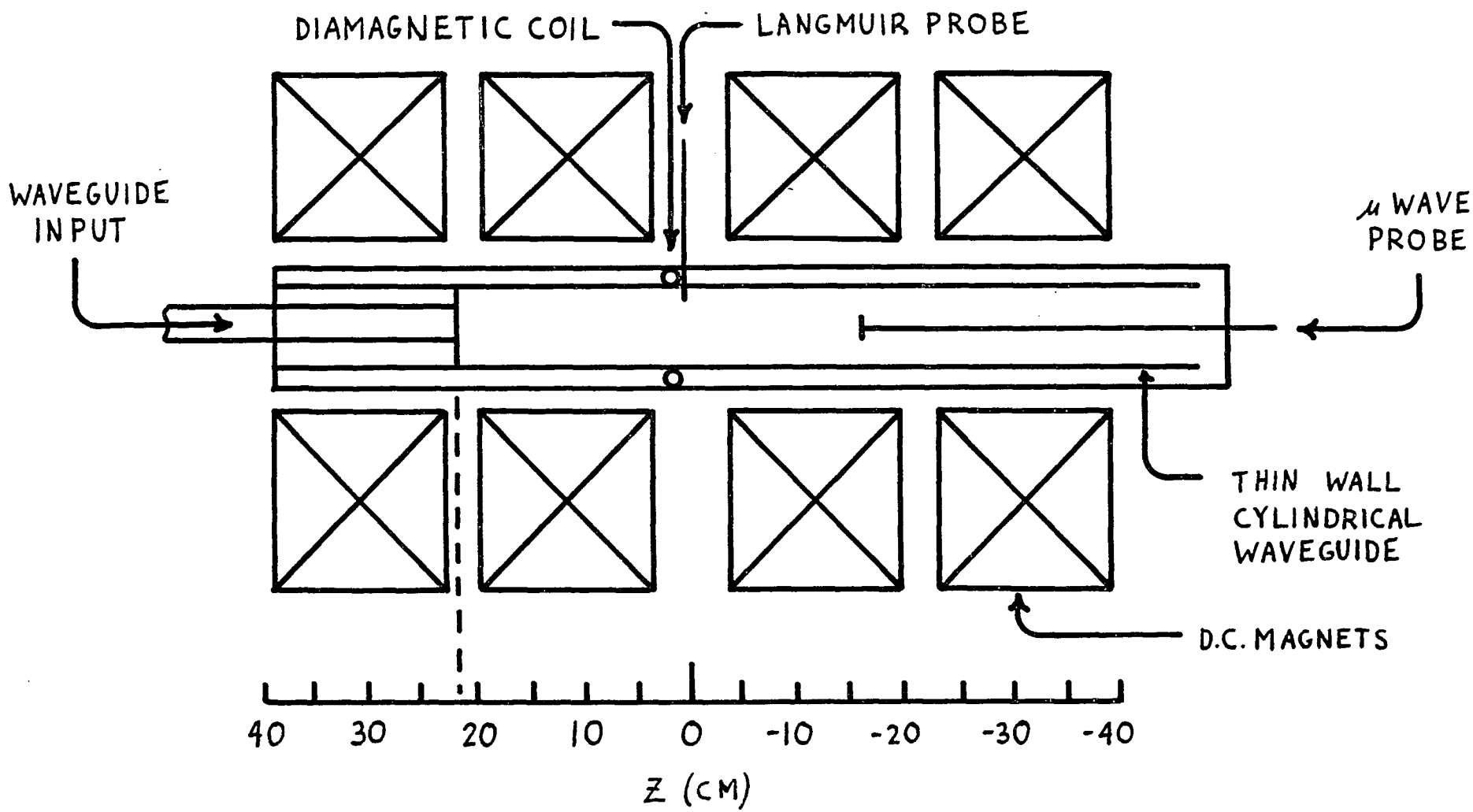
DIAMAGNETIC COIL
LANGMUIR PROBE
WAVEGUIDE INPUT
μ WAVE PROBE
THIN WALL CYLINDRICAL WAVEGUIDE
D.C. MAGNETS
40
30
20
10
0
-10
-20
-30
-40
Z (CM)

FIGURE 16

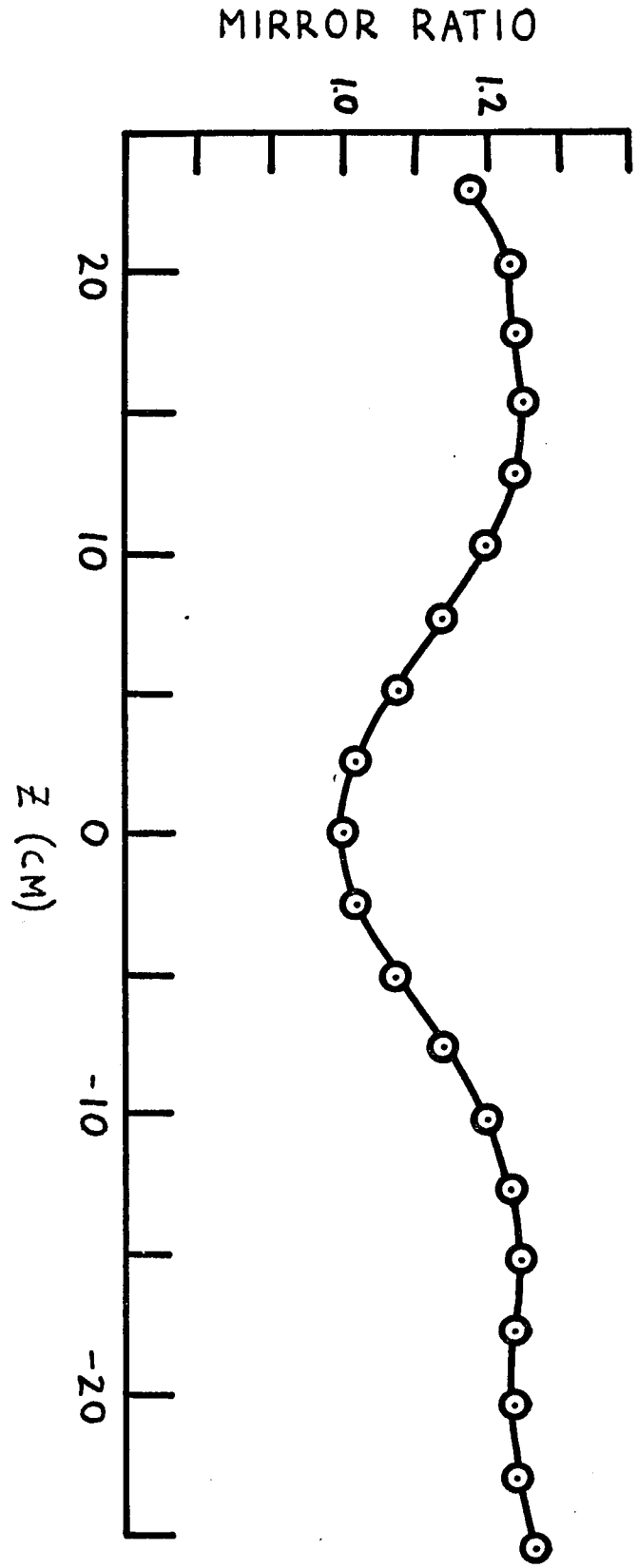

FIGURE 17

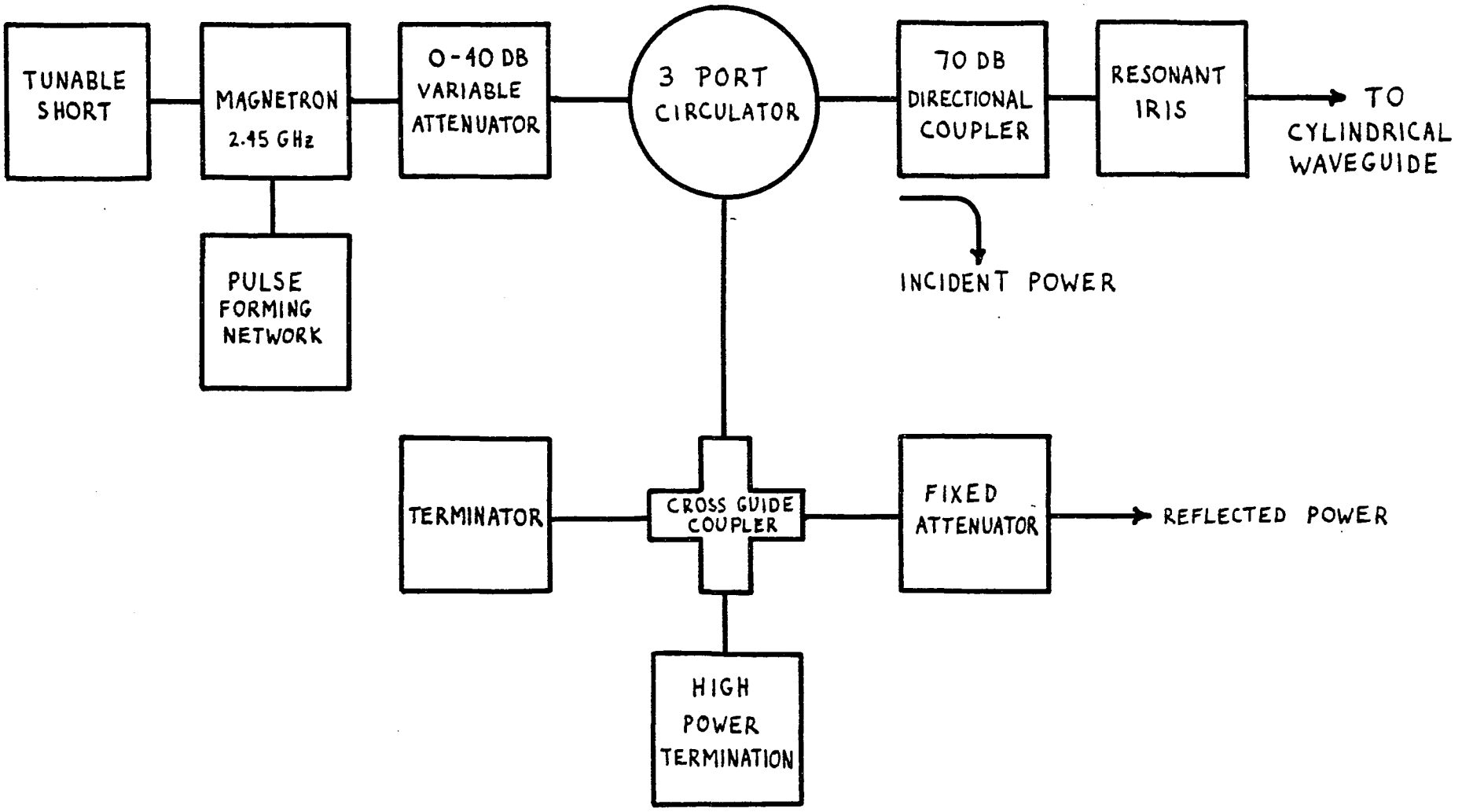
TUNABLE SHORT
MAGNETRON 2.45 GHz
PULSE FORMING NETWORK
0-40 DB VARIABLE ATTENUATOR
3 PORT CIRCULATOR
70 DB DIRECTIONAL COUPLER
RESONANT IRIS
TO CYLINDRICAL WAVEGUIDE
INCIDENT POWER
TERMINATOR
CROSS GUIDE COUPLER
FIXED ATTENUATOR
REFLECTED POWER
HIGH POWER TERMINATION

FIGURE 18

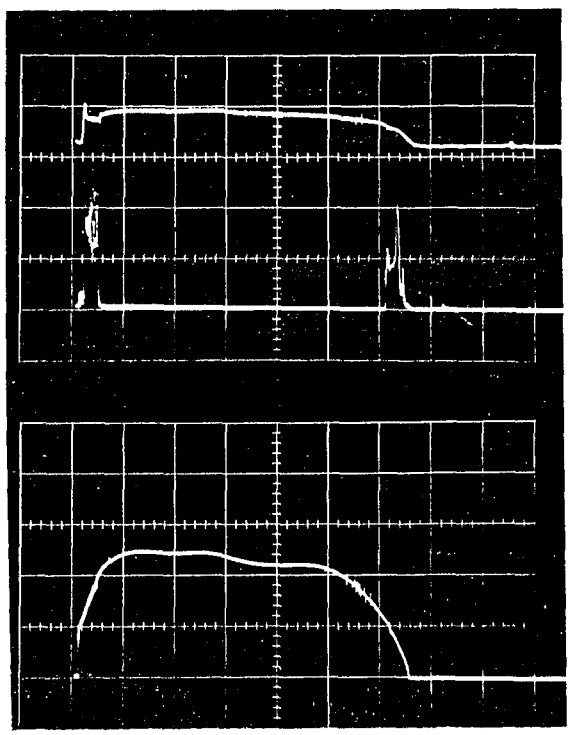

DIAMAGNETIC

RF POWER

INCIDENT POWER

1.0 MS/CM

FIGURE 19

2 - MICROWAVE INTERFEROMETER

The K-band interferometer bridge is shown in Figure 20. Two microwave horns were mounted in the sides of the cylindrical waveguide at the midplane of the mirror machine in order to propagate a small amplitude signal at frequencies of about 20 GHz across the magnetic field. This gives a measurement of the average density of the plasma across the midplane.

The K-band signal is split up into two branches, one which passes through the plasma and the other branch serving as a reference. The signals from these two branches are combined in a magic tee[1] which adds the two signals in one arm and subtracts them in the other. Thus, if R and P represent the signals in the reference and plasma branches respectively and is the phase difference between R and P, then the power in the additive (max) arm of the magic tee is $R^2 + P^2 + 2RP \cos\theta$ while the power in the other (null) arm is $R^2 + P^2 - 2RP \cos\theta$. Initially R and P are adjusted to be equal in amplitude and θ is adjusted to be zero. When a plasma is formed in the waveguide, it decreases the index of refraction in that branch which causes a phase shift of $\Delta\theta$. This will then produce changes in the power levels of the two arms of the magic tee which are monitored. If the signals in the two arms are subtracted, the phase shift can be determined.

Once $\Delta\theta$ has been found, the plasma density can be calculated as follows: the dispersion relation for propagation across the static magnetic field is given by [2]

$$n^2 = \frac{k^2 c^2}{\omega^2} = 1 - \frac{\omega_p^2}{\omega^2} \qquad (101)$$

This is a purely transverse linearly polarized electromagnetic wave with the oscillating electric field vector pointing in the direction of the static magnetic field and thus is not effected by the magnetic field. If $\omega_p^2 << \omega^2$ (as it is for this experiment), then the index of refraction becomes

$$n \approx 1 - \frac{1}{2} \frac{\omega_p^2}{\omega^2} \tag{102}$$

The average density across a path length of 2a is given by [3]

$$\bar{n} = \frac{4\pi c\, m \epsilon_o}{q^2} \frac{f\,\Delta\theta}{2a} \tag{103}$$

where f is in hertz and $\Delta\theta$ is in radians.

A typical set of data is shown in Figure 21. By reading the power levels in the max and null arms and the transmitted power, the phase shift can be measured before and after absorption.

The average density measured for two different frequencies both before and after absorption are given in the table below:

FREQUENCY (GHz)	$\bar{N}$ BEFORE $x10^{11}$ cm^{-3}	$\bar{N}$ AFTER $x10^{11}$ cm^{-3}
19.775	2.6±.5	3.3±.2
22.000	2.2±.8	2.9±1.0

FIGURE CAPTIONS

Fig. 20. Schematic of the K band microwave interferometer.

Fig. 21. Oscillogram of typical interferometer data. The top trace is the difference signal between the max and null branches. The lower trace is the transmitted power. Time scale =.5 ms/cm, pressure is 2.5×10^{-4} torr. The picture is shown twice to demonstrate reproducibility.

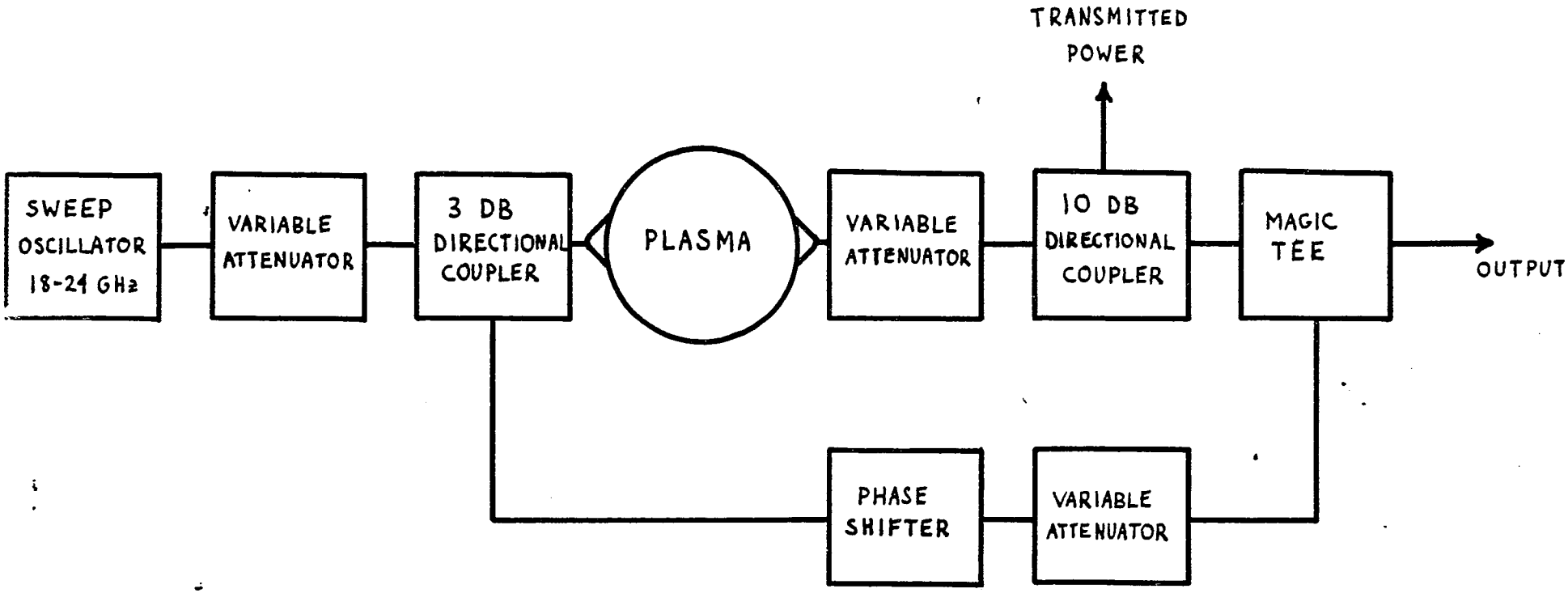
TRANSMITTED
POWER
SWEEP
OSCILLATOR
18-24 GHz
VARIABLE
ATTENUATOR
3 DB
DIRECTIONAL
COUPLER
PLASMA
VARIABLE
ATTENUATOR
10 DB
DIRECTIONAL
COUPLER
MAGIC
TEE
OUTPUT
PHASE
SHIFTER
VARIABLE
ATTENUATOR

FIGURE 20

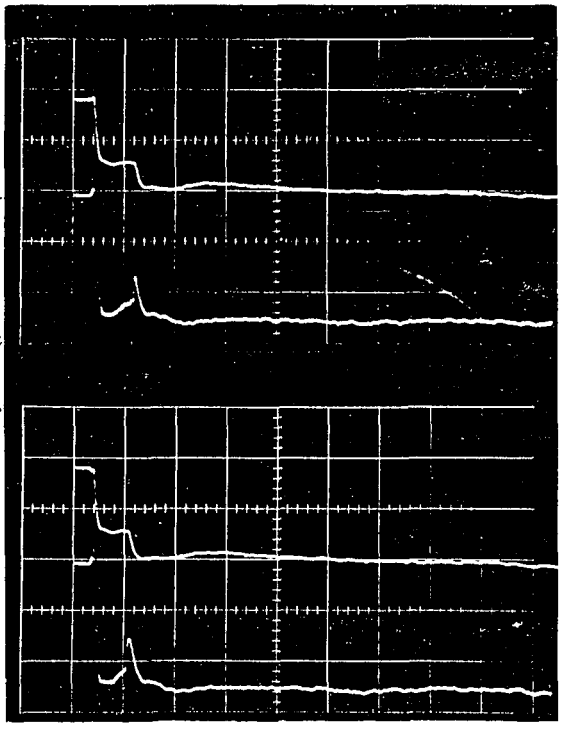

DIFFERENCE SIGNAL

TRANSMITTED POWER

0.5 MS/CM

FIGURE 21

3 - LANGMUIR PROBES

Both radial and axial Langmuir probes were used to measure the local plasma density and temperature. The radial probe enters the chamber at the midplane through a port in the vacuum chamber and a small hole in the side of the cylindrical waveguide. It can only be positioned from the center of the waveguide to the wall. The axial Langmuir probe, on the other hand, was designed to swivel in the vacuum feed through and thus can take radial profiles at any axial position. Both probes consist of a piece of wire which is insulated from the plasma by alumina (except for the end). A diagram of the axial Langmuir probe is shown in Figure 22 .

In order to measure the electron temperature, the probe is biased positively and collects primarily an electron current I_e . For a Maxwellian electron distribution the electron current collected is given by:

$$I_e = I_o \, e^{-\frac{eV}{kT_e}} \tag{104}$$

This expression is valid only up to the point where electron saturation is reached and the probe is space charge limited. The electron temperature can thus be found by making a semi-log plot of I_e versus V and calculating the slope in the linear region. Typical results are shown in Figure 23.

In order to determine the density we note that when the probe is negatively biased, all the electrons are repelled and ions are collected. The ion current density collected is given by:[4]

$$J_i = \frac{I_i}{A} = \frac{n_i e V_{th}}{4} = \frac{n_i e}{4}\left(\frac{2kT_i}{m_i}\right)^{1/2} \tag{105}$$

where A is the area of the probe and $n_i = n_e = n$ for a neutral plasma. The

above expression would simply enable us to calculate the density except for the fact that a negatively charged sheath builds up around the probe (due to the higher mobility of the electrons) which increases the effective collecting area of the probe. When the sheath is thin compared to the radius of the probe and $T_i << T_e$, the current is given by [4]

$$I_i \approx .4\, A\, n_i\, e \left(\frac{2kT_e}{m_i}\right)^{1/2} \tag{106}$$

Thus, if the probe area A is measured and T_e has been determined as above, then it is seen that the density is simply proportional to the ion saturation current which is easily measured. Figures 24 and 25 show typical data.

The above analysis applies only when there is no magnetic field present. If a static magnetic field exists (as does in this experiment), the random flux of particles will be limited because ion Larmor radius can be smaller than the probe radius and the measured density will thus be lower than the true density. This is overcome by using a very thin probe (diameter = 0.0089") but now the sheath will no longer be thin compared to the probe radius. The above thin sheath theory fails and a thick sheath theory must be substituted to account for particles which are not collected because of orbital motions. It can be shown that [5]

$$I_i^2 = \frac{4}{\pi} A^2 j_r^2 \left(1 - \frac{eV}{kT_i}\right) \tag{107}$$

where A is the area of the probe and j_r is the random current density,

$$j_r = .5\, n_i\, e \left(\frac{2kT_i}{\pi m_i}\right)^{1/2}. \tag{108}$$

Therefore, if a plot is made of I^2 versus V, the density can be calculated

by measuring the slope S which is given by

$$S = \frac{2}{\pi^2} A^2 \frac{e^3}{m_i} n_i^2 \tag{109}$$

Note that neither T_e nor T_i must be known as was previously. Typical results are shown in Figure 26.

FIGURE CAPTIONS

Fig. 22. Axial Langmuir probe.

Fig. 23. Radial Langmuir probe data; the electron current on a log scale is plotted versus the applied voltage on a linear scale. The probe was located at r = 1.25 cm.

Fig. 24. Oscillogram of typical Langmuir probe data. The top trace is the intergrated diamagnetic signal coil signal (plasma pressure); the lower trace is the ion saturation current (the voltage drop across a 100 ohm resistor). The radial probe is biased at -50 volts. Vertical gain = 50 mv/cm, time scale = 1.0 ms/cm. Pressure = 2.6×10^{-4} torr and r = 0.

Fig. 25. Oscillogram of typical Langmuir probe data. The top trace is the intergrated diamagnetic signal coil signal (plasma pressure); the lower trace is the ion saturation current (the voltage drop across a 100 ohm resistor). The radial probe is biased at -50 volts. Vertical gain = 50 mv/cm, time scale = 0.1 ms/cm. Pressure = 2.6×10^{-4} torr and r = 0.

Fig. 26. Radial Langmuir probe characteristics both before and after absorption of the left wave. r = 1.25 cm.

AXIAL LANGMUIR PROBE

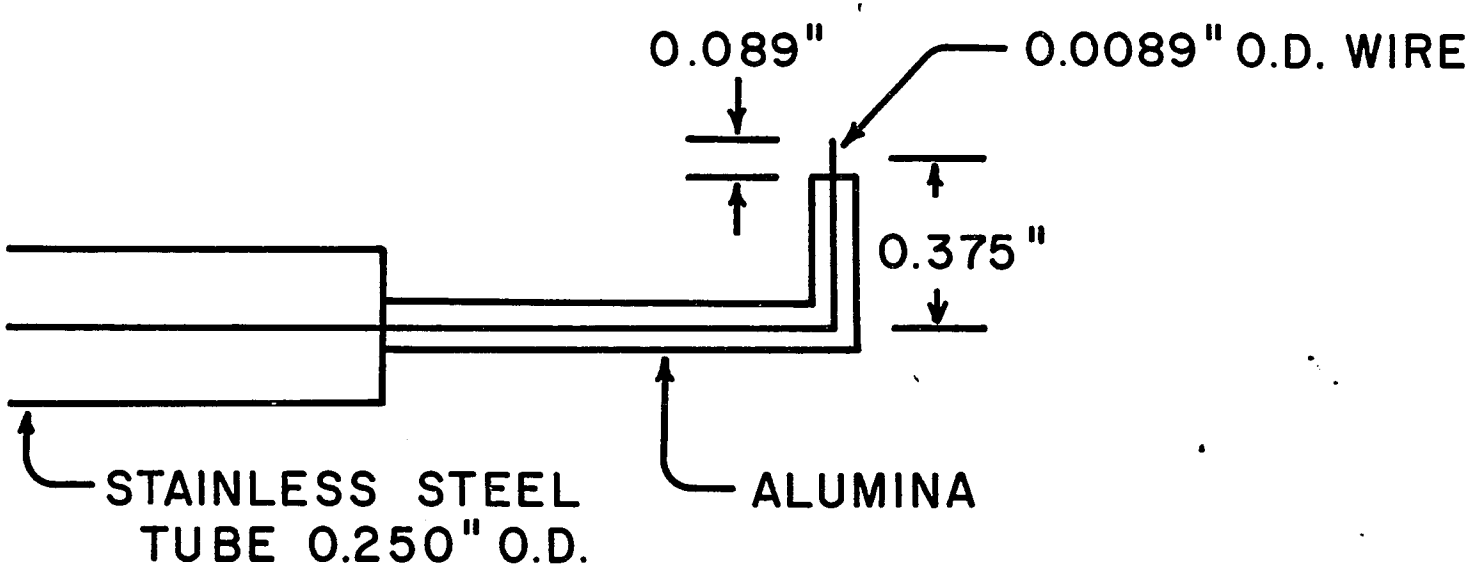

FIGURE 22

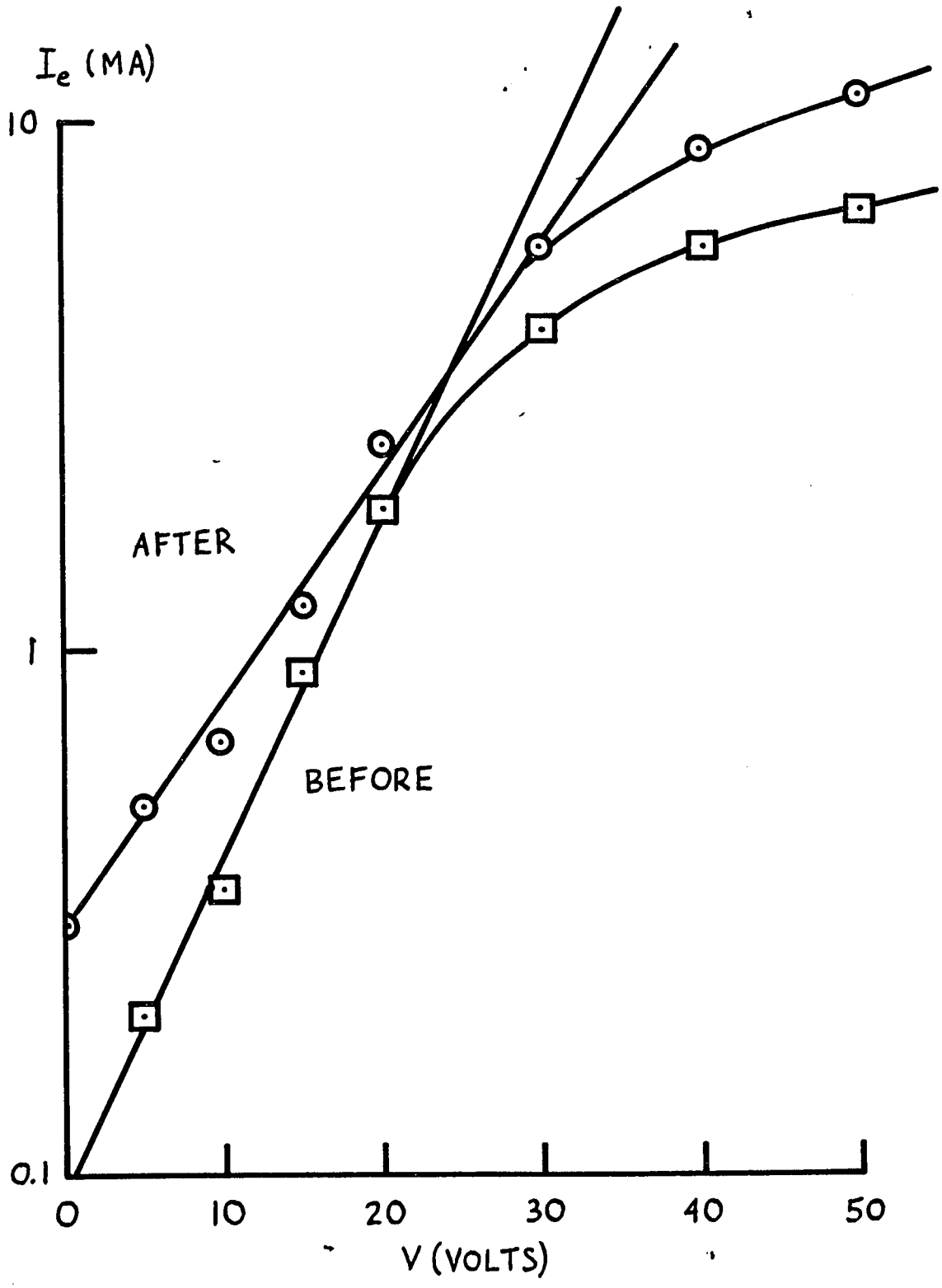

FIGURE 23

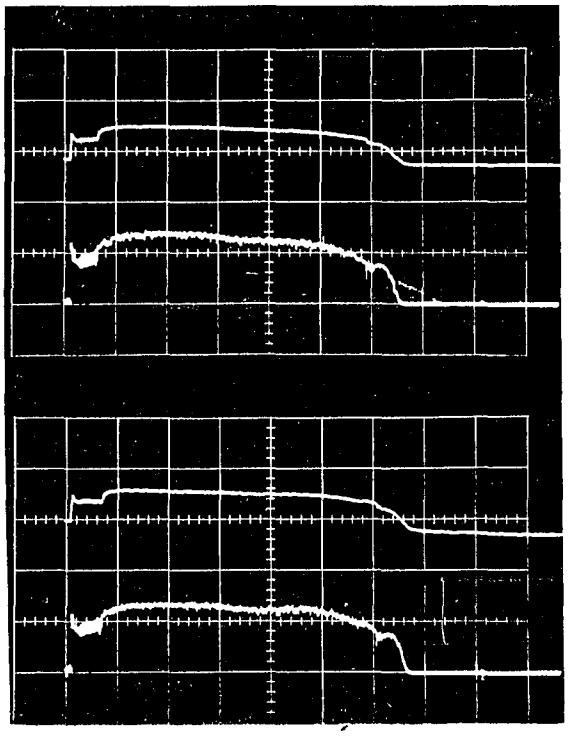

DIAMAGNETIC

ION SATURATION CURRENT

1.0 MS/CM

FIGURE 24

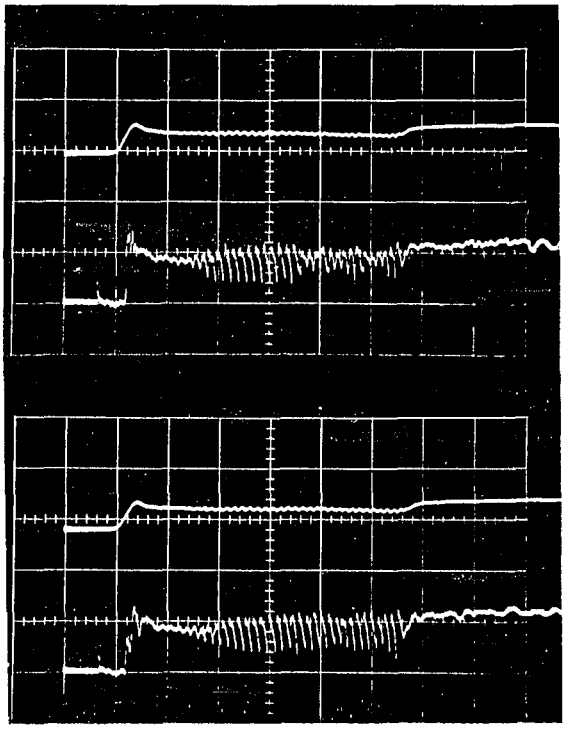

DIAMAGNETIC

ION SATURATION CURRENT

0.1 MS/CM

FIGURE 25

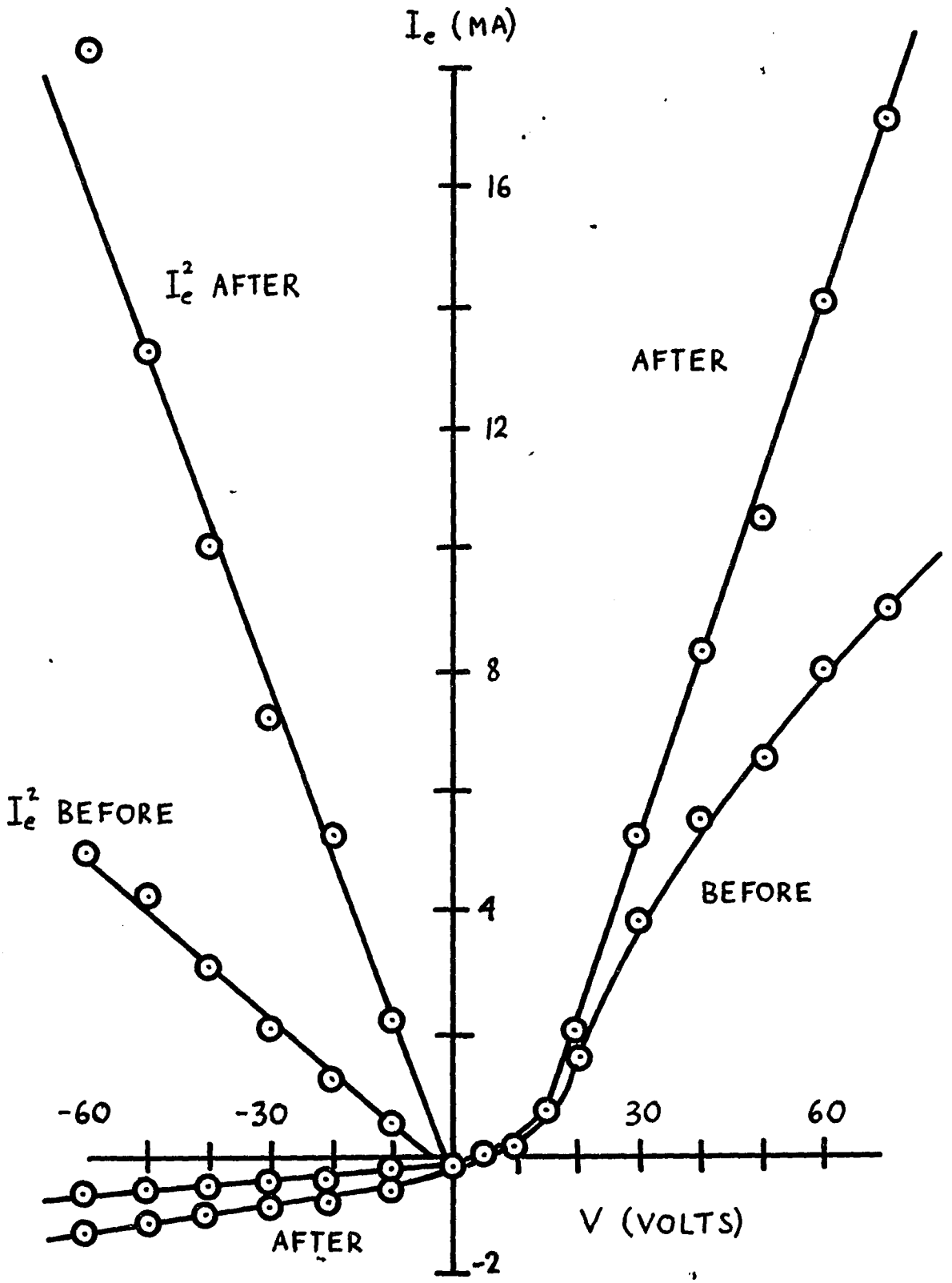
I_e (MA)
16
12
8
4
-2
I_e^2 AFTER
AFTER
I_e^2 BEFORE
BEFORE
-60
-30
30
60
AFTER
V (VOLTS)

FIGURE 26

4 - DIAMAGNETIC COIL

The diamagnetic coil consists of 100 turns of wire wrapped around the stainless steel liner and is located at z= +1 cm (see Figure 16). As the perpendicular plasma pressure $p_\perp = nkT_{e\perp}$ changes, it induces an emf in the coil given by[6]

$$\mathcal{E} = \frac{\mu_o N A}{B_o} \frac{dp_\perp}{dt} \tag{110}$$

where N is the number of turns and A is the area of the coil.

This signal is then integrated by an RC integrating circuit. The voltage across the capacitor is given by[7]

$$V(t) = \frac{\mu_o N A}{RC B_o} p_\perp(t) \tag{111}$$

Typical results are shown in Figure 27. The voltage response before absorption is about 40 mv which corresponds to a pressure of 0.45 N/m^2. During this phase small ripples appear on the trace which corresponds to the ion acoustic oscillation observed on the RF signal. Absorption is clearly seen on the diamagnetic signal as a rise in the perpendicular pressure of up to 50%. Since density measurements (Langmuir probe and interferometer) indicate no appreciable change in average density after absorption, this 50% rise can be attributed to a rise in the prependicular electron temperature.

FIGURE CAPTIONS

Fig. 27. Oscillogram of typical data. The top trace is the intergrated diamagnetic coil signal (plasma pressure) with RC = 100 μs, the middle trace is crystal rectified RF probe signal and the bottom trace is the incident microwave power. The RF loop probe was located at z =-15.2 cm and r = 0. Time scale = .2 ms/cm.

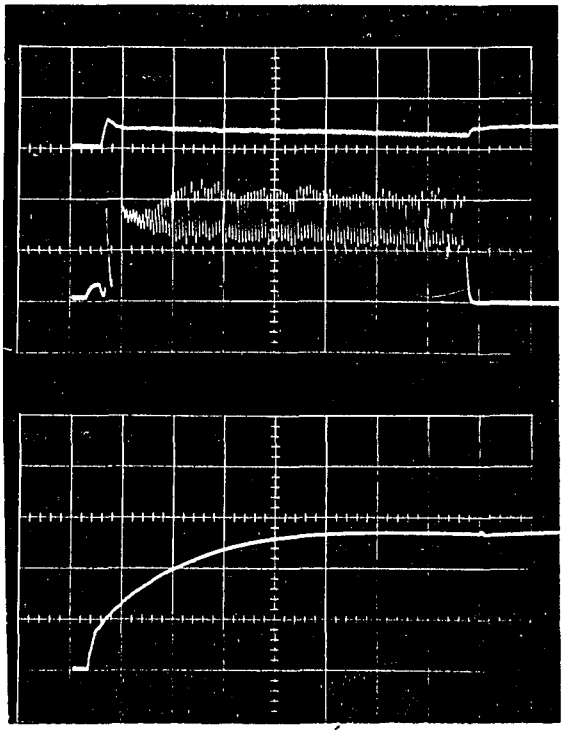

DIAMAGNETIC

RF POWER

INCIDENT POWER

0.2 MS/CM

FIGURE 27

5 - RADIO FREQUENCY PROBES

In order to detect the wave field in the waveguide a dipole probe was used to sample the electric fields E_r and E_θ and a magnetic loop pickup was used to sample H_r and H_θ. Either probe is introduced into the chamber via a vacuum feed through on the end flange just as the axial Langmuir probe. These probes are capable of taking radial profiles at all axial positions. The signal from these probes is fed into a crystal detector whose rectified output is proportioned to the power received by the probe when the crystal is operated in its linear region. In order to measure the wave fields for any particular frequency, the probe output was fed directly into a microwave receiver (Polarad Model R) which has a video output proportional to the field received. With various plug-in units this receiver is capable of detecting frequencies of 900-2,000 MH_Z and 2,000-4,000 MH_Z.

Sample data of the RF plasma response for the crystal and the receiver are shown in Figures 27 and 28.

The dipole probe has a length of 1.3 cm and is connected to 0.9 mm O.D. coaxial cable. So as not to pick up any plasma currents, the probe and the cable are insulated from the plasma with alumina tubing and epoxy. The magnetic probe consists of a piece of coaxial cable which is bent into a 1 cm diameter loop. The inner conductor is spot welded to the outer casing and again care is taken to insulate the probe from the plasma. Diagrams of these probes are shown in Figures 29 and 30.

The probes do have finite size and it is possible to couple to another

field component or components other than those for which the probe was designed. In order to test the dipole probe, E_θ and E_r were measured in the vacuum waveguide where only the dominant TE_{11} mode can exist[8] at f = 2.45 GHz. The results are shown in Figure 31. The E_θ points give a good fit to the theoretical curve but the E_r response falls off faster than predicted. This is because the probe has a finite size and is coupling to E_θ as well as E_r .

Similar results are shown for the loop probe in Figure 32. Again the poor agreement for the H_θ profile can be attributed to the finite probe size, but in addition now the probe could also pick up some H_z component which is present in the TE_{11} mode. This effect becomes more important as the probe is moved off axis thus exposing more of its area to the axial direction.

Another problem with the loop probe is that it may be capable of coupling to the electric fields as well as the magnetic fields. For example, in the vacuum guide H_r and E_θ both have the same radial profile, namely

$$H_r, E_\theta \sim J_1(\chi_{11}\, r/a) \tag{112}$$

where χ_{11} is the first root of $J_1'(\chi_{11}) = 0$ and a is the waveguide radius. To test that the probe is responding to H rather than E a TM_{010} mode microwave cavity was constructed. For this mode the only fields present are[9]

$$E_z \sim J_0(\chi_{01}\, r/a) \tag{113}$$

$$H_\theta \sim J_1(\chi_{01}\, r/a) \tag{114}$$

where χ_{01} is the first root of J_0. The results are shown in Figure 33 . The data is only in fair agreement with H_θ . The signal at r = O drops only to 10% in power rather than to zero. This is probably due to the probe coupling to E_z which is greatest at r = O. Thus, it is seen that the loop probe can effectively be used to measure magnetic field profiles even when an electric field is present.

FIGURE CAPTIONS

Fig. 28. Oscillogram of receiver response at f = 1685 MHz. The unrectified RF loop probe signal is fed into the microwave receiver. $p = 2.5 \times 10^{-4}$ torr, z = -12.7 cm, r = 0 and .2 ms/cm.

Fig. 29. RF dipole probe.

Fig. 30. RF loop probe.

Fig. 31. The square root of the RF dipole response, in the vacuum guide (normalized) is plotted versus the normalized radial position r/a. The curves are the calculated vacuum guide fields for the TE_{11} mode.

Fig. 32. The square root of the RF loop probe response, in the vacuum guide (normalized) is plotted versus the normalized radial position r/a. The curves are the calculated vacuum guide fields for the TE_{11} mode.

Fig. 33. The square root of the RF loop probe response (normalized) in the microwave test cavity is plotted for different radial position. The curves are the cavity fields for the TM_{010} mode.

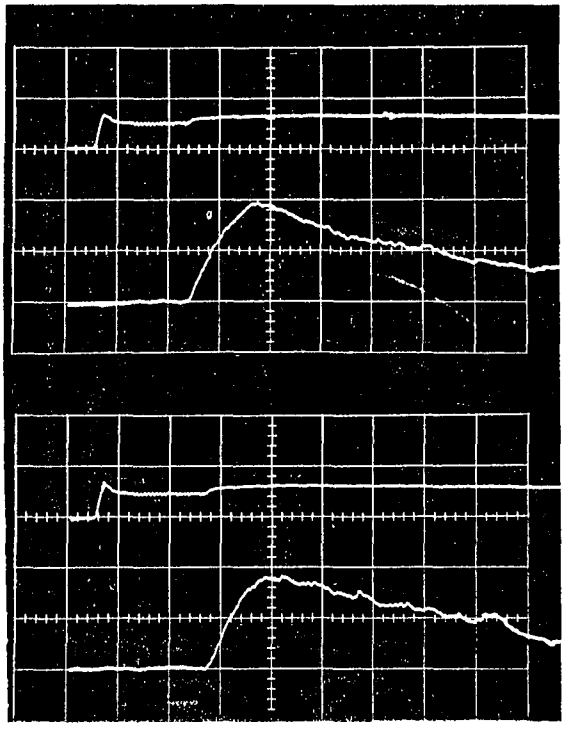

DIAMAGNETIC

RF AT 1685 MHz

0.2 MS/CM

FIGURE 28

DIPOLE PROBE

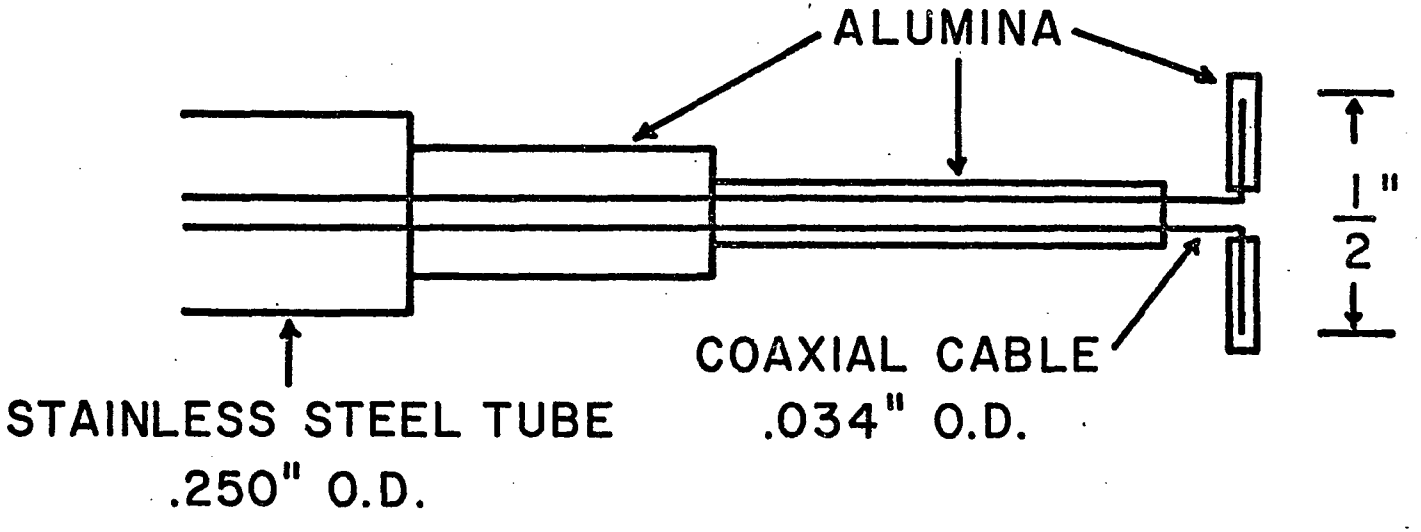

FIGURE 29

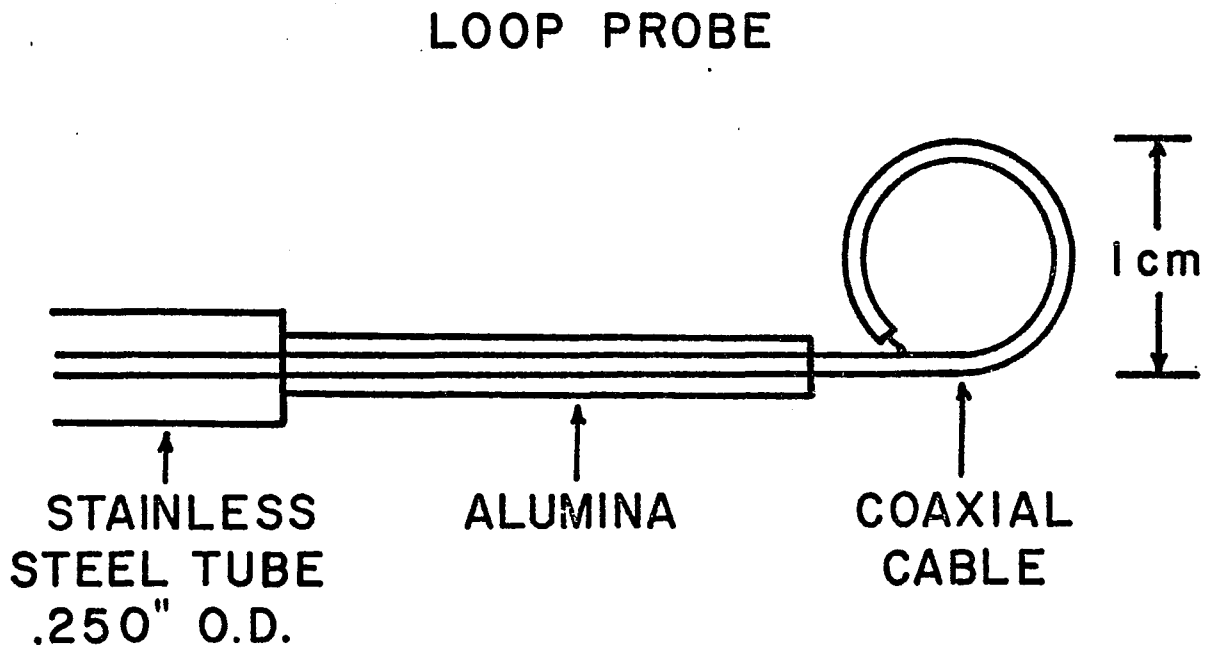
LOOP PROBE
1 cm
STAINLESS
STEEL TUBE
.250" O.D.
ALUMINA
COAXIAL
CABLE

FIGURE 30

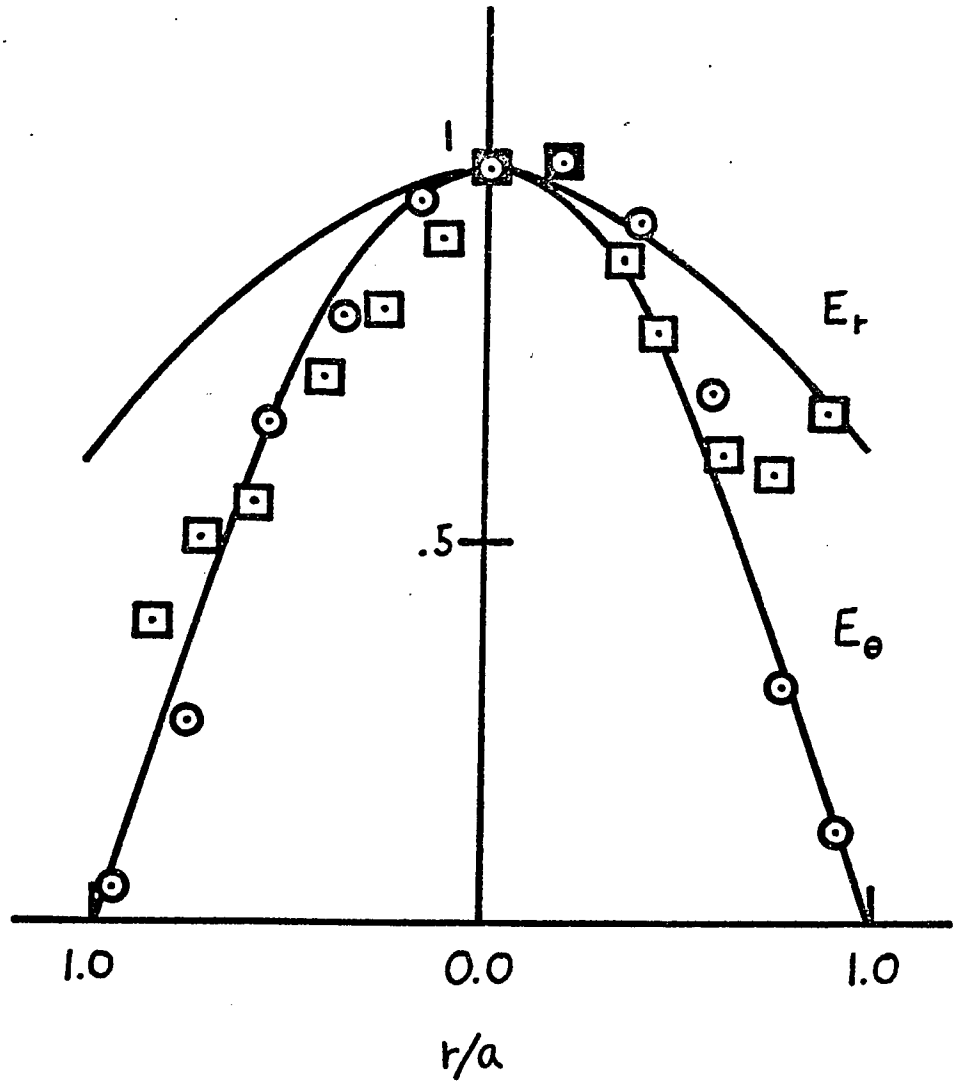

FIGURE 31

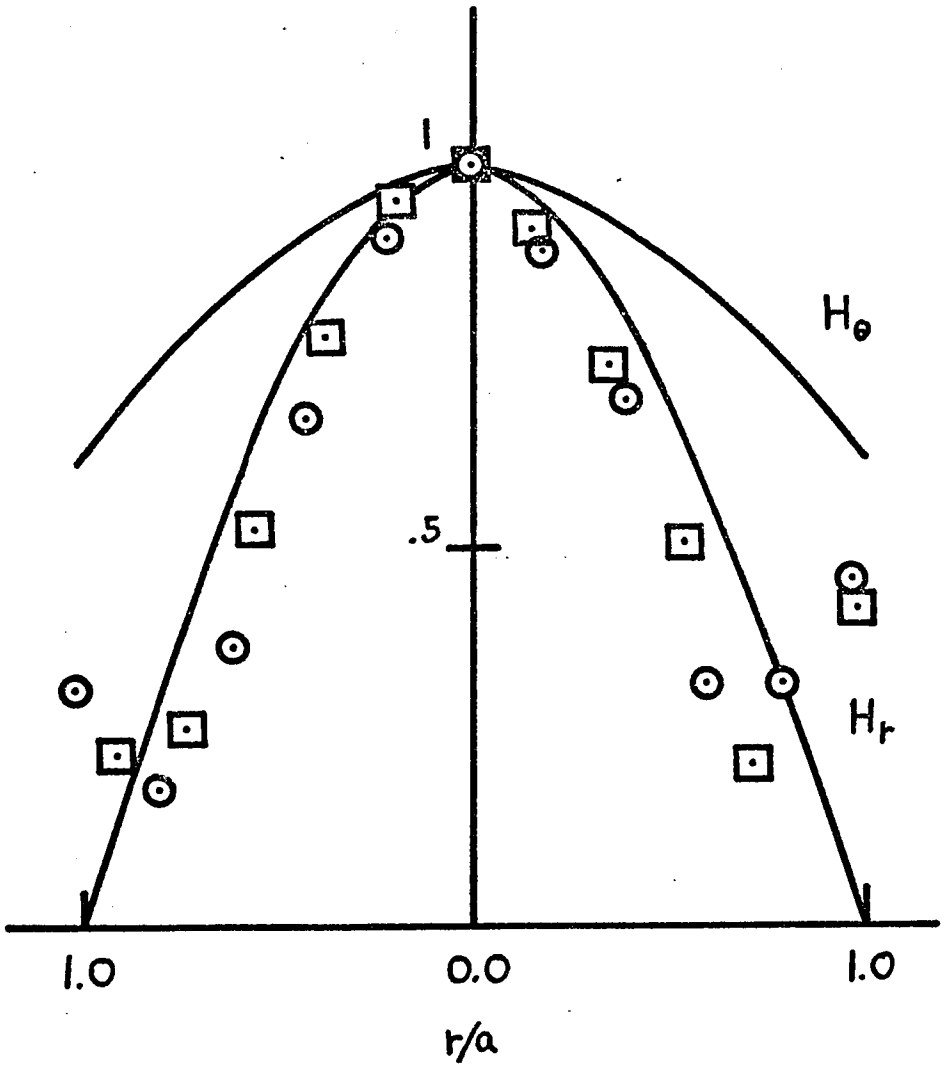

FIGURE 32

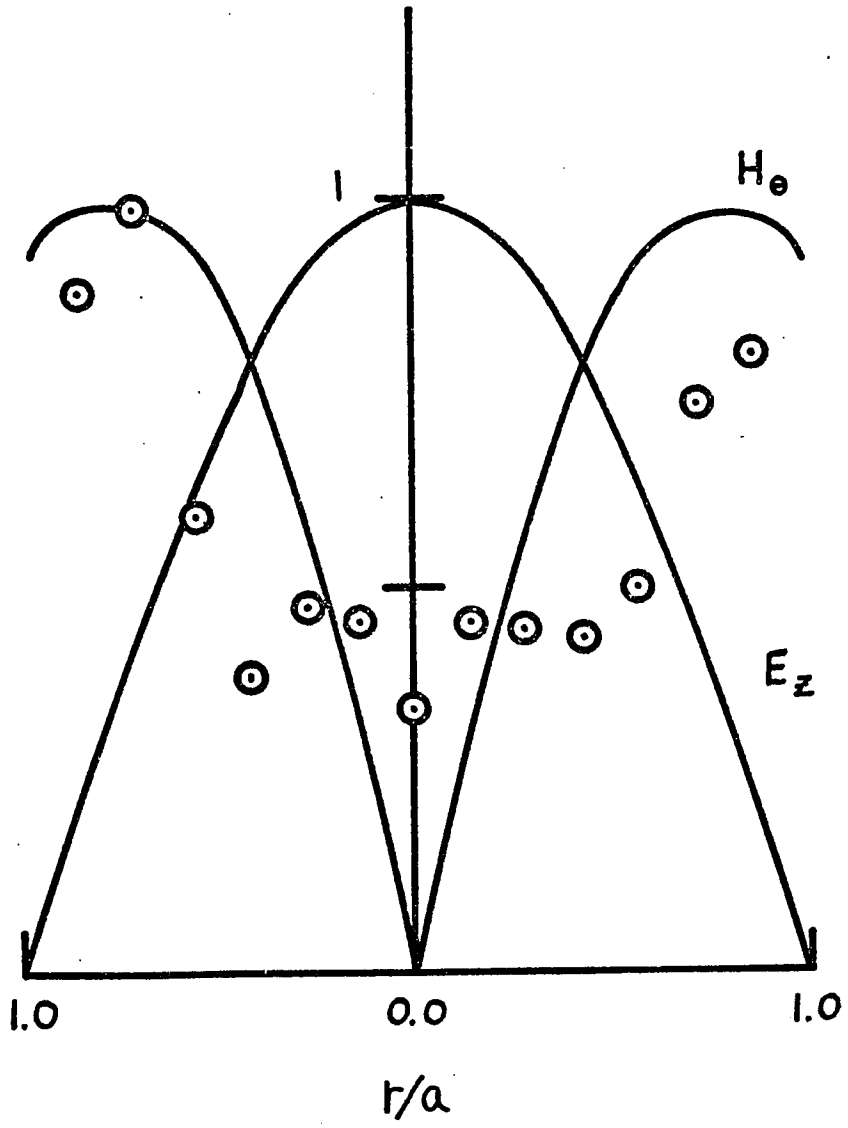

FIGURE 33

6 - REFERENCES

1. R.E. Collin, Foundations For Microwave Engineering, McGraw-Hill Book Co. (1966) pp. 282-284.

2. G. Schmidt, Physics of High Temperature Plasmas, Academic Press (1966) p. 235.

3. M.A. Heald and C.B. Wharton, Plasma Diagnostics with Microwaves, John Wiley and Sons, Inc. (1965) pp. 120-123.

4. Ibid, pp. 378-380.

5. R.H. Huddlestone and S.L. Leonard, Plasma Diagnostic Techniques, Academic Press (1965) pp. 128-131.

6. N.A. Krall and A.W. Trivelpiece, Principles of Plasma Physics, McGraw-Hill Book Co. (1973) pp. 628-629.

7. R.H. Huddlestone and S.L. Leonard, pp. 8-9.

8. R.E. Collin, pp. 107-111.

9. J.D. Jackson, Classical Electrodynamics, John Wiley and Sons, Inc. (1962) pp. 252-254.

IV - EXPERIMENTAL RESULTS

In experiments performed with the previously described apparatus, a plane linearily polarized electromagnetic wave of frequency 2.45 GHz propagating in the dominant TE_{10} mode in the rectangular S-band waveguide (cutoff frequency = 2.08 GHz) is launched into a cylindrical waveguide (vacuum cutoff frequency = 2.00 GHz). The right hand component of the incident wave interacts with the electrons in a magnetic beach arrangement to create an electron cyclotron plasma. The left hand component of the incident wave should either be reflected if the plasma is overdense or be transmittedthrough the plasma if it is underdense, to a wave of that frequency.

Figure 34 is an oscillogram showing the response of the diamagnetic coil and the RF dipole probe along with the incident power. Figure 35 shows the same parameters but now on an expanded time scale. These oscillograms reveal several interesting phenomena during the time of the incident power pulse. Initially, the plasma builds up; this is best seen on the diamagnetic trace indicated by a sharp rise in plasma pressure $nkT_{e\perp}$. During this phase the RF response undergoes several large amplitude fluctuations which is attributed to a rapidly changing standing wave pattern as the plasma is created. Next we observe that an equilibrium ($dp_\perp/dt \approx 0$) is reached. This is indicated by the constant amplitude diamagnetic and RF responses. The modulation of both these signals by low frequency oscillations is very apparent. These modulations have a frequency of about 75 kHz and have been identified

as ion acoustic waves.[1] It is also noted that the RF signal level is such that substantial power is present at the probe position, which indicates that the left wave is being transmitted. Density measurements during this phase find that $n \simeq 2 \times 10^{11}$ cm^{-3}. Cold plasma theory predicts (see theory section, Figure 9) that the left wave should be cutoff for densities above 6.6×10^{10} cm^{-3}, thus the observed transmission can be termed anomalous.

After a period of time the RF signal essentially drops to zero with a concurrent increase in the plasma pressure. At the same time the reflected power also decreases from $\approx$ 30% to $\approx$ 4%. Density measurements indicate that the average density remains essentially unchanged at this time, thus we attribute the rise in the diamagnetic signal to an increase in the temperature. This is interpreted to be anomalous absorption of the incident left hand wave.

Each of the above phenomena will now be discussed in more detail.

FIGURE CAPTIONS

Fig. 34. Oscillogram of typical data. The top trace is the intergrated diamagnetic coil signal (plasma pressure), the middle trace is the crystal rectified RF dipole probe response (z = -15.2 cm) and the bottom trace is the incident microwave power. Time scale = 1 ms/cm.

Fig. 35. Oscillogram of typical data. The top trace is the intergrated diamagnetic coil signal (plasma pressure), the middle trace is the crystal rectified RF dipole probe response (z = -15.2 cm) and the bottom trace is the incident microwave power. Time scale = 0.1 ms/cm.

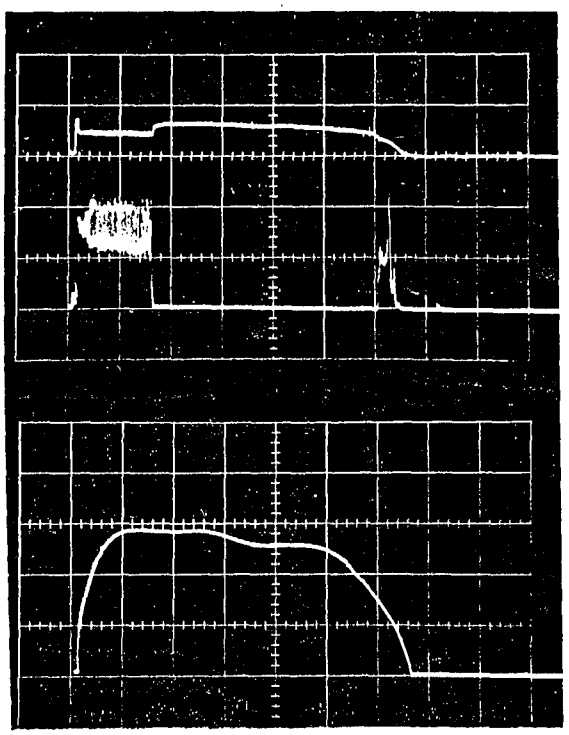

DIAMAGNETIC

RF POWER

INCIDENT POWER

1.0 MS/CM

FIGURE 34

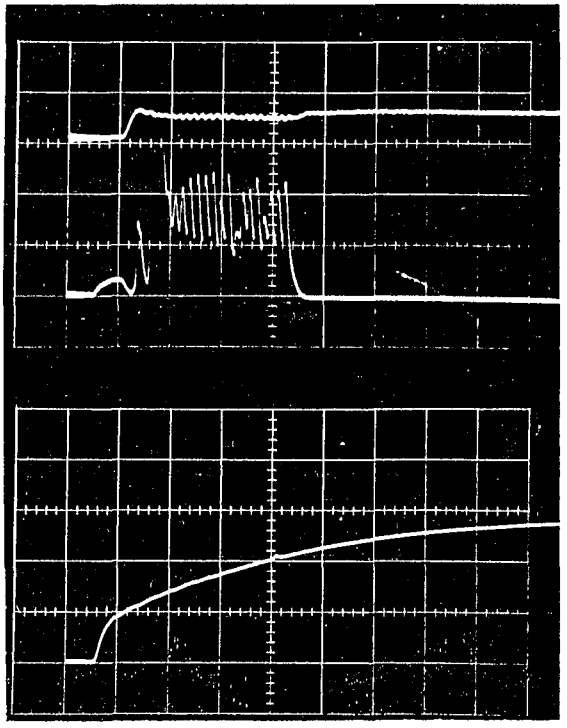

DIAMAGNETIC

RF POWER

INCIDENT POWER

0.1 MS/CM

FIGURE 35

1 - ION ACOUSTIC WAVES

The appearance of low frequency ($\sim$ 75 kHz) modulations can be clearly seen on the diamagnetic and RF signals (see Figures 34and35). These oscillations are also observed with a high impedance electrostatic probe and on the Langmuir probe data. They are interpreted to be density fluctuations due to ion acoustic waves.

The dispersion relation for these waves is given by [2]

$$\frac{1}{\omega^2} = \frac{1}{k_z^2}\left(\frac{m_i}{k T_e}\right) + \frac{1}{\omega_{pi}^2} \tag{115}$$

and in the long wavelength limit (of interest here), equation (115) can be written as

$$\frac{\omega}{k_z} = \sqrt{\frac{k T_e}{m_i}} \tag{116}$$

The wavelength was measured by comparing the phase of the modulations of the diamagnetic signal to the RF power modulations for different axial positions. The RF probe was moved axially until a phase shift of $\pi/2$ radians was noted. These measurements yield a result of $\lambda = 40 \pm 8$cm. When this value of λ and a typical value of $T_e = 8 \pm 1$ e V are inserted into equation (116), the result is f = 69 $\pm$ 11 kHz. This is in good agreement with the measured value of 75 kHz.

When the effects of a static magnetic field and cylindrical conducting boundaries are included, the dispersion relation for the ion acoustic waves is [1]

$$\frac{\omega^2}{k_z^2} = \frac{V^2}{1 + (V^2/\Omega^2)(l^2 + k_z^2)} \tag{117}$$

where $V^2 = kT_e/m_i$, $\Omega^{-2} = \omega_{ci}^{-2} + \omega_{pi}^{-2}$, $\omega^2 << \omega_{ci}^2$, ℓa is a root of $J_m(\ell a)$, a is the waveguide radius, and J_m is the ordinary Bessel function of order m. The measured wavelength is long enough so that $k_z^2 << \ell^2$. The azimuthal mode number m is unknown, but when the frequency is calculated from (117) for m = 0 and m = 1 for the parameters of this experiment, the results differ with the value obtained from (116) by only $\approx 2\%$. Again, this is well within the experimental error.

In addition, to demonstrate that the frequency of these waves depends on the ion mass as predicted by (116), frequency measurements were made with neon (atomic weight = 20) and argon (atomic weight = 40) as well as hydrogen. The results are shown in the table below.

Working Gas	Atomic Weight	Measured Frequency (kHz)	Calculated Frequency* (kHz)
H	1	75	75
Ne	20	18	17
Ar	40	6	12

* - The calculated frequency was taken to be the measured frequency for hydrogen and 75 kHz/ $\sqrt{m_i}$ for the other gases.

Although these results are not in good agreement it must be noted that no account was made for any change in T_e or λ.

The magnitude of the density modulation is about 25% but can be as high as 40% at off axis positions. This is not a sufficient reduction in the density to allow the left wave to propagate. In order for this to happen, the ion acoustic waves would have to modulate the density at a magnitude of the order of 70%.

2 - DENSITY PROFILES

Radial density profiles (at z = 0 only) were made with the radial Langmuir probe, while both axial and radial (for various axial positions) were made with the axial Langmuir probe. In plotting these profiles, the ion saturation current was used because, as was shown previously, it is directly proportional to the plasma density. It is noted, however, that the ion saturation current is also proportional to $T_e^{1/2}$ and thus will only give a true representation of the density only if the temperature is constant. However, temperature measurements indicate that the longitudinal and transverse temperature gradients are only about 30%. This indicates that the profiles shown differ from the true density distribution by 15% at most.

Figure 36 shows the axial density profile both before and after absorption at r = 1 cm. Microwave interferometer measurements indicate that the average density changes very little at the time of absorption but Figure 36 clearly shows the density after absorption higher than before absorption. The reason for this is twofold. First, temperature measurements show that T_e increases by about 30% after absorption which accounts for a 15% increase in the ion saturation current and second, as will be shown, the radial density profile undergoes several rapid changes. Thus we cannot conclude from Figure 36 that the density after absorption is greater for all z, but we can get a reasonable picture of how the density is distributed along the axis of the mirror machine.

Figure 37 shows the radial density profile for several different times in the evolution of the plasma. Curves A and B show the distribution shortly after plasma formation to be peaked on axis and falling off toward the waveguide wall. C and D taken at progressively later times show that the density is redistributing itself to configurations with maxima off the axis. Curve E shows the density distribution just after absorption.

Figure 38 shows the density profiles for several axial positions just before absorption of the left wave. The inner maximum of curve E in Figure 37 (z=0) has moved onto the axis at z = -7.6 cm and has completely vanished by z = -15.3 cm. It is also seen that at positions further downstream from the center of the machine, the maxima move closer to the axis.

FIGURE CAPTIONS

Fig. 36. The axial density distribution (arbitrary units) is shown for both before and after absorption of the left wave along with the magnetic field profile. The microwave power is incident from the left at $z = +22$ cm (location of the resonant iris) and the left wave is cutoff at about $z = +11$ cm.

Fig. 37. Time evolution of the radial density profile. The ion saturation current in arbitrary units is plotted versus the normalized radial position. Points A - E refer to progressive points in time.

Fig. 38. Radial density profile for various axial positions just before absorption of the left wave.

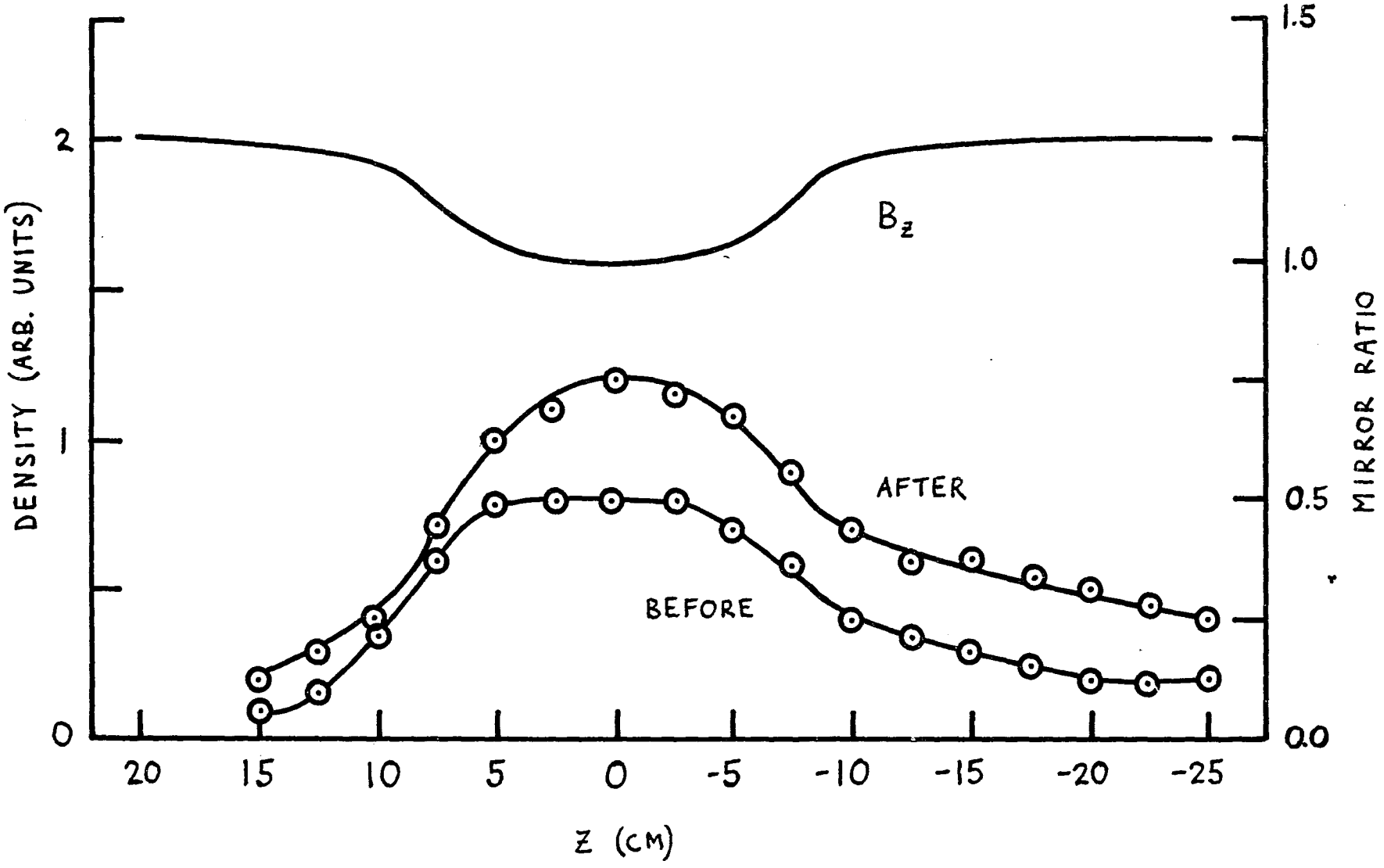
DENSITY (ARB. UNITS)
2
1
0
B_z
AFTER
BEFORE
20
15
10
5
0
-5
-10
-15
-20
-25
Z (CM)
1.5
1.0
0.5
0.0
MIRROR RATIO

FIGURE 36

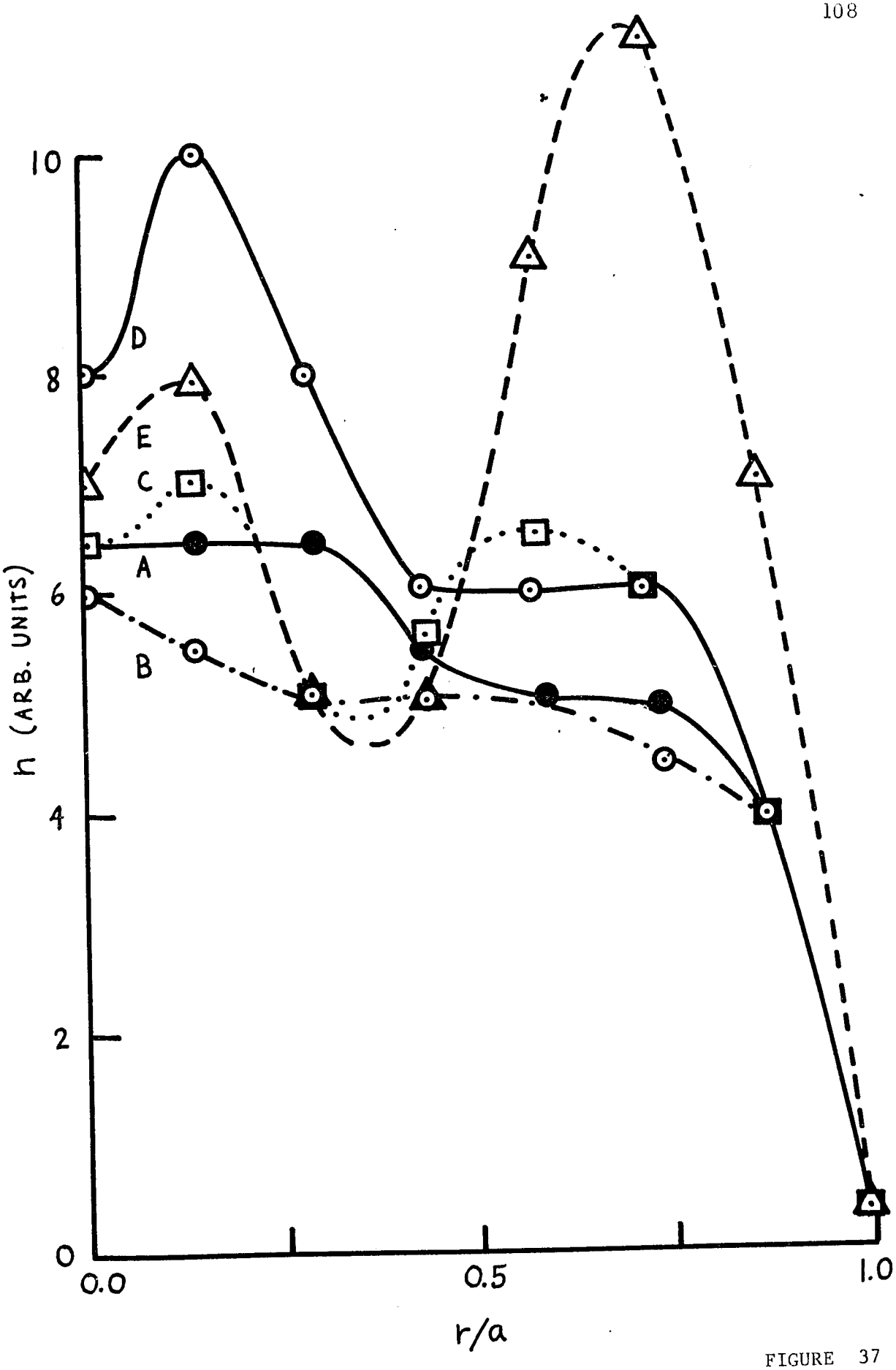

FIGURE 37

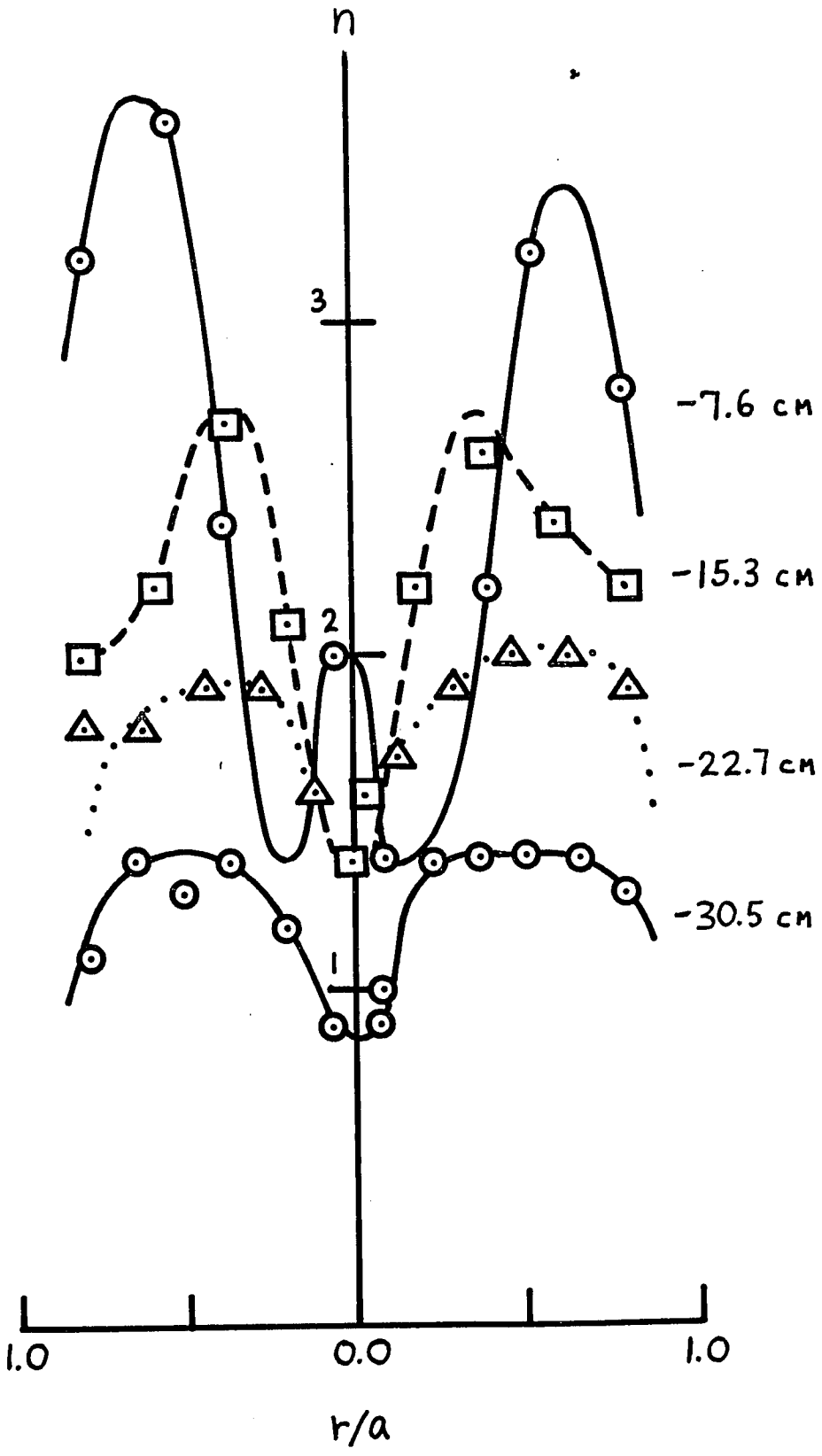

FIGURE 38

3 - RF PROFILES

Figure 39 is an axial profile at r = 0 taken with the dipole probe. The RF power (crystal response) is plotted for both horizontal (H) and vertical (V) orientations of the probe. The upper curves were taken before absorption and the lower set after absorption. The wave enters the cylindrical waveguide at z = +22 cm and should be intially linearly polarized in the vertical direction (not shown). The response before absorption clearly shows that Faraday rotation of the wave is taking place up to about z = +13 cm. Beyond z = +4 cm the horizontal and vertical signals are identical indicating that the wave is now circularly polarized (either left or right handed). We assume that it is the left component which is propagating because of the strong cyclotron damping of right wave predicted by theory. (Evidence will be presented later to verify that it is indeed the left wave which is propagating.) This left wave is transmitted through the plasma volume and then sets up a standing wave pattern in an essentially vacuum guide on the downstream side of the plasma for $z \gtrsim -15$ cm. Only the first peak in the standing wave pattern is shown.

The lower set of curves (after absorption) again show Faraday rotation but now both the left and right components are absorbed by z = +4 cm. Reflected power measurements (see Figure 40) show that there is essentially no reflected power after absorption, thus we conclude that both the left and right hand waves are being absorbed. Most of the $\sim$ 4% reflected power after absorption in Figure 40 is attributed

FIGURE CAPTIONS

Fig. 39. Axial standing wave pattern for vertical (V) and horizontal (H) orientations of the RF dipole probe. The upper curves are before absorption and the lower curves after.

Fig. 40. Percent reflected power as a function of neutral pressure is plotted both before and after the absorption of the left wave. The incident power is 365 watts. In the vacuum guide, the reflected power is 67%.

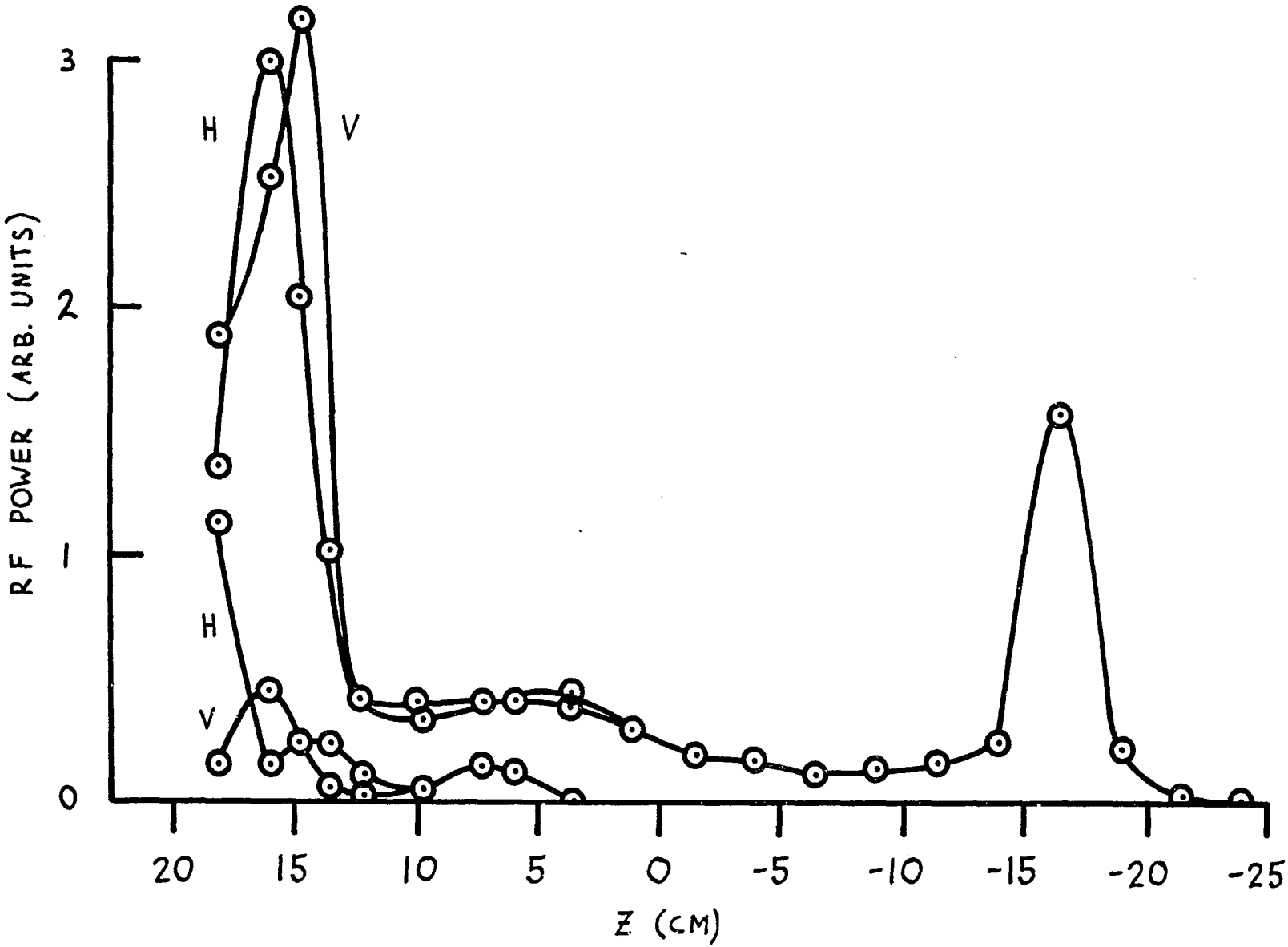

FIGURE 39

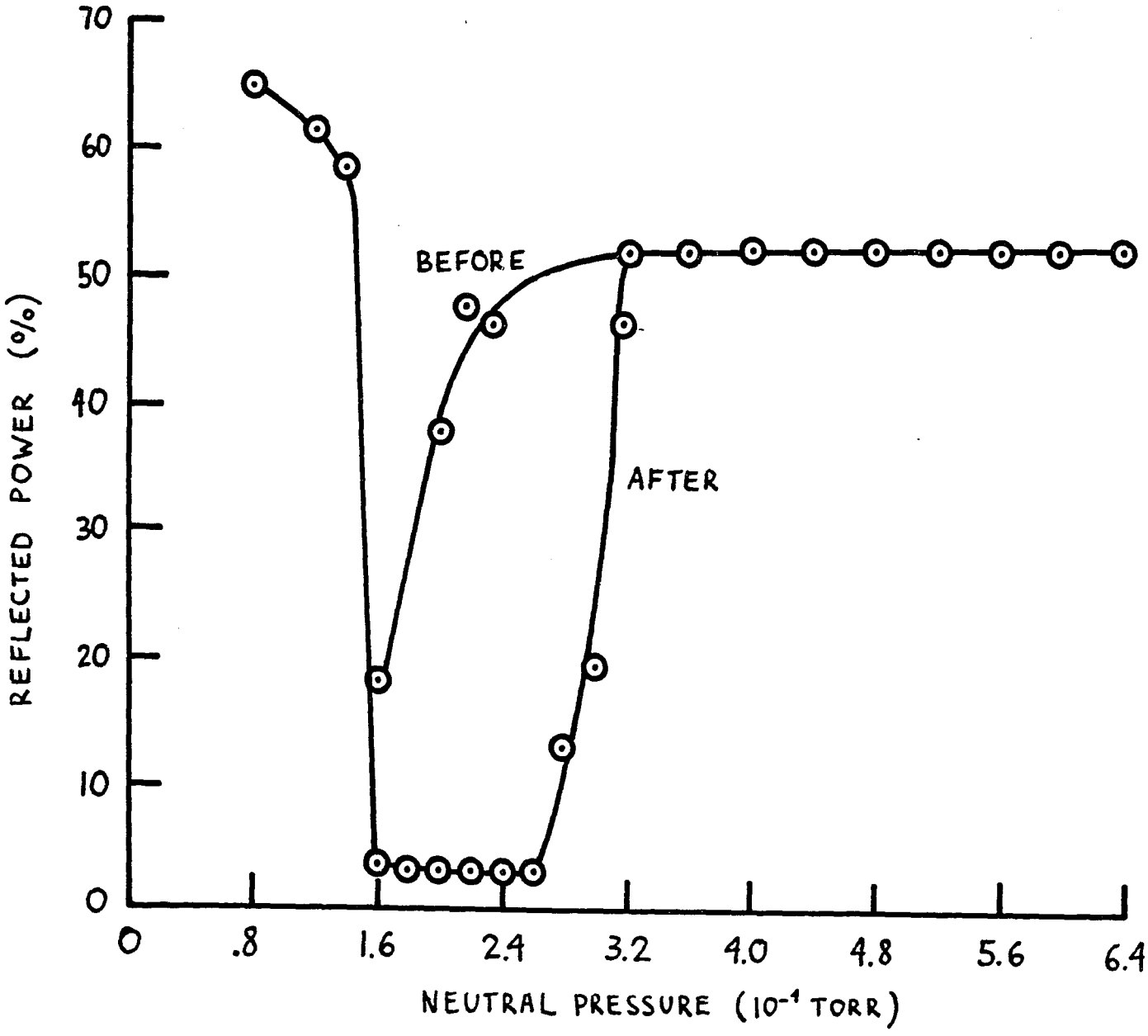
70
60
50
40
30
20
10
0
REFLECTED POWER (%)
BEFORE
AFTER
0
.8
1.6
2.4
3.2
4.0
4.8
5.6
6.4
NEUTRAL PRESSURE (10^{-4} TORR)

FIGURE 40

to waveguide mismatch.

To verify that the left wave was being transmitted before absorption, a spiral antenna was used. This antenna consists of a piece of wire wound on a plexiglass cone in a sense so that it responds predominantly to a left hand polarized wave. When the static magnetic field is reversed, the role of the left and right waves is also reversed. The response of the probe with the field reversed was 10 db lower than its response to the left wave thus confirming this hypothesis.

Radial profiles of E_r and E_θ were taken at various axial positions with the dipole probe. Figures 41 and 42 show typical results. Curve A is taken just after plasma formation where the diamagnetic signal levels off. These profiles are in excellent agreement with the theoretical profiles (see Figure 10). Curve B was taken at the average of the ion acoustic modulations of transmitted left wave signal (before absorption). As with the density profiles, the electric field distributions are also "annular" in configuration.

Figures 43, 44 , 45 show the field profiles for the downstream positions of z = -7.6 cm. -20.0 cm and -25.4 cm. Again it is observed that the maxima are farthest from the axis close to the center of the machine, but move closer together for positions further downstream (to regions of lower density) until the profiles again appear as expected by z = -25.4 cm. This redistribution of the fields accounts for the large amplitude peaks in F igure 39 . The regions of maximum density as well as maximum electric field appear to be "football shaped."

The wave magnetic field profiles just before absorption are shown in Figures 46 and 47 . Here again H_r and H_θ exhibit annular configuration rather than their expected peaked on axis distribution.

FIGURE CAPTIONS

Fig. 41. E_θ radial profile (arbitrary units) at z = -15.3 cm. Curve A is the dipole probe response just after plasma formation and curve B is the average of the ion acoustic modulations of the left wave before absorption.

Fig. 42. E_r radial profile (arbitrary units) at z = -15.3 cm. Curve A is the dipole probe response just after plasma formation and curve B is the average of the ion acoustic modulations of the left wave before absorption.

Fig. 43. Electric field radial profiles at a time just before absorption at z = -7.6 cm.

Fig. 44. Electric field radial profiles at a time just before absorption at z = -20.0 cm.

Fig. 45. Electric field radial profiles at a time just before absorption at z = -25.4 cm.

Fig. 46. H_r radial profile at a time before absorption at z = -15.3 cm.

Fig. 47. H_θ radial profile at a time before absorption at z = -15.3 cm.

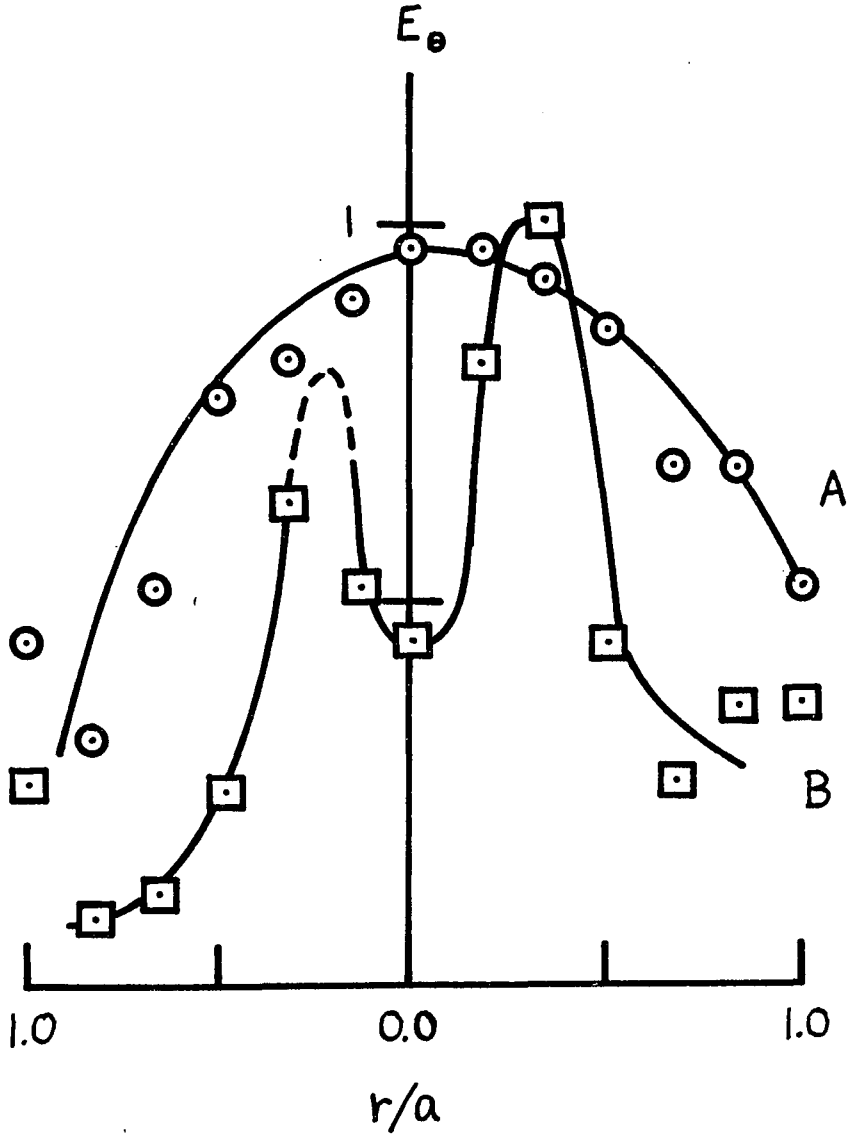

FIGURE 41

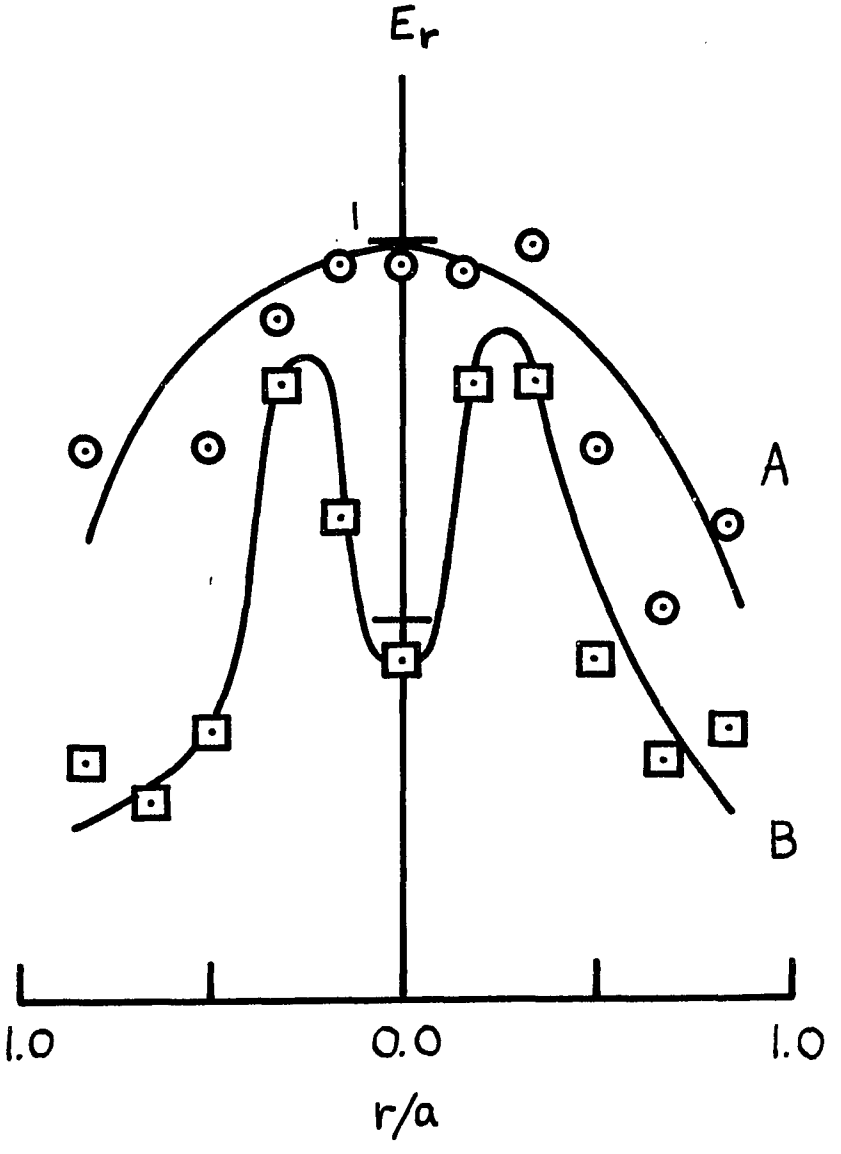

FIGURE 42

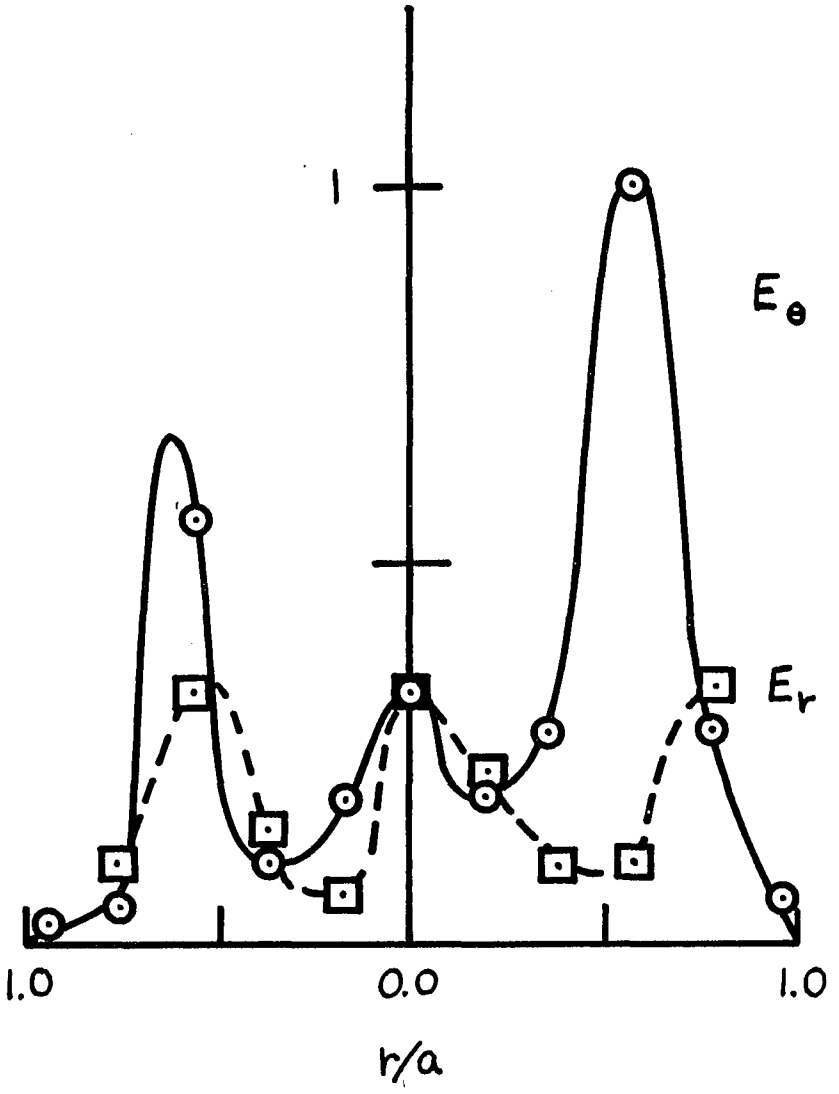

FIGURE 43

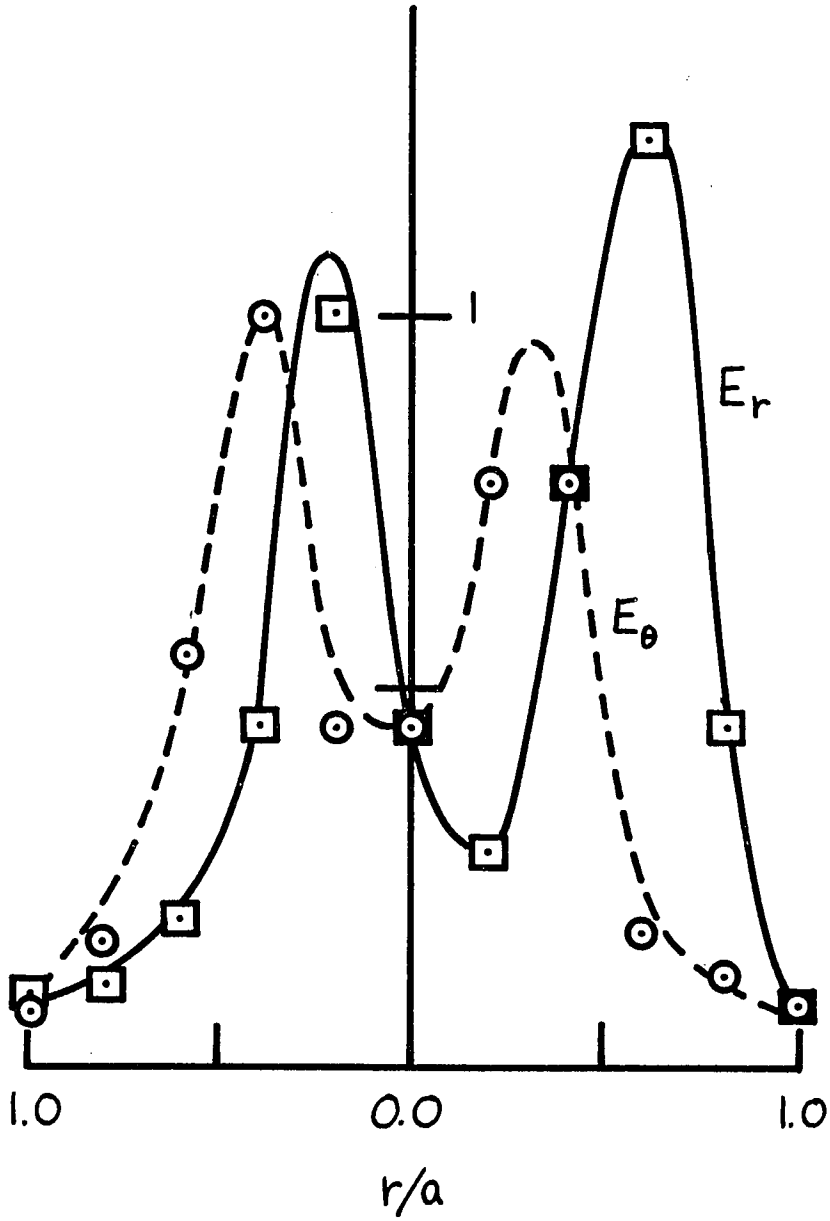

FIGURE 44

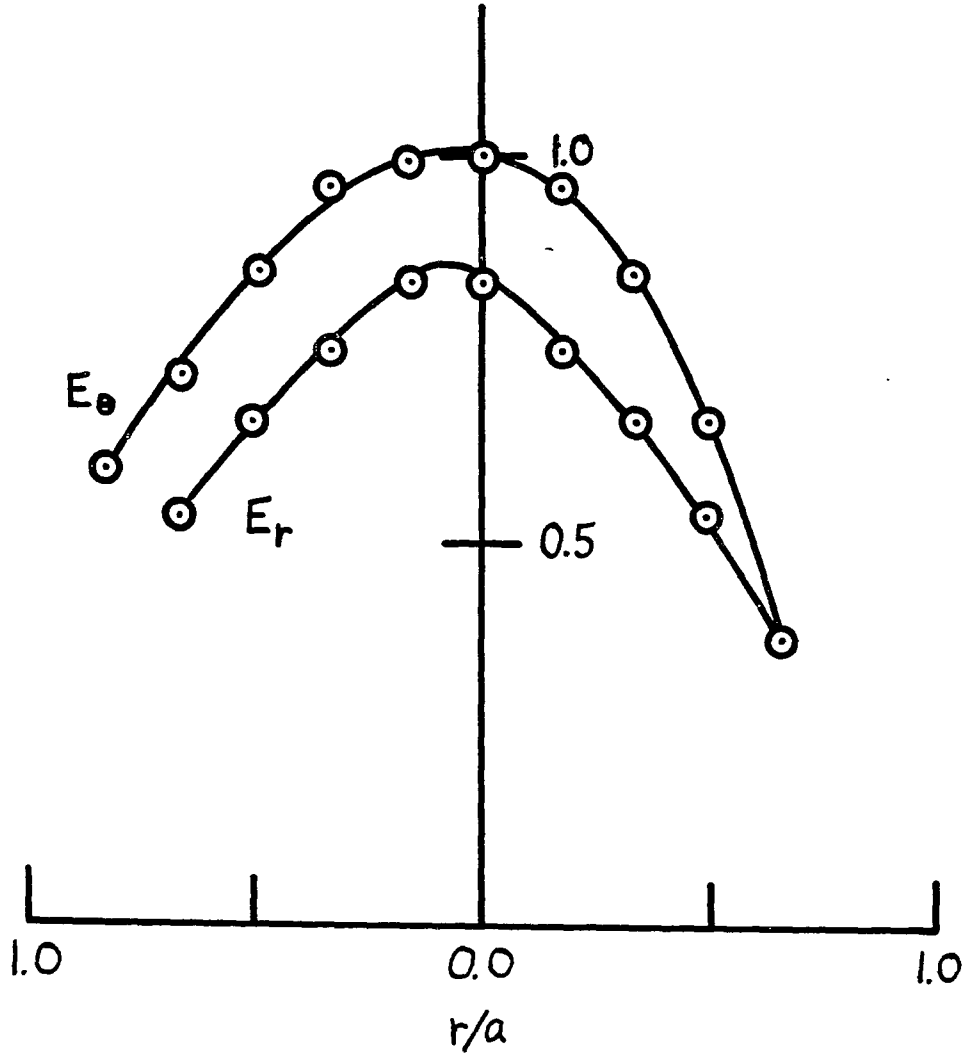

FIGURE 45

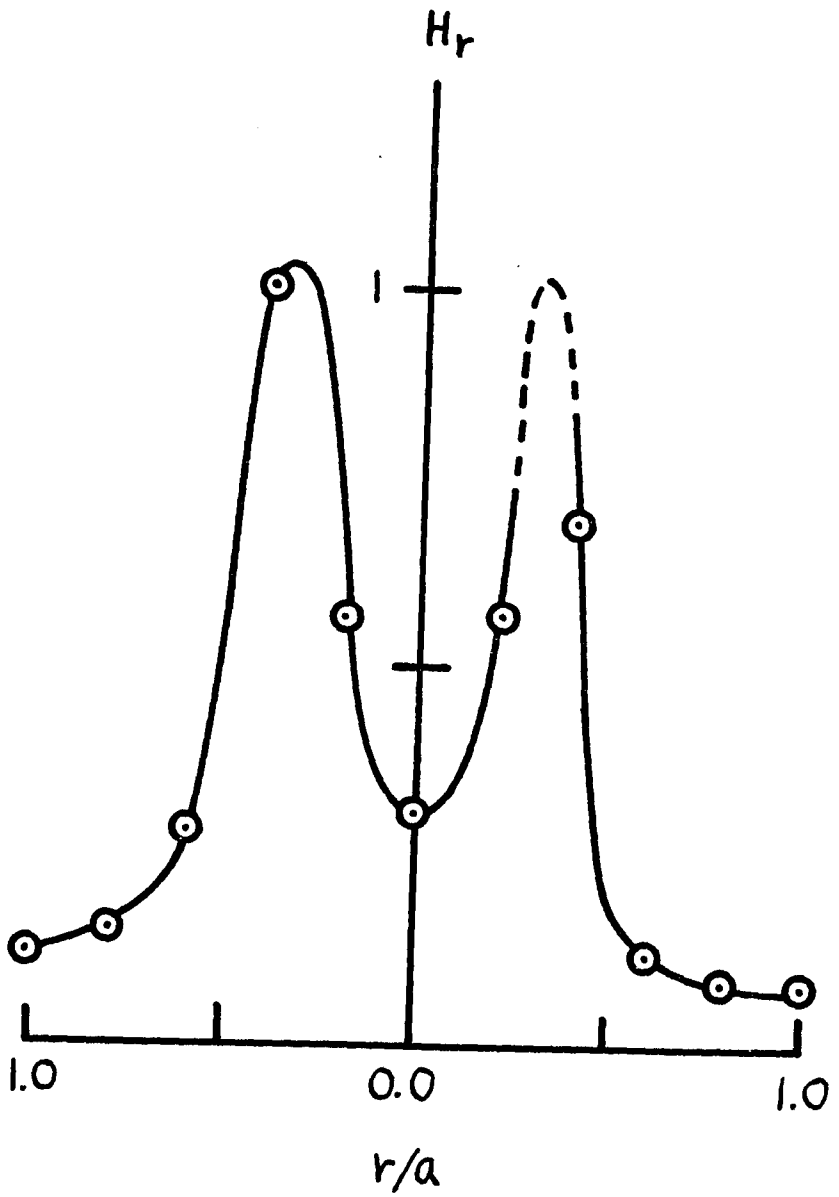

FIGURE 46

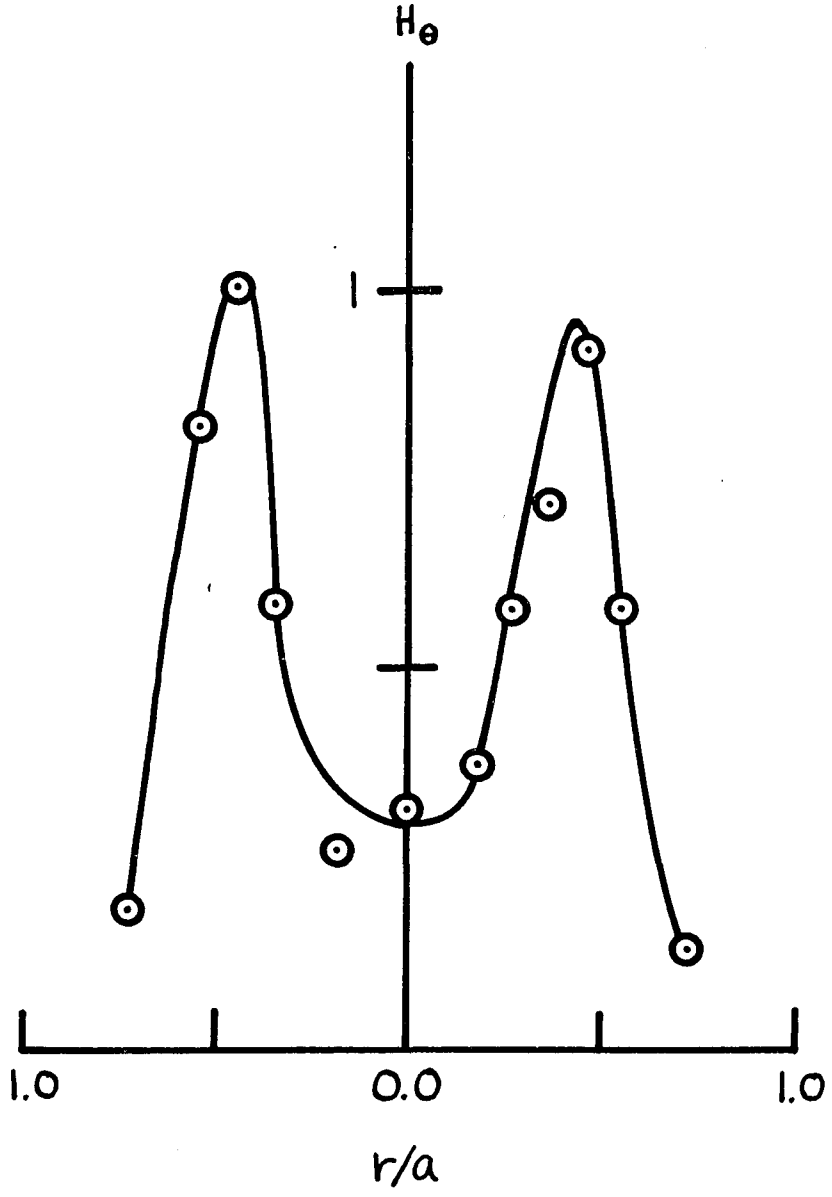

FIGURE 47

4 - ELECTROSTATIC PROFILES

As was previously discussed, the left hand wave is first transmitted then anomalously absorbed. During absorption the total transmitted power is less than .01%, the electron temperature increases 20-50% while the average density remains essentially unchanged. In addition to making RF power measurements with a crystal detector (which has a broad band response), measurements were also made with a microwave receiver (see apparatus) at all frequencies within the range of 0.9 - 4.1 GHz. Figures 48 and 49 show the power frequency spectrum taken with the receiver. Similar measurements were made in the vacuum guide in order to insure that the observed signals were plasma responses and not just pick up from the magnetron itself. Any responses in the 2 - 3.7 GHz region were found to be from the magnetron.

When the responses at any particular frequency are examined, they are typically found to look like Figures 50 and 51 . It is found that there is no response before absorption. Measurements at all frequencies clearly show the RF signals to build only immediately after absorption. This indicates that there are many modes which are excited in the plasma at the time of absorption.

In order to determine the propagation constants for these various modes, axial standing wave patterns of the wave magnetic field were taken at frequencies corresponding to the center of the peaks in Figures 48 and 49 . Typical results for the low frequency branch are shown in Figures 52 , 53 , 54 and 55 . Two features can easily be discerned

FIGURE CAPTIONS

Fig. 48. Power frequency spectrum of excited responses. The RF loop probe response (arbitrary units) is plotted against the frequency to which the receiver is tuned.

Fig. 49. Same as Figure 48 except for a higher range of frequencies.

Fig. 50. RF receiver response of the loop probe signal at f = 1685 MHz. Probe located z = -12.7 cm, r = 0. Vertical gain = .2 v/cm, time scale = .2 ms/cm.

Fig. 51. Same as Figure 50 except f = 3980 MHz and z = -8.9 cm.

Fig. 52. Axial standing wave pattern at f = 1480 MHz. The RF receiver response (arbitrary units) of the loop probe is plotted as a function of axial position z.

Fig. 53. Same as Figure 52 but a f = 1578 MHz.

Fig. 54. Same as Figure 52 but at f = 1685 MHz.

Fig. 55. Same as Figure 52 but at f = 1780 MHz.

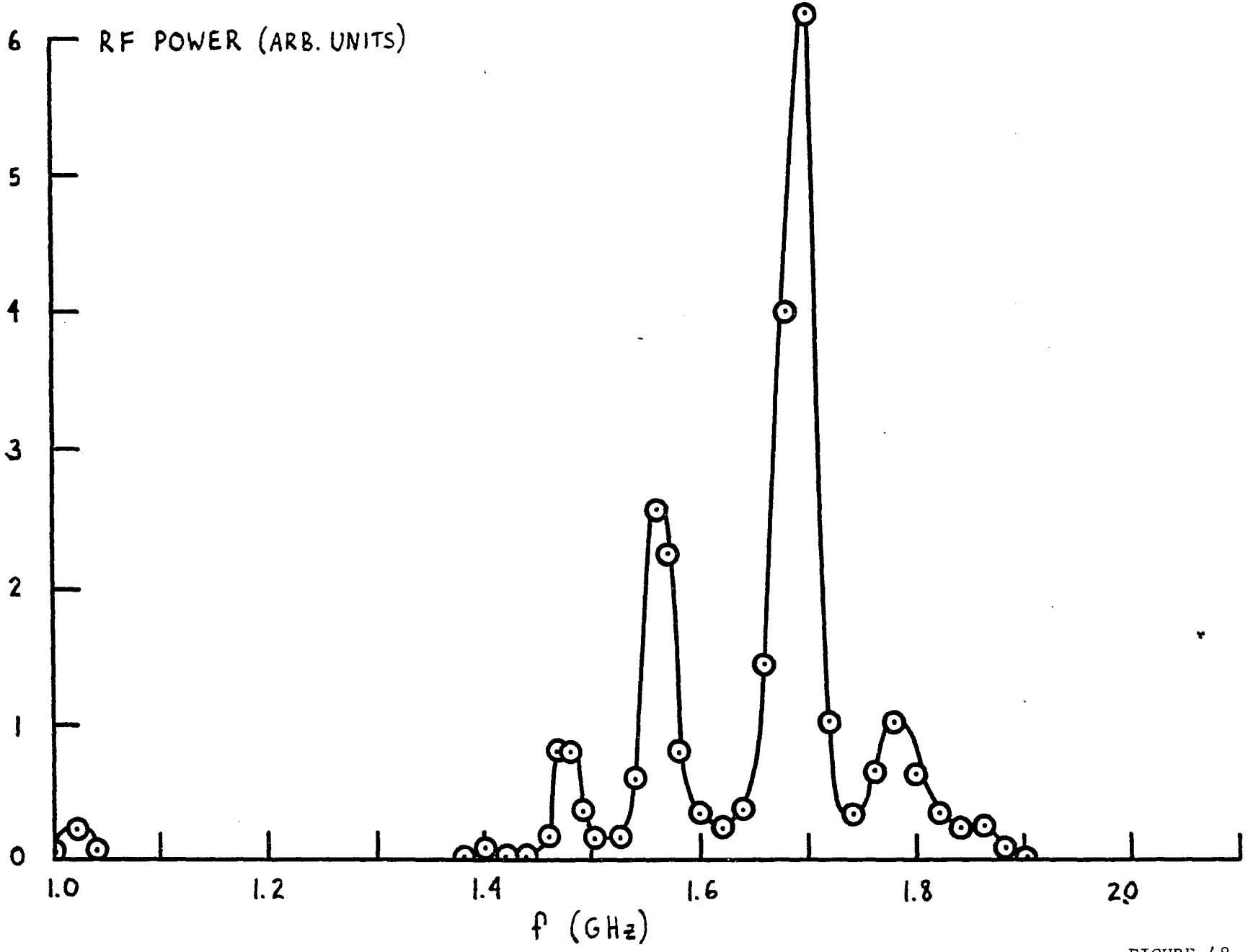

FIGURE 48

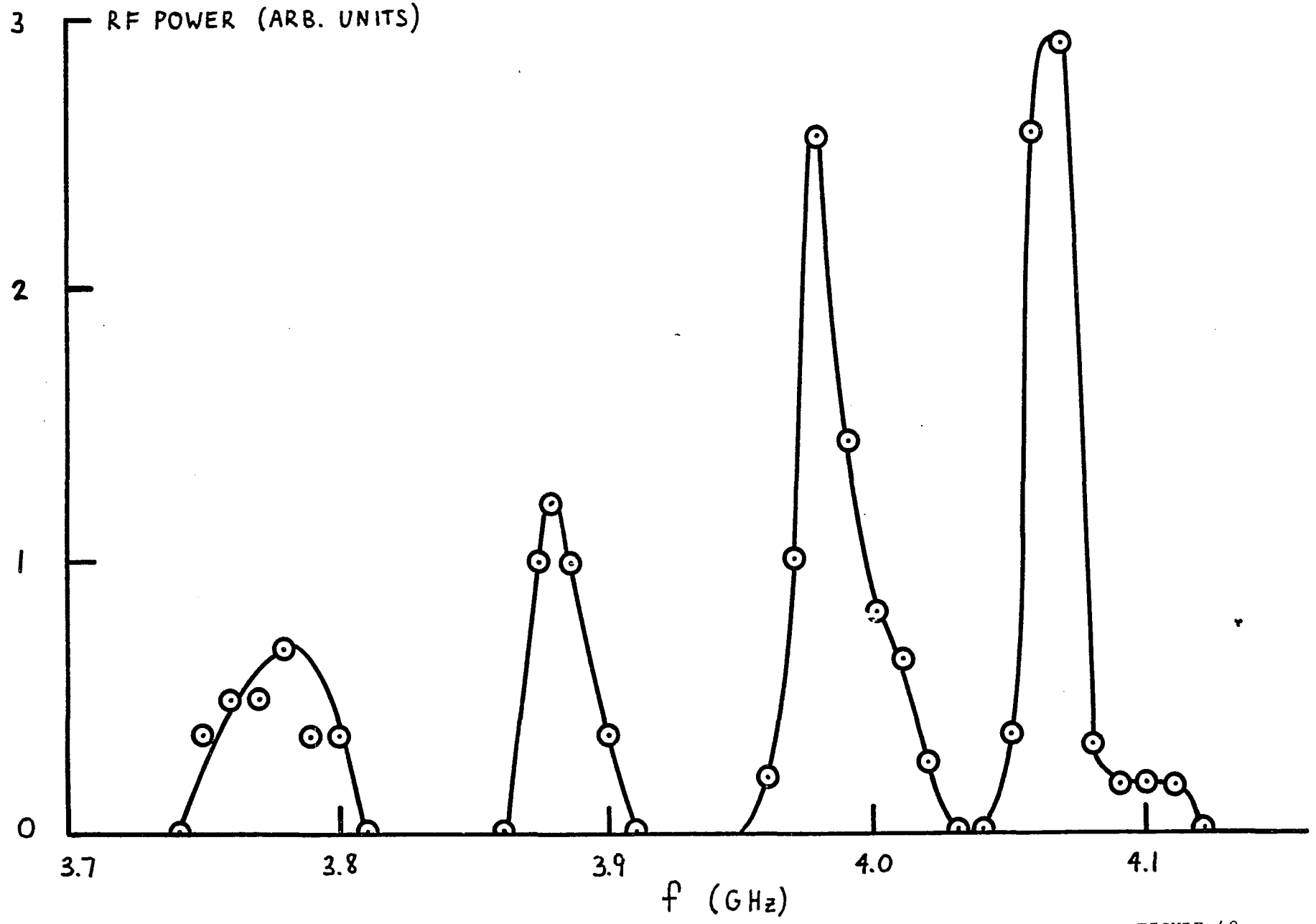

FIGURE 49

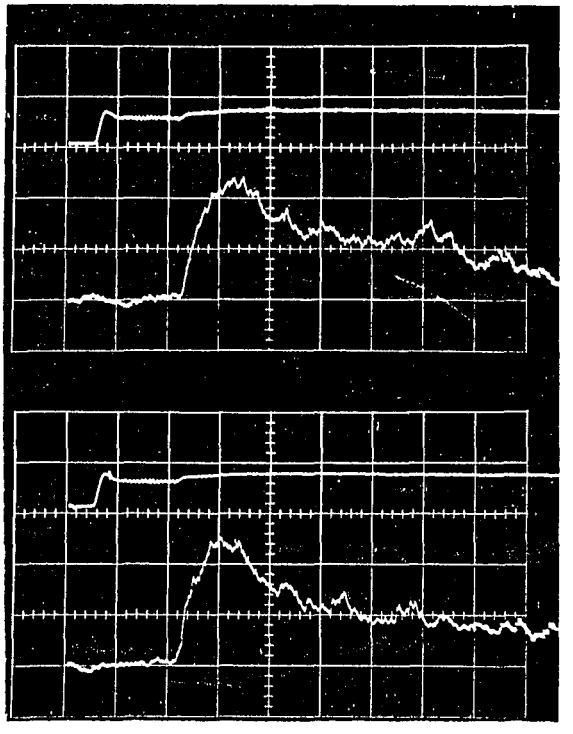

DIAMAGNETIC

RF POWER AT 1685 MHz

0.2 MS/CM

FIGURE 50

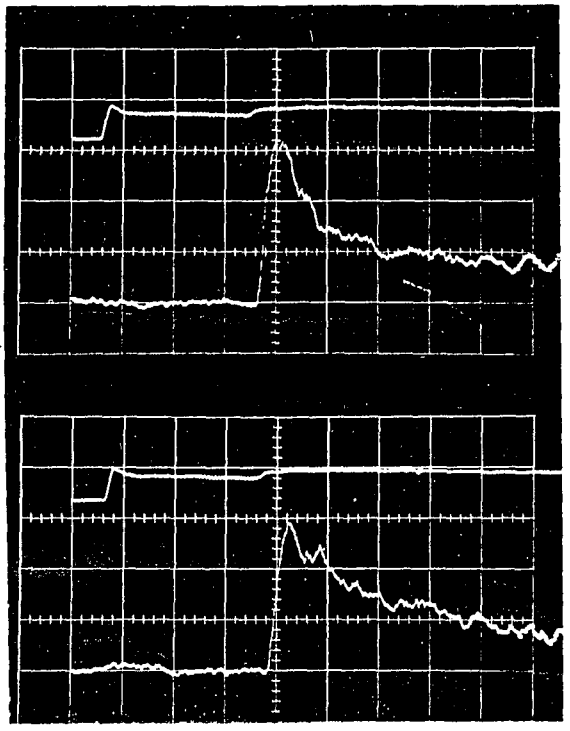

DIAMAGNETIC

RF AT 3980 MHz

0.2 MS/CM

FIGURE 51

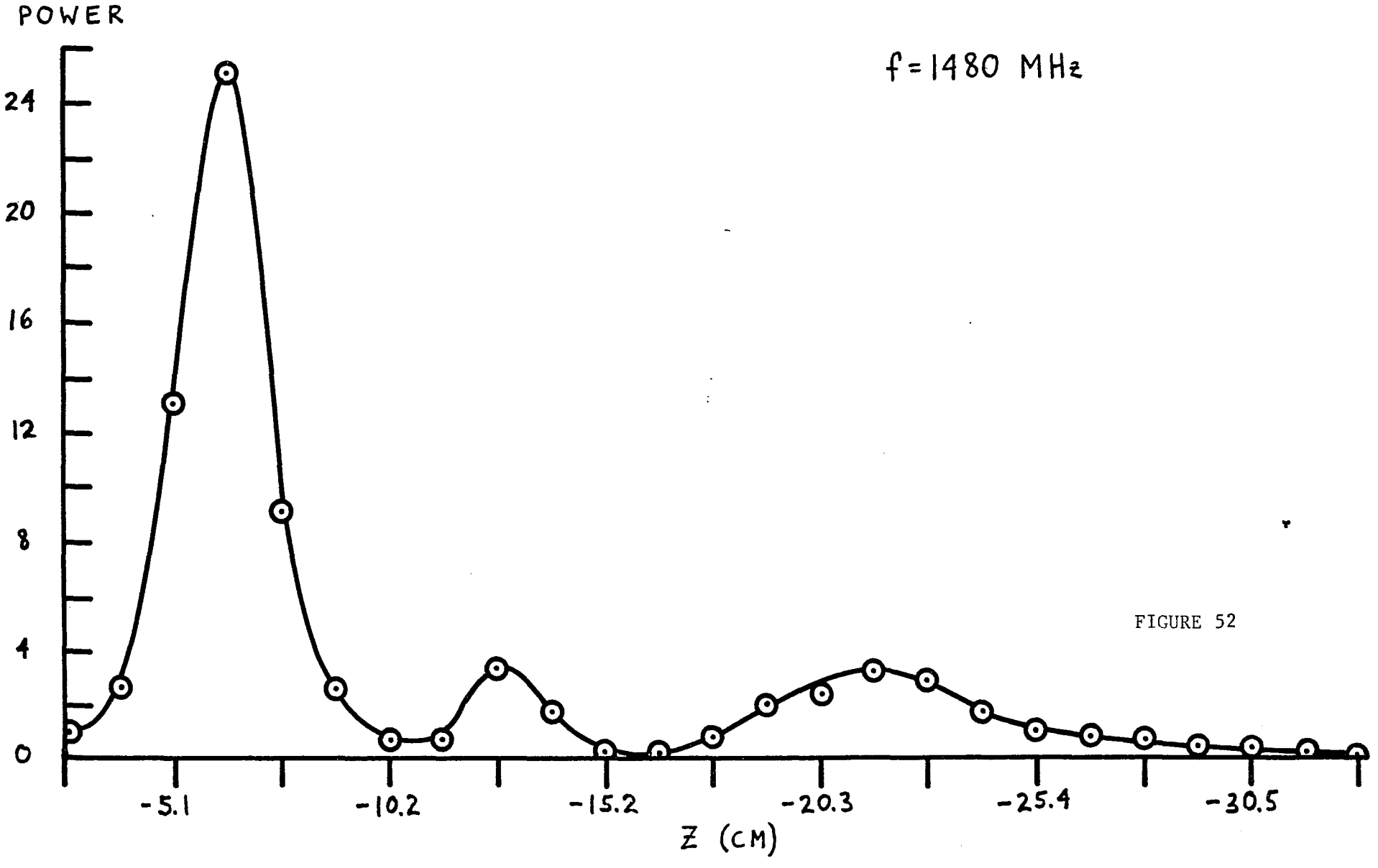

FIGURE 52

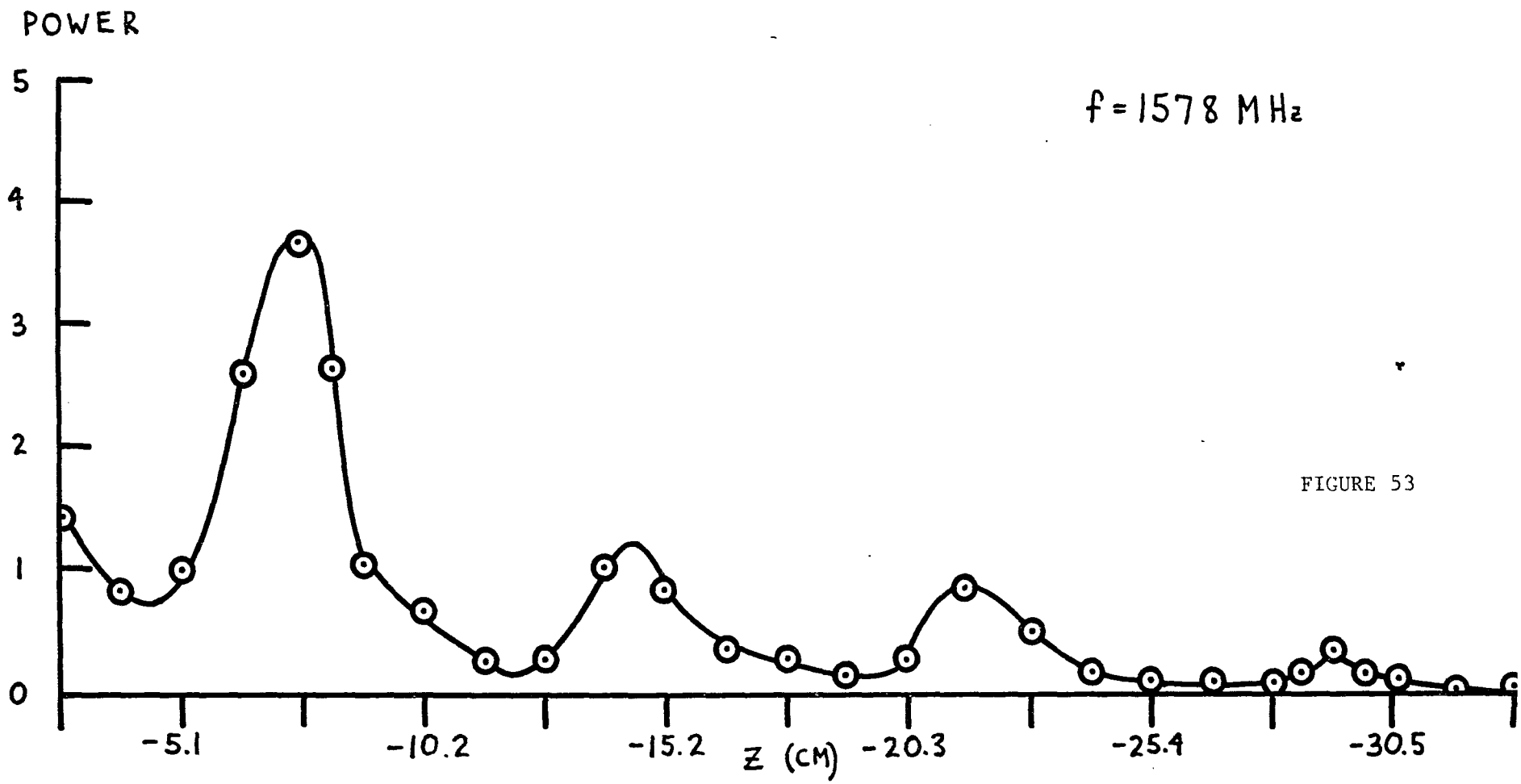

FIGURE 53

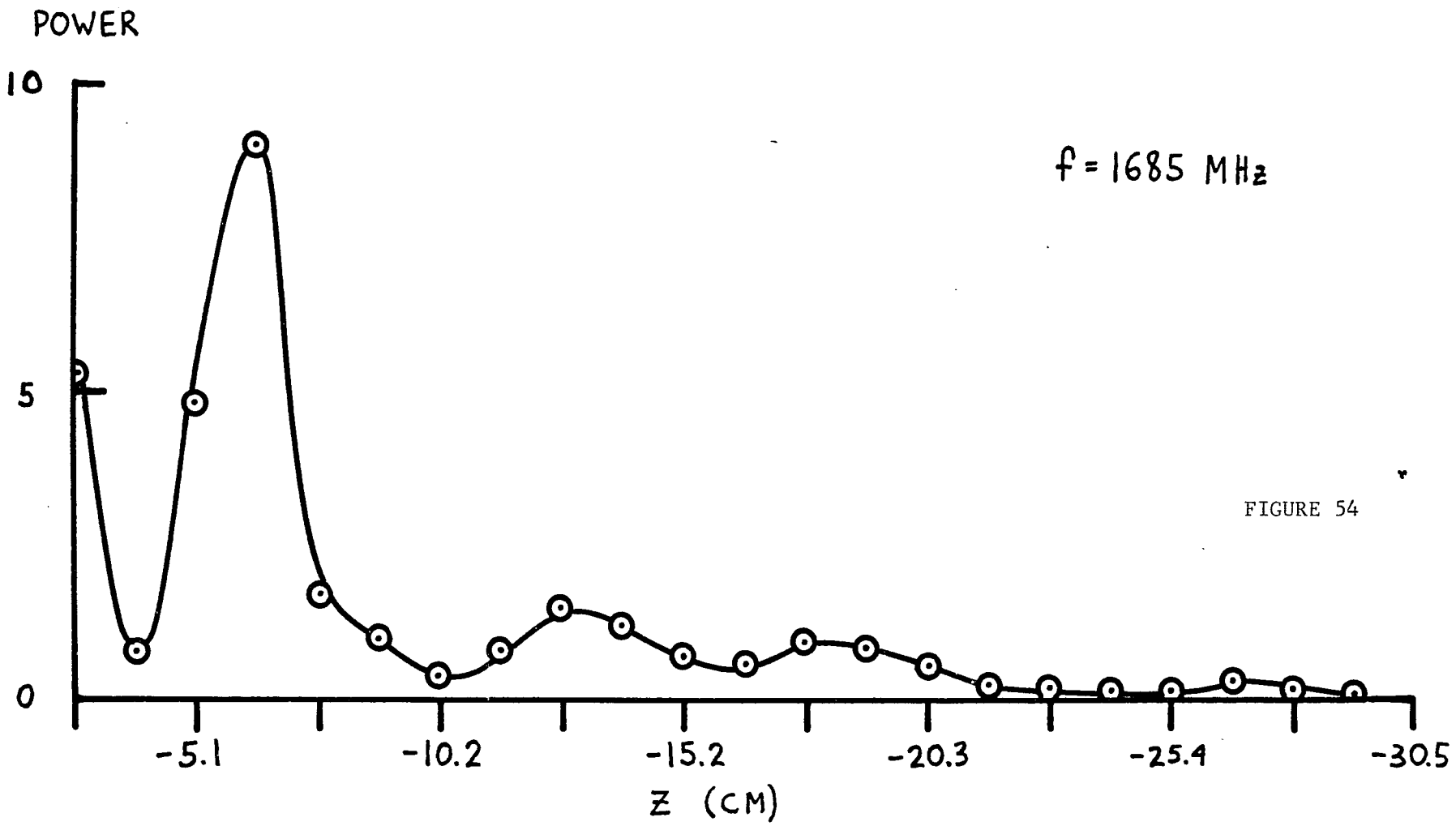

FIGURE 54

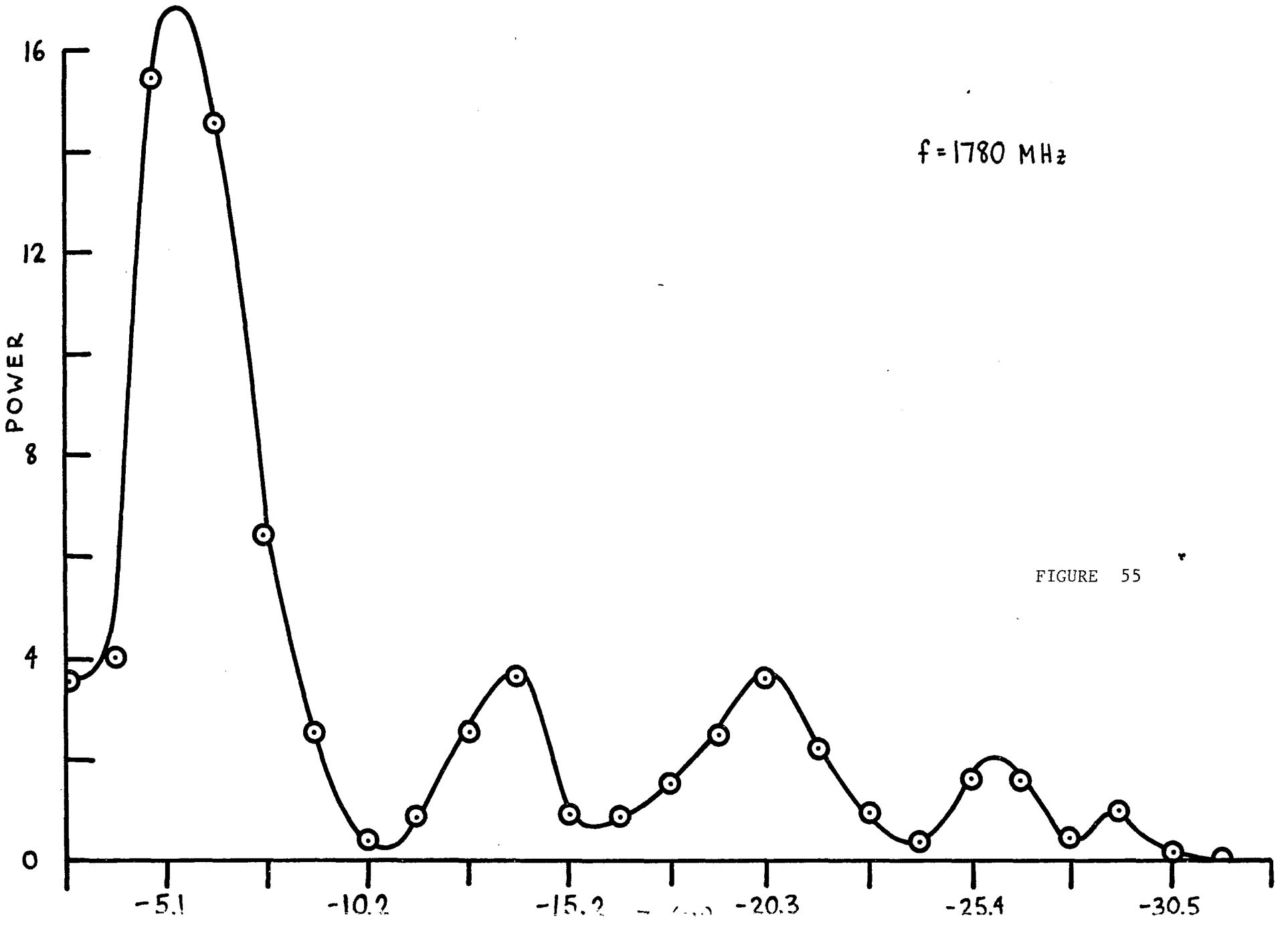

FIGURE 55

here: 1.- The wavenumber increases with frequency and 2.- k_z increases for lower densities (higher axial positions).

Figure 56 shows the average propagation constant for each measured frequency plotted as data points; the solid curves are the dispersion curves for the low frequency branch of bounded Gould - Trivelpiece modes[3](see Figure 11). It is noted that the slope of the data points is in reasonable agreement with the theory for no damping but the values of k_z are smaller than expected. This suggests that damping may be occuring, as collisional damping would tend to increase the wavelength from its undamped value. It is seen that a collision frequency of $\nu/\omega = .3$ gives excellent agreement.

Figure 57 is a plot of the propagation for a single frequency (1785 MHz) along with the theoretical dispersion curves, but now presented as a function of density rather than frequency. Again it is found that the measured wavenumber is in reasonable agreement with the undamped theory, but is less than predicted. For comparison, the damped electrostatic modes are also shown. It is seen that for low densities, a small collision frequency gives a better fit to the data, whereas at higher densities more damping appears evident; this is to be expected.

The standing wave pattern for f = 1578 MHz (Figure 53) also reveals an exponential envelope which is suggestive of damping. In Figure 58 the maxima and minima of the axial profile for this frequency are presented on a semi-log plot. The slope of these curves yields a damping decrement of about 9 cm (for power). This corresponds to

FIGURE CAPTIONS

Fig. 56. The average wavenumber at each measured frequency is plotted as data points; the curves are the computed dispersion characteristics for the low frequency branch of the m = 0 Gould-Trivelpiece modes. The curves were calculated for f_c = 2.7 GHz, n = 2.0 x 10^{11} cm^{-3} and a = 4.39 cm.

Fig. 57. The wavenumber at f = 1785 MHz is plotted versus density. These values were interpolated from the axial standing wave pattern (Figure 55) and the axial density profile (Figure 36). The curves are the dispersion characteristics of the real part of the wavenumber for the m=0 Gould-Trivelpiece modes. f = 1780 MHz, f_c = 2.7 GHz and a = 4.39 cm.

Fig. 58. The maxima and minima of axial profile for f = 1578 MHz (Figure 53) are plotted on a log scale versus axial position on a linear scale. The power damping decrement as determined from the slope is approximately 9 cm.

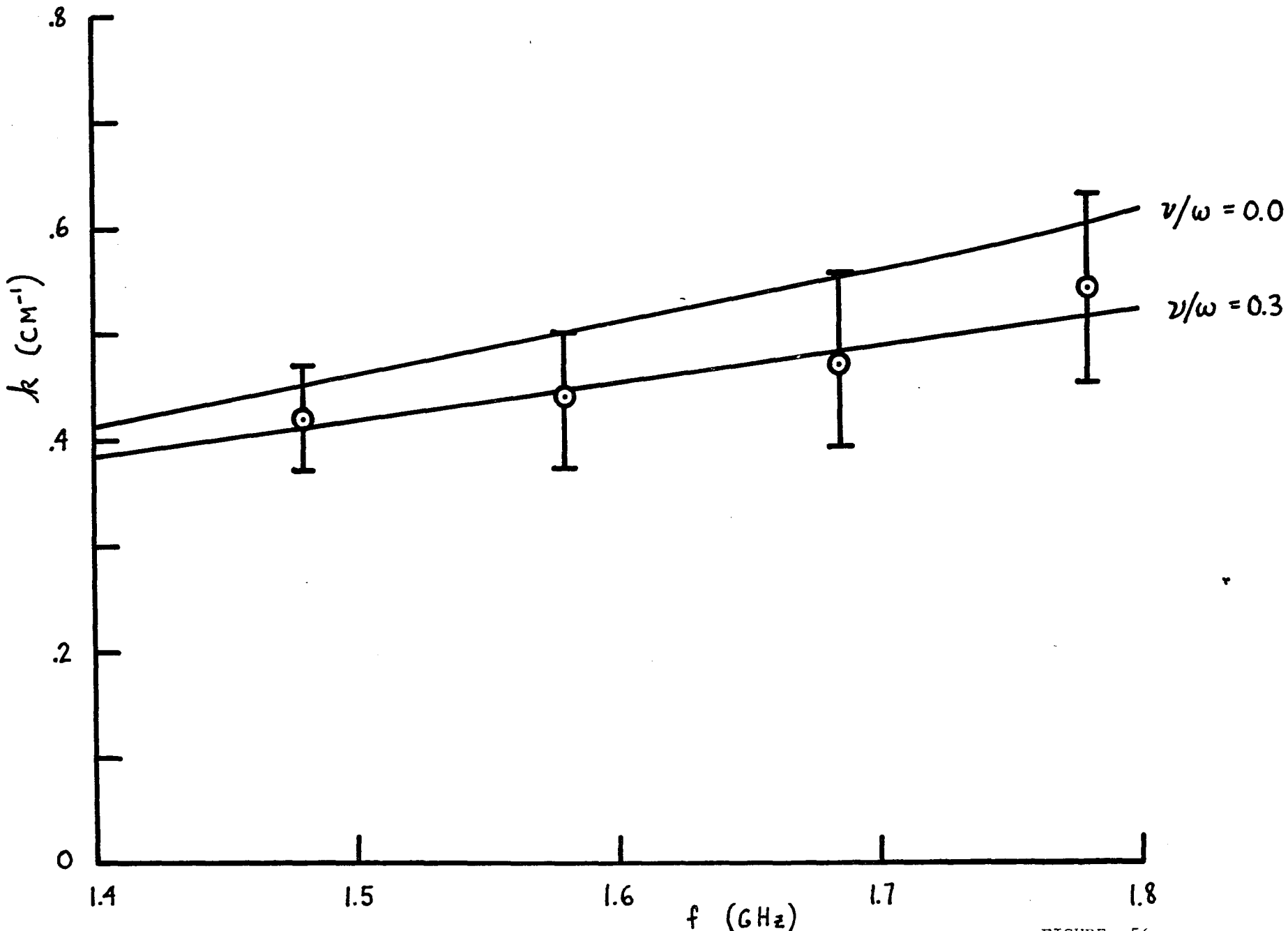

FIGURE 56

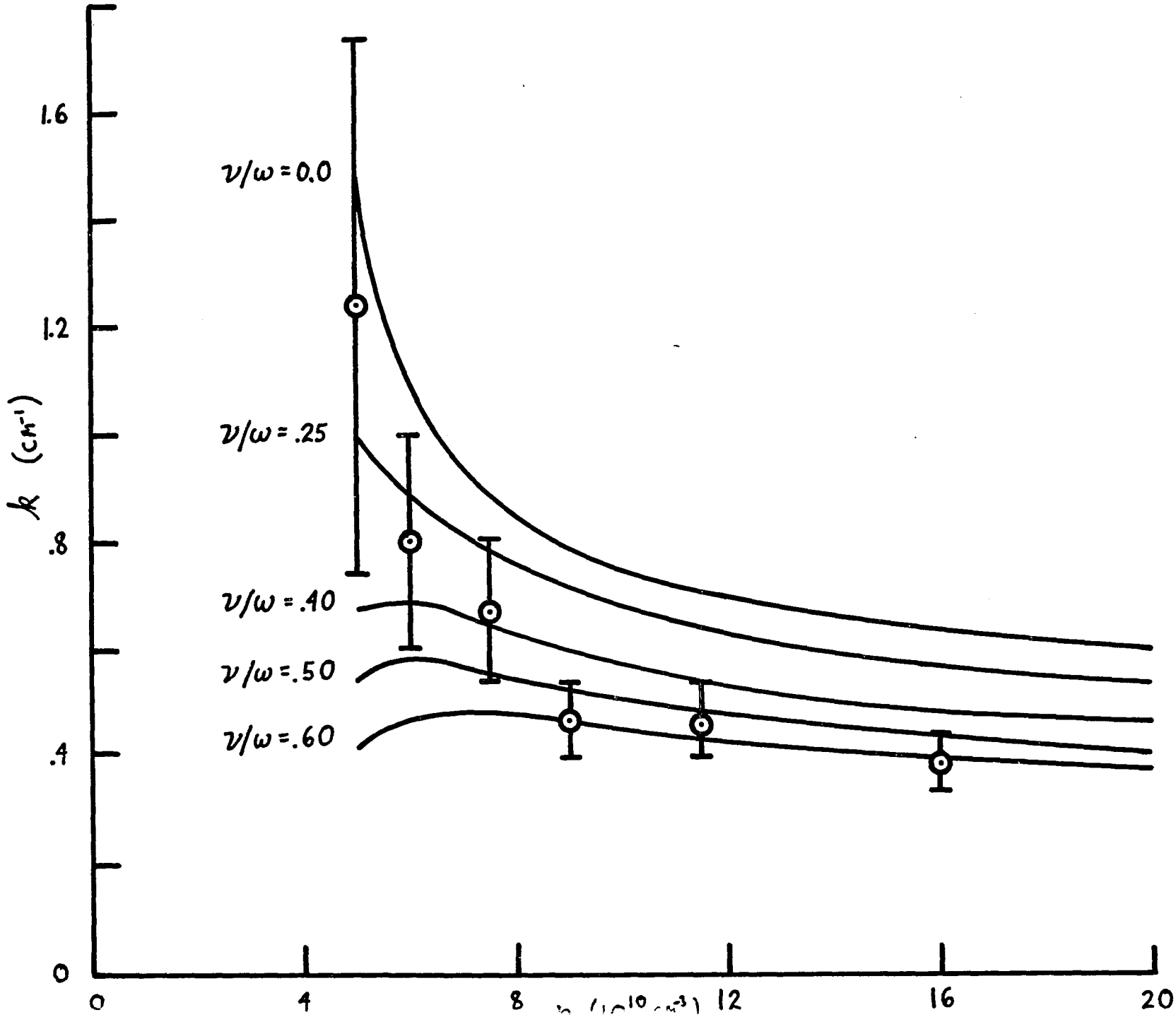

FIGURE 57

FIGURE 58

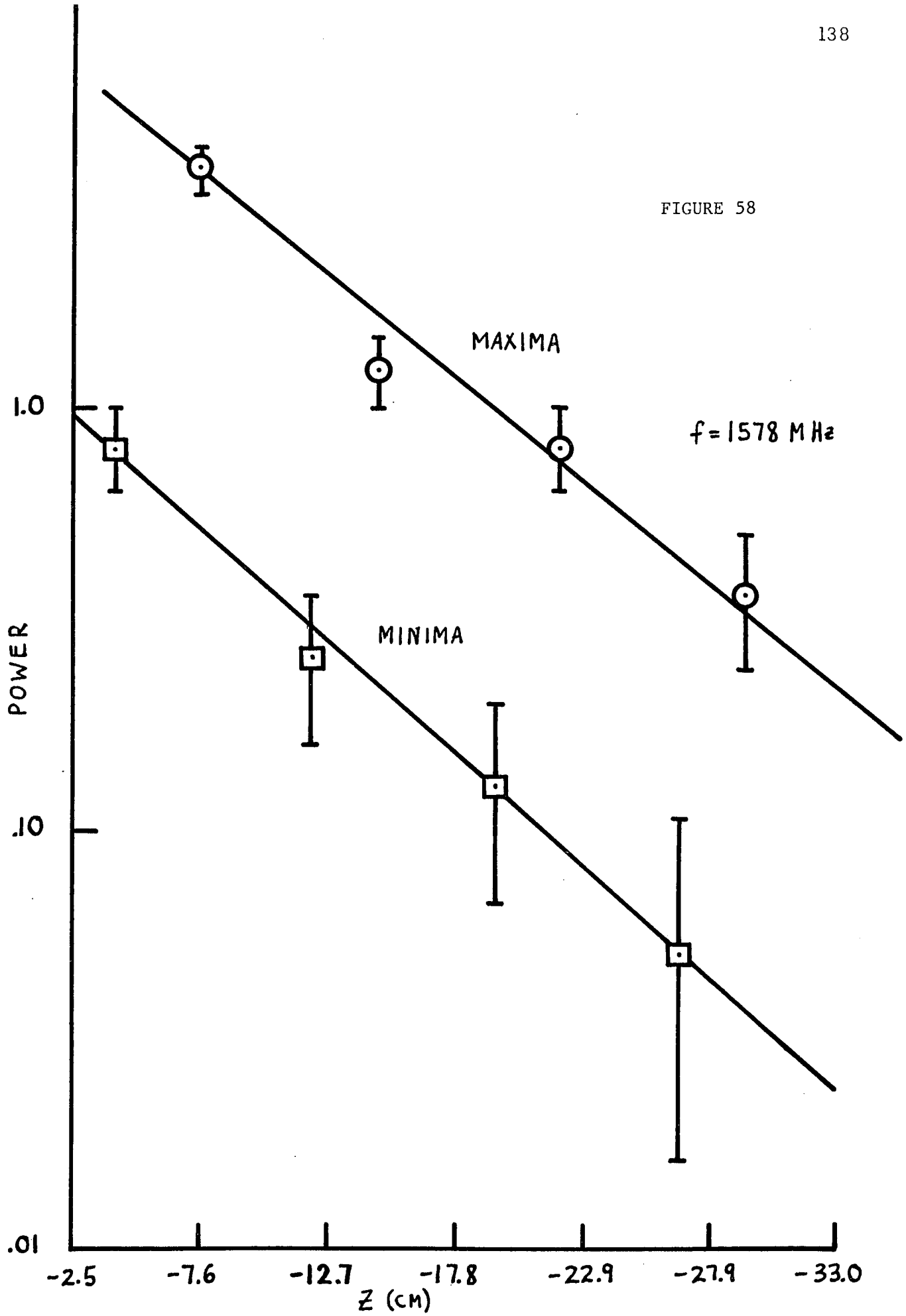
MAXIMA
MINIMA
f = 1578 MHz
POWER
1.0
.10
.01
-2.5
-7.6
-12.7
-17.8
-22.9
-27.9
-33.0
Z (CM)

a collision frequency of about $\nu/\omega = .1$ which is comparable to the value previously obtained. The standing wave patterns for the other frequencies also exhibit damping, but it is not as clearly defined as in the frequency discussed above. In general it is noted that the other axial patterns yield somewhat greater values of collision frequency.

In the low frequency branch only electrostatic modes can exist (the cutoff frequency for electromagnetic modes = 2.00 GHz) and we had clearly defined values for the propagation constants. However, for the high frequency branch, electromagnetic as well as electrostatic modes are present and this prevents us from obtaining the wavenumber from the standing wave patterns here (see Figures 59 , 60 , 61 and 62). To obtain these plots, many data (at the same and at different axial and radial positions) were taken. At certain axial positions the results were not readily reproducable. The problem here is that with more than one mode present, slight perturbation in the discharge would cause the probe to pick up first one mode, then another and possibly a combination of modes in the next measurement. Another problem is that for the high frequency branch, the wavenumber is strongly dependent upon the density (see Figure 12). Any local density fluctuations can cause large variations in k_z thus causing erratic results. Figures 59 - 62 represent the average or more consistent of the values obtained, however, it was not deemed plausible to ascertain values for the wavenumber from this data.

To present further evidence that these excited modes are the electro-

FIGURE CAPTIONS

Fig. 59. Axial standing wave pattern of loop probe (arbitrary units) at f = 3780 MHz.

Fig. 60. Same as Figure 59 but at f = 3880 MHz.

Fig. 61. Same as Figure 59 but at f = 3980 MHz.

Fig. 62. Same as Figure 59 but at f = 4070 MHz.

FIGURE 59

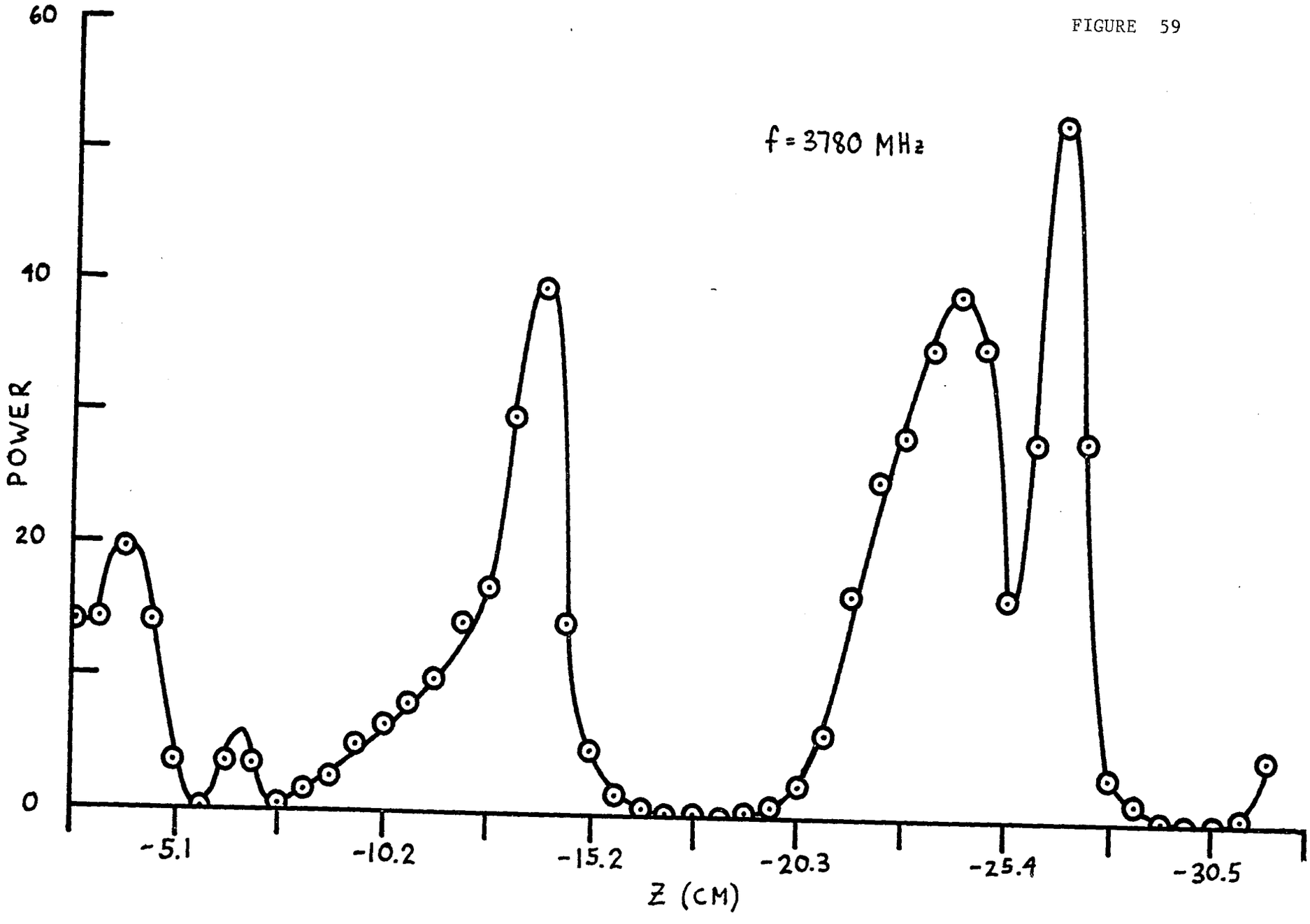

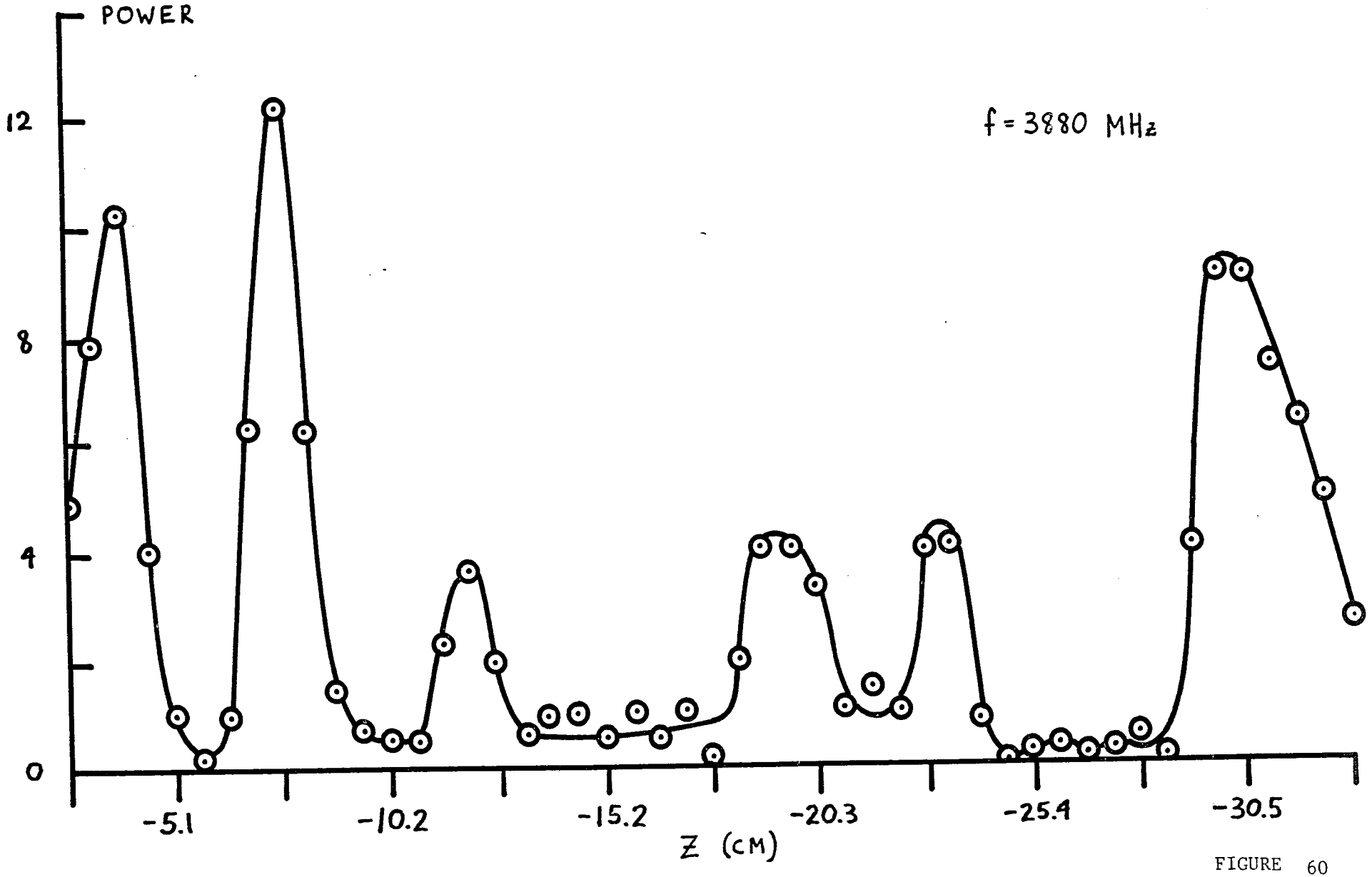

FIGURE 60

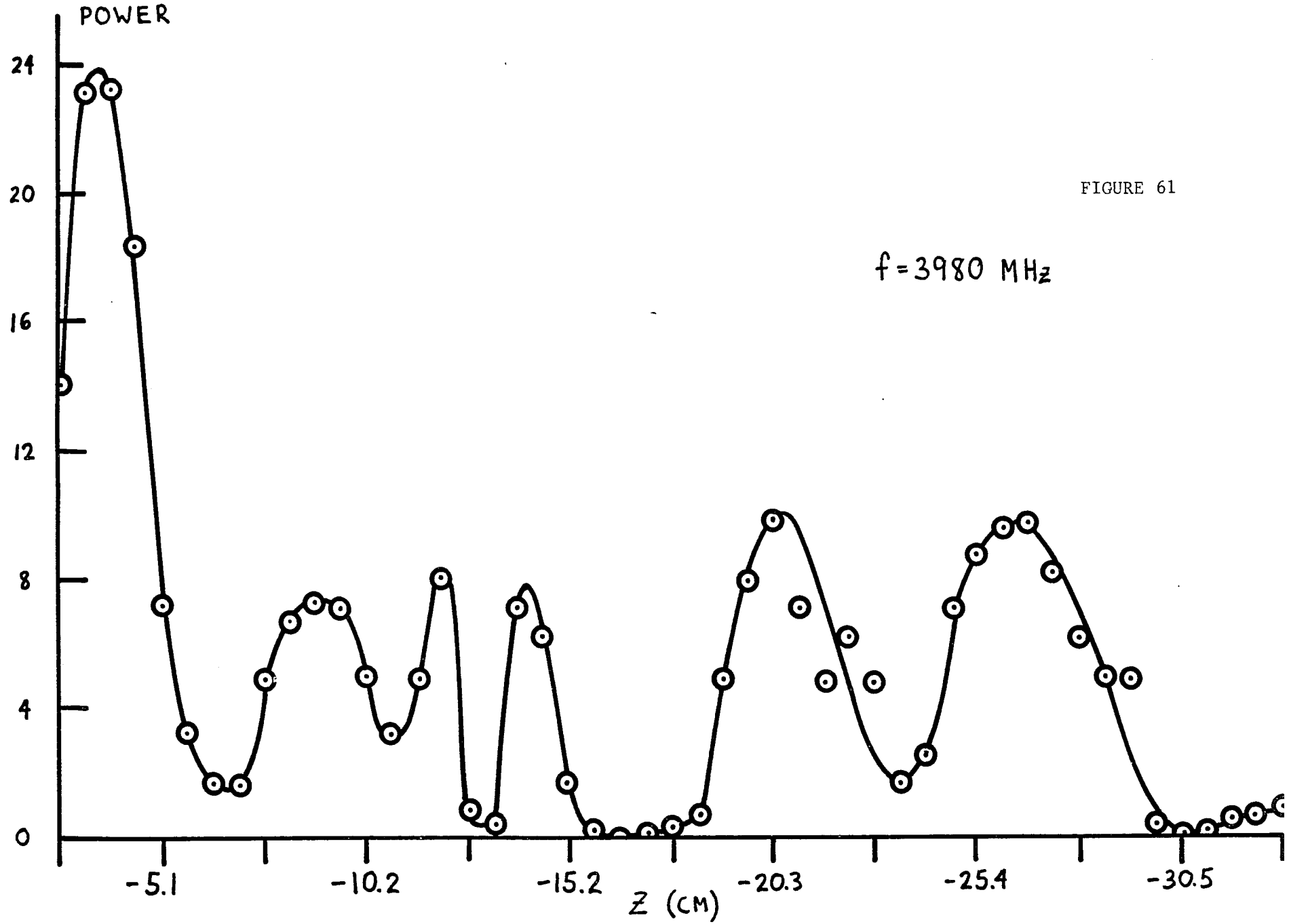

FIGURE 61

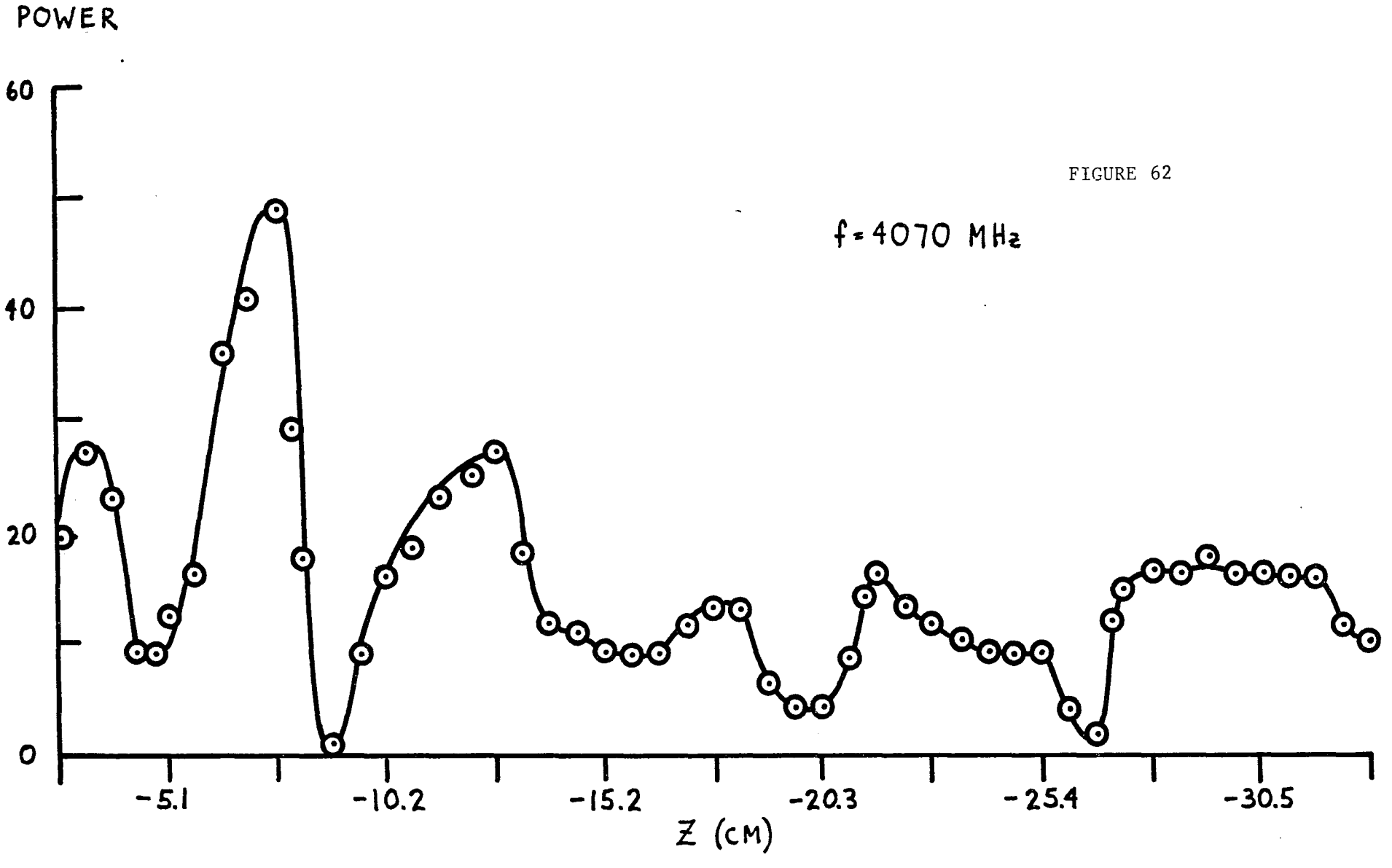

FIGURE 62

f = 4070 MHz

static modes described by Gould and Trivelpiece[3] and in addition to measure the azimuthal mode number m, the radial wave magnetic field profiles were compared to theory. On Figures 63, 64, 65, and 66 the radial profile of H_r is presented along with the theoretical results for the low frequency branch. The theoretical curves were calculated, using the approximate density at the axial position at which the data was obtained, for the m = 0 mode. All of these results show a profile with a minimum on the axis (often very close to the predicted zero value), definite minima at r/a = 1 and maxima at r/a $\gtrsim$ .5. The data agrees remarkably well with the theory, considering the errors involved. There are only a few points on each plot that weren't able to fit the theory within the estimated experimental error. Any disagreement can satisfactorily be explained by the problems already presented in the description and calibration of this probe. The data was fitted against the calculated profile for m = 0. This was done because the m=0 profile matched the data much closer than the m = 1 profile. For comparison, the low frequency profile for m = 1 is shown in Figure 13. It is indeed similar to the m = 0 case in that it goes to zero at r = a and has a minima at r = 0. However, it does not go to zero on the axis (its minima here is $\approx$ 40% of its peak value) and the maxima are further from the center. The m = 0 calculation is a considerably better fit to the data than the m = 1 case.

Figures 67, 68, 69, and 70 show the results for the low frequency H_θ profiles. Again all these results agree remarkably well with the

FIGURE CAPTIONS

Fig. 63. H_r radial profile (arbitrary units) for f = 1480 MHz. The curve is the computed field profile for the Gould-Trivelpiece modes, m = 0.

Fig. 64. H_r radial profile for f = 1578 MHz, m = 0.

Fig. 65. H_r radial profile for f = 1685 MHz, m = 0.

Fig. 66. H_r radial profile for f = 1780 MHz, m = 0.

Fig. 67. H_θ radial profile for f = 1480 MHz, m = 0.

Fig. 68. H_θ radial profile for f = 1578 MHz, m = 0.

Fig. 69. H_θ radial profile for f = 1685 MHz, m = 0.

Fig. 70. H_θ radial profile for f = 1780 MHz, m = 0.

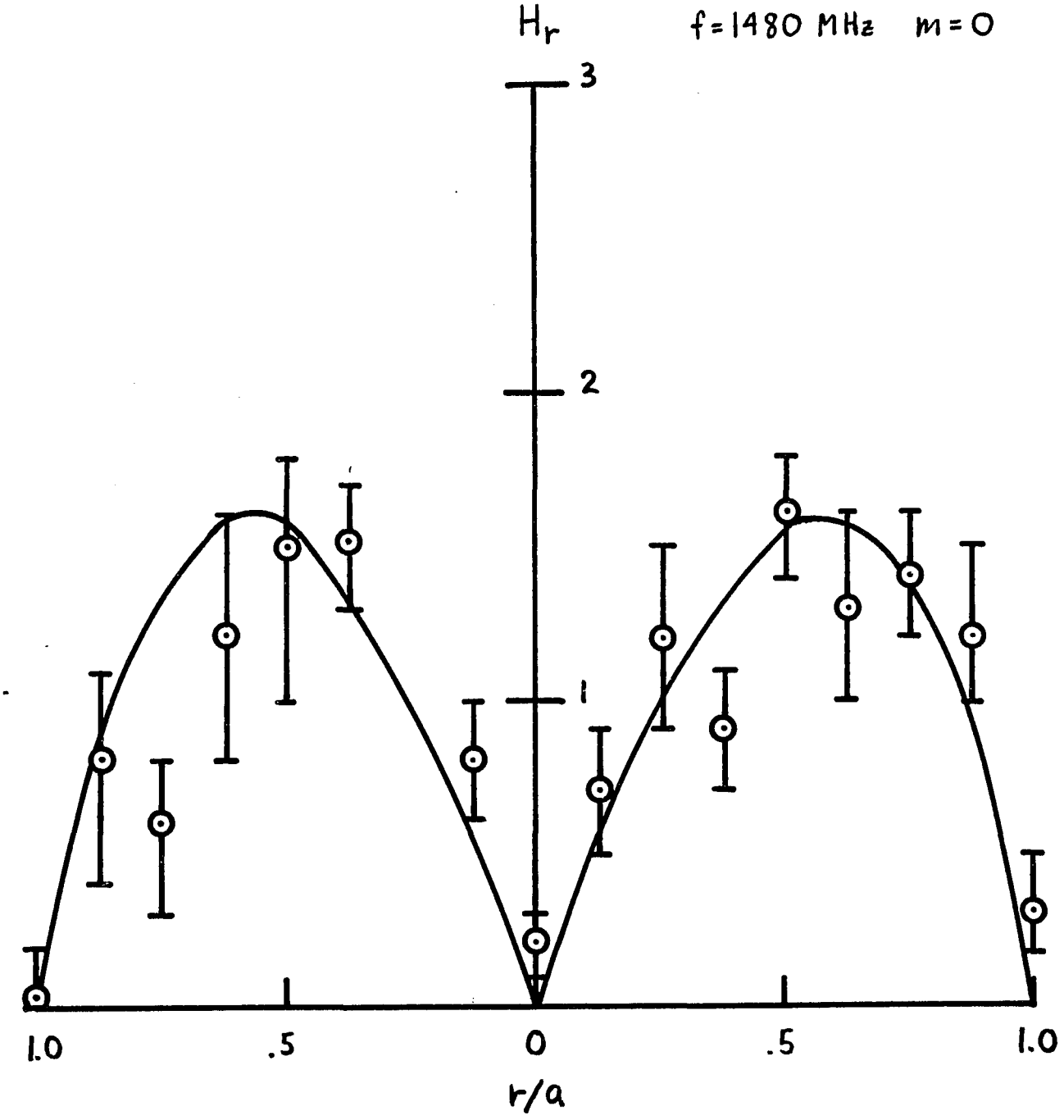

FIGURE 63

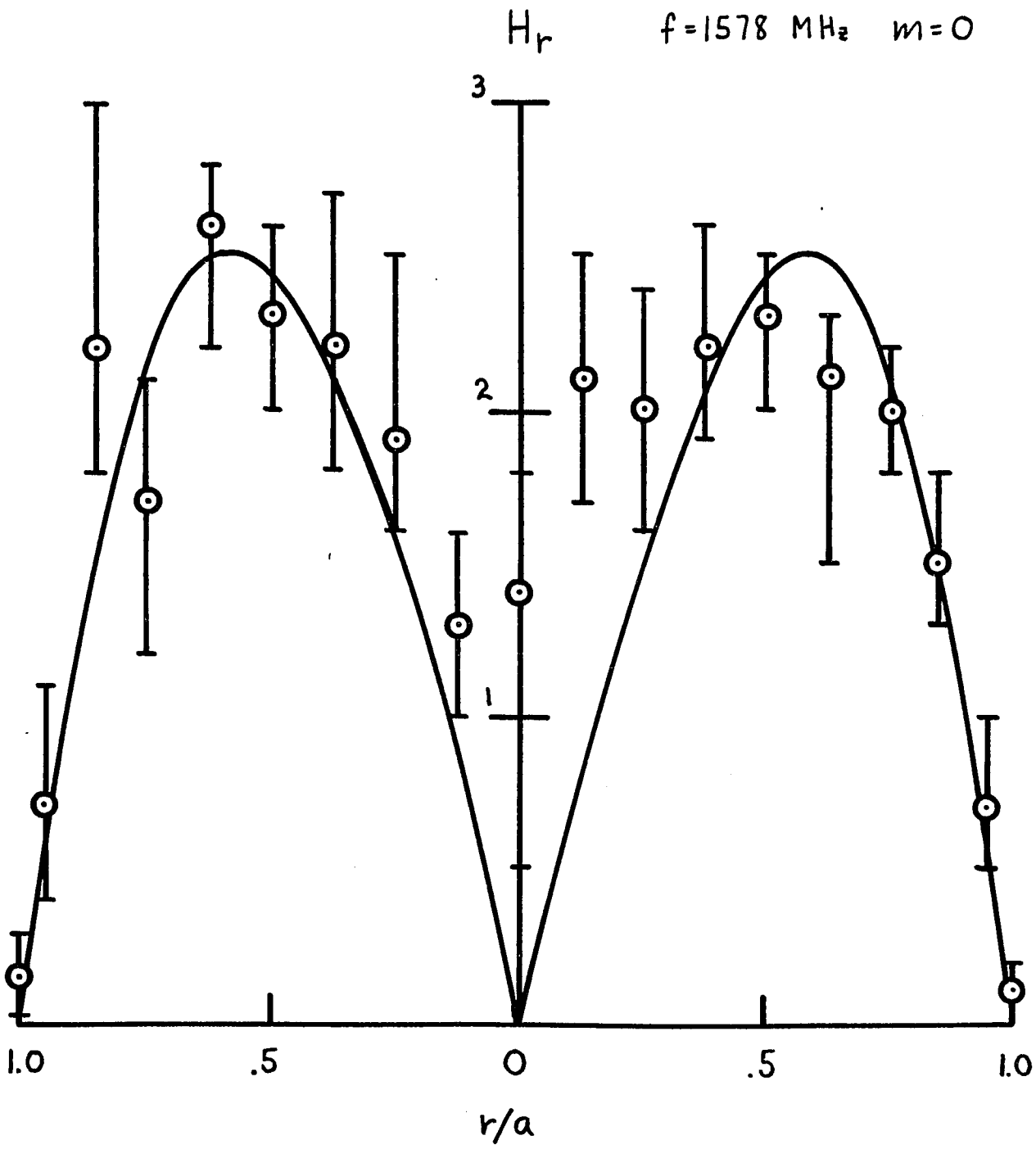

FIGURE 64

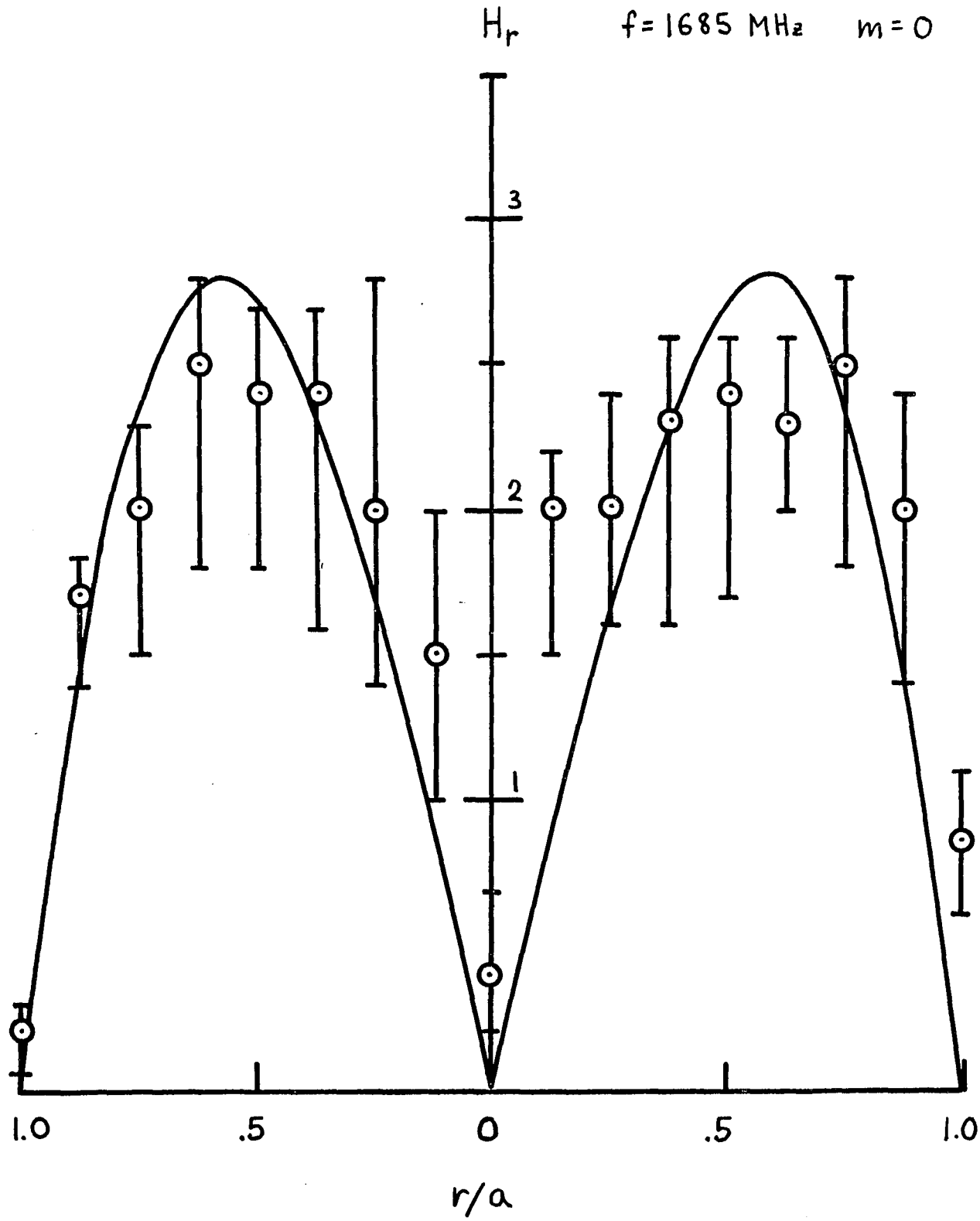

FIGURE 65

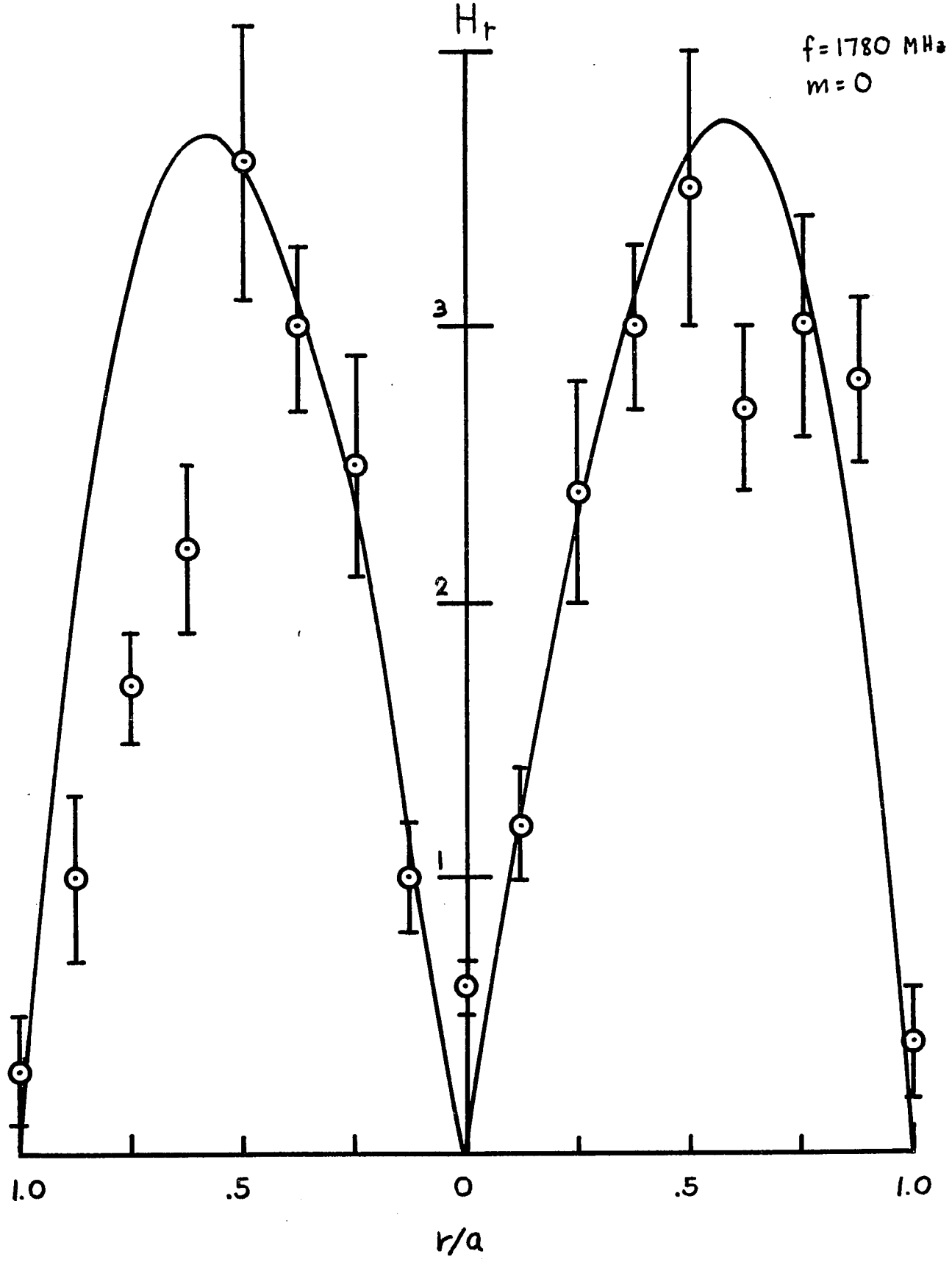

FIGURE 66

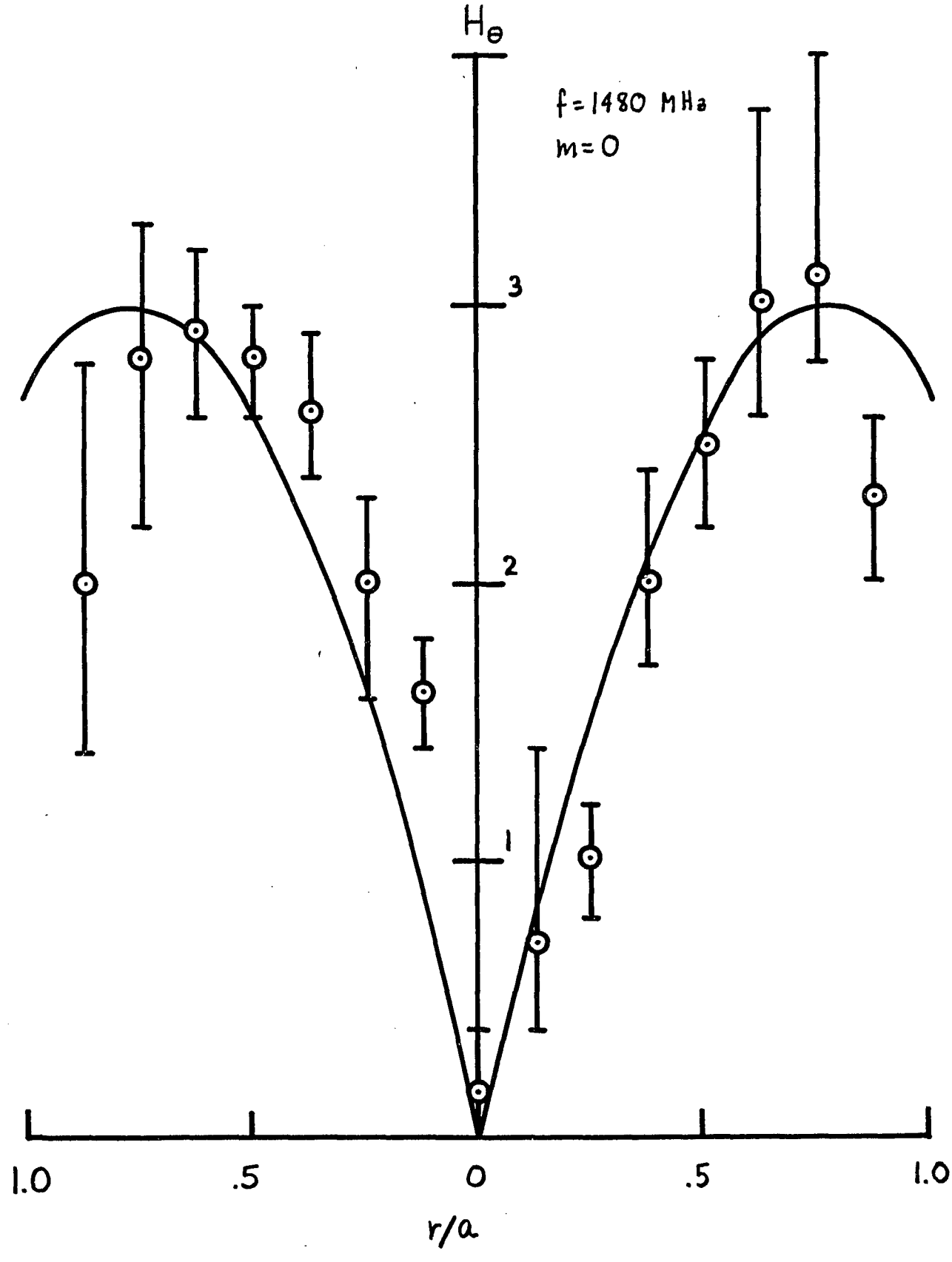

FIGURE 67

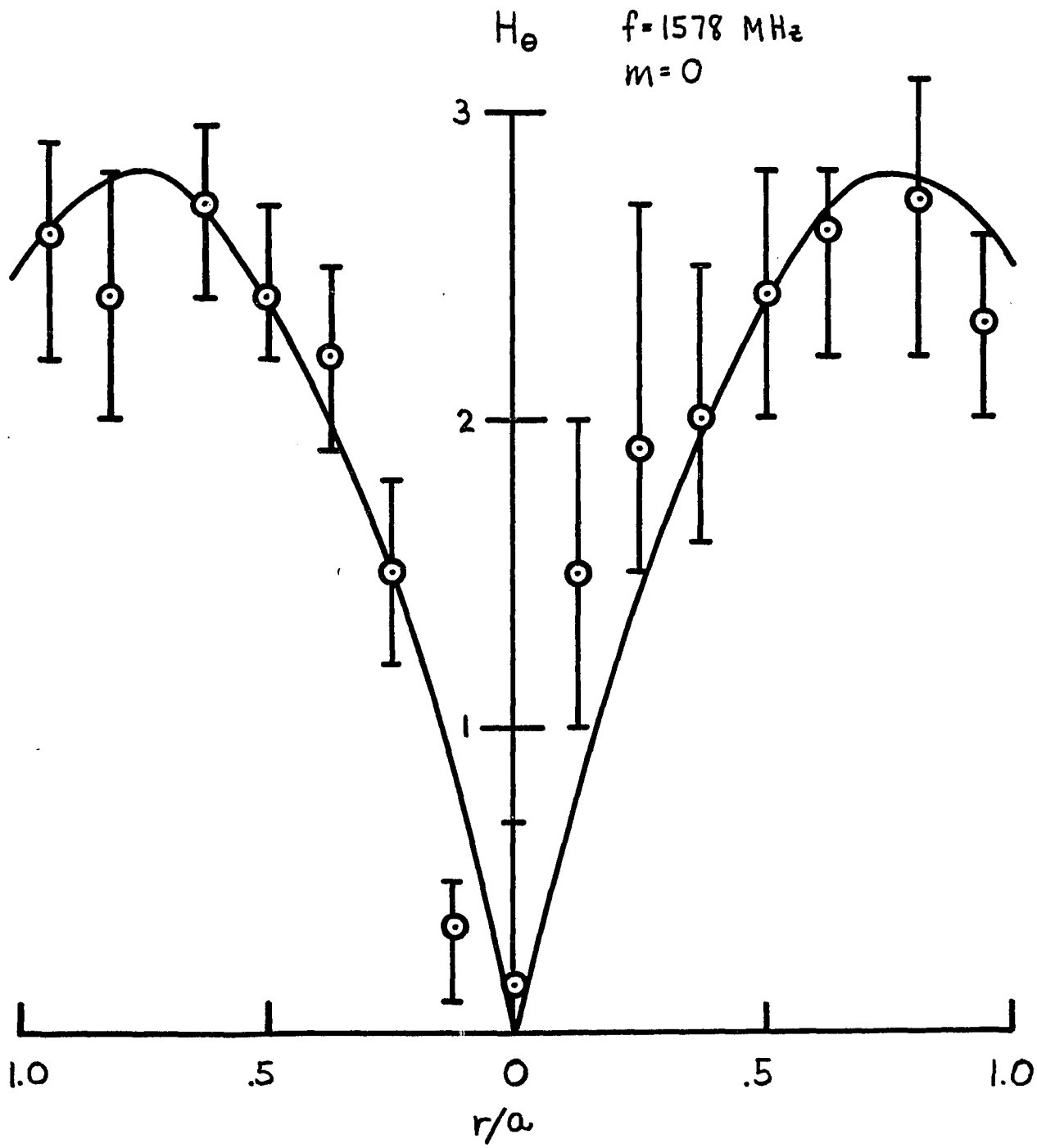

FIGURE 68

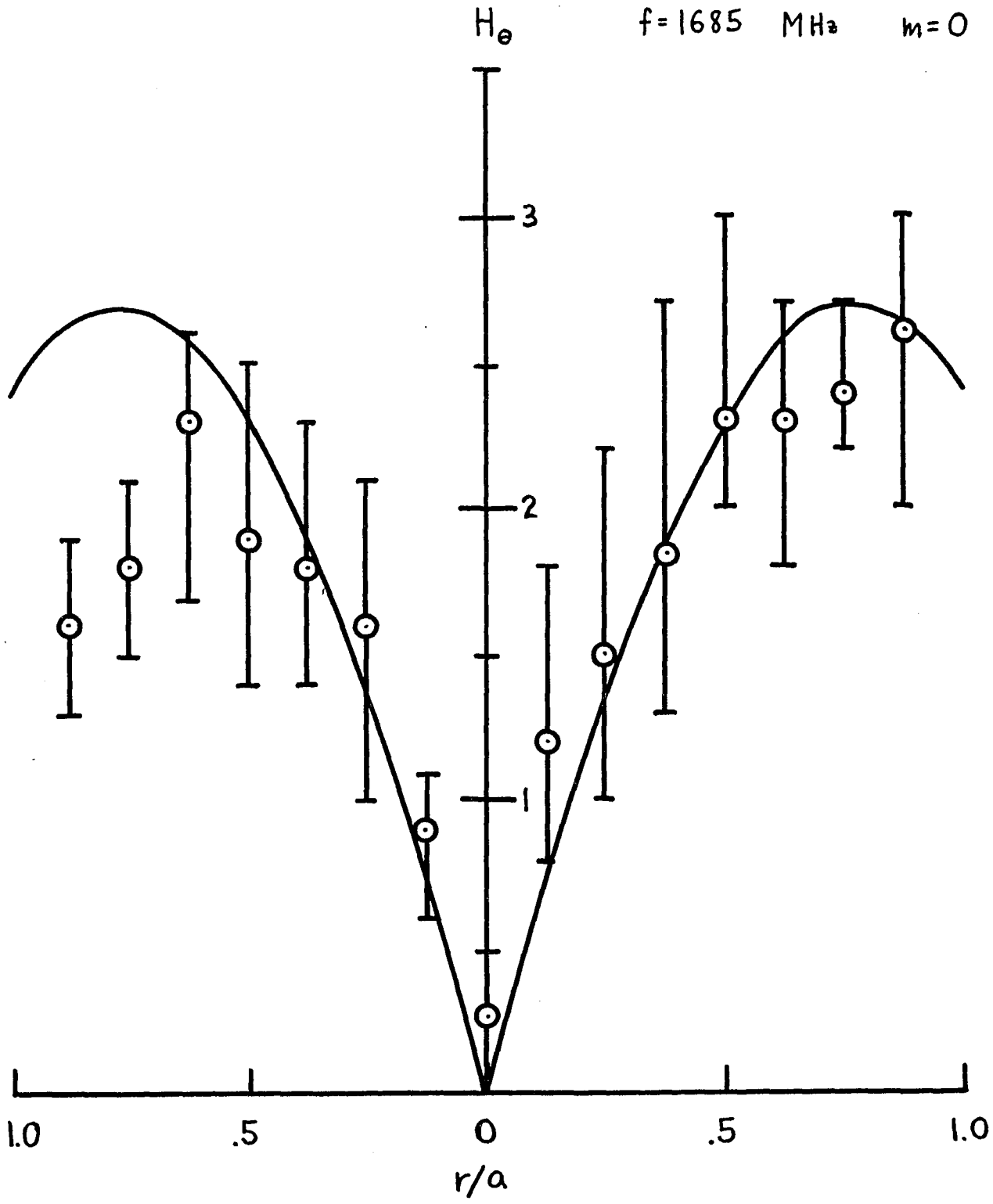

FIGURE 69

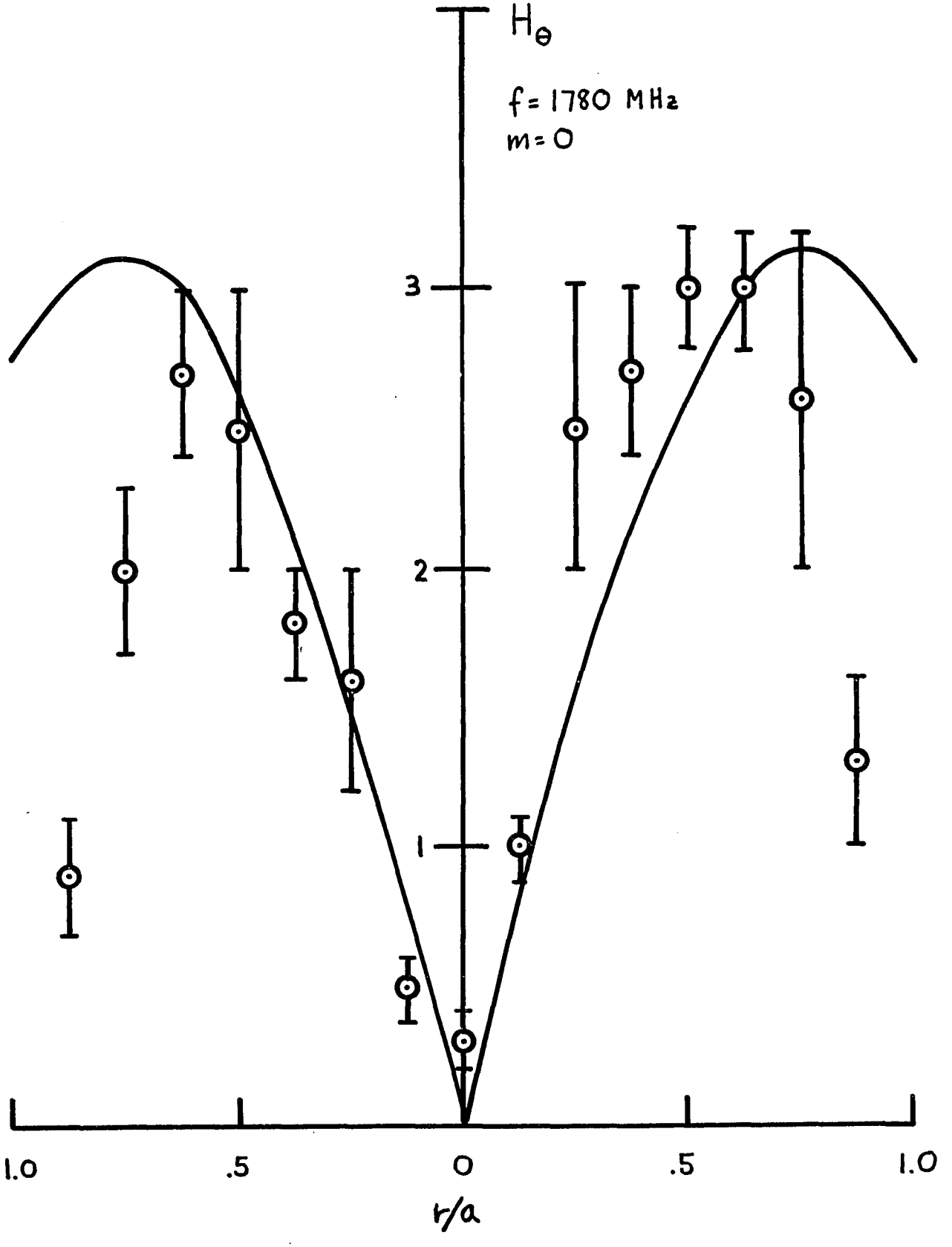

FIGURE 70

calculated profile for m = 0. They all exhibit minima on the axis (close to zero) and maxima at r/a $\approx$ .75. Again comparing with the other calculated profiles (see Figure 13), the m = 0 mode offers the best fit.

The H_r radial profiles for the high frequency case are shown in Figures 71 to 74. The agreement for these data are not nearly as good as the low frequency case. As was pointed out earlier, the wavenumber and hence the field profiles is strongly dependent upon density in this regime which make measurements considerably more difficult. This accounts for the large error bars represented in this data and the poorer agreement with the calculated profiles. The data is now compared with both the m = 1 (solid curve) and the m = -1 (dashed curve) high frequency calculation. It is seen that both calculated profiles exhibit nodes which is evident in the data, however, it is clear that only the m = 1 profile can fit the data with reasonable agreement. In contrasting the data for two trials, the result for f = 3980 MHz doesn't seem to correspond to any of the calculated profiles where on the other hand f = 4070 MHz gives good agreement. In order to demonstrate that the vacuum electromagnetic modes are also present, a profile was taken at z = -30cm where we essentially have a vacuum waveguide. Figure 75 does indeed show that the profile tends toward the familiar vacuum waveguide fields. (This measurement could not be done for the low frequency case because it is below the vacuum waveguide cutoff.)

FIGURE CAPTIONS

Fig. 71. H_r radial profile for f = 3780 MHz, m = 1, m = -1

Fig. 72. H_r radial profile for f = 3880 MHz, m = 1, m = -1

Fig. 73. H_r radial profile for f = 3980 MHz, m = 1, m = -1

Fig. 74. H_r radial profile for f = 4070 MHz, m = 1, m = -1

Fig. 75. H_r radial profile for f = 4070 MHz but at z = -30 cm (essentially vacuum). The curve is the computed field profile for the TE_{11} waveguide mode.

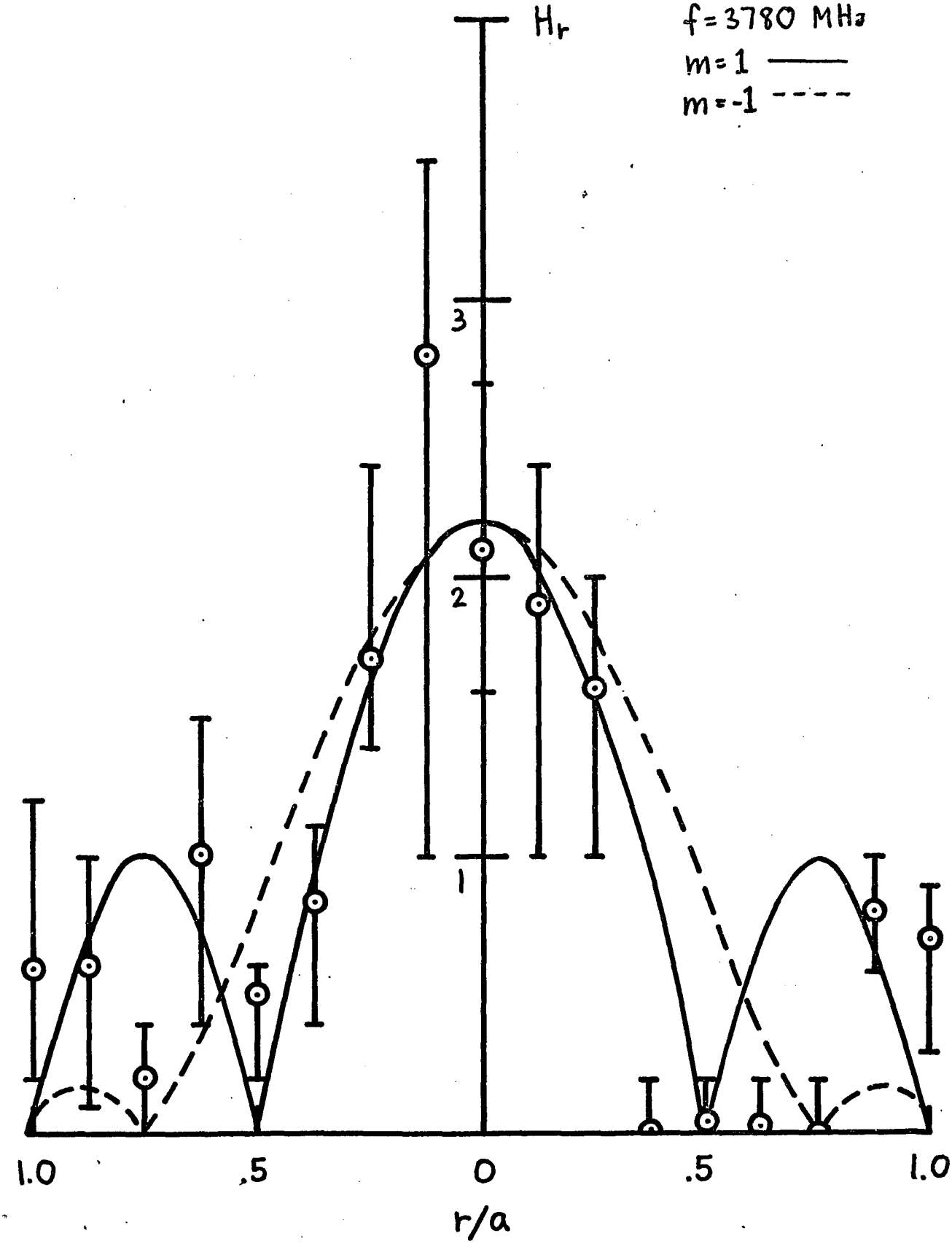

FIGURE 71

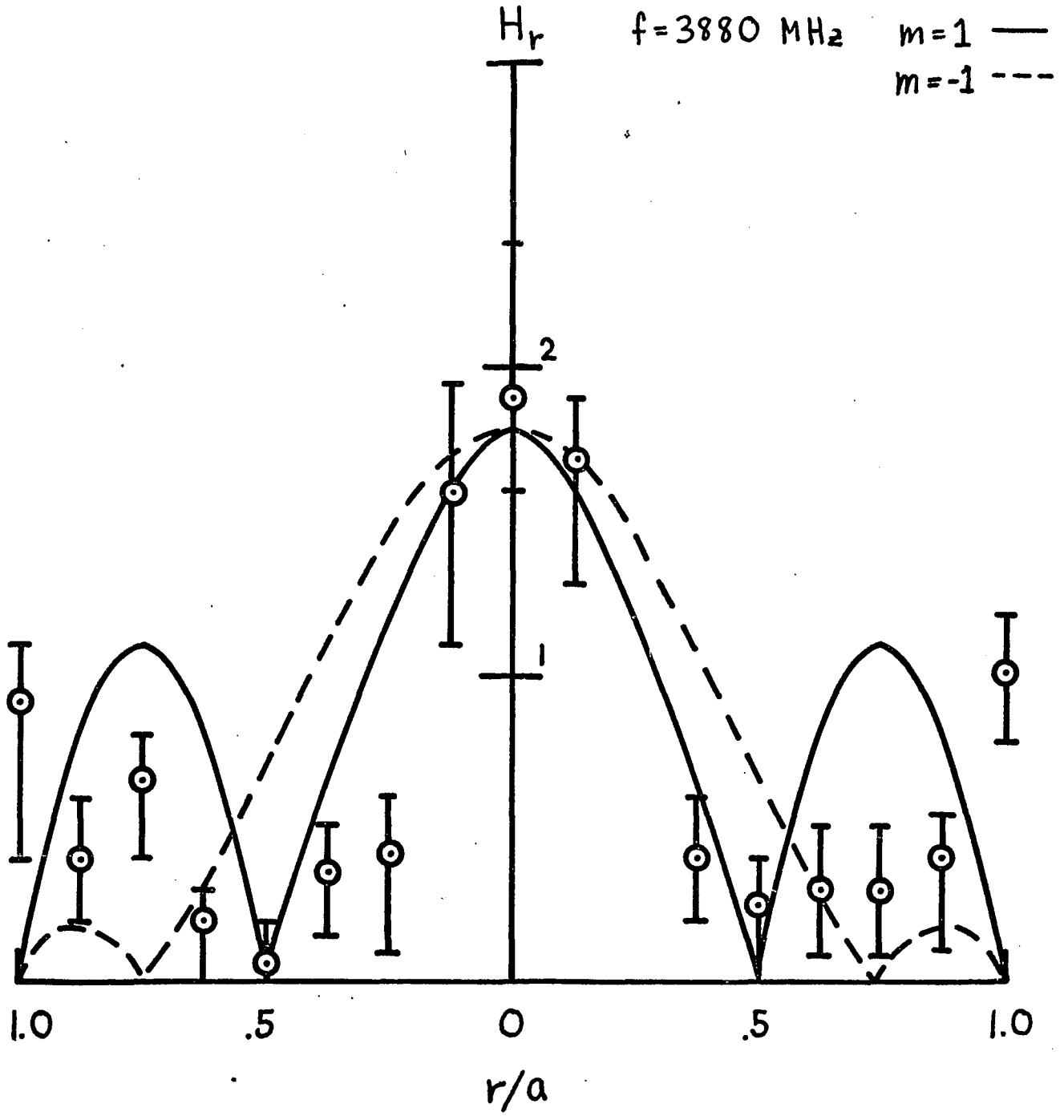

FIGURE 72

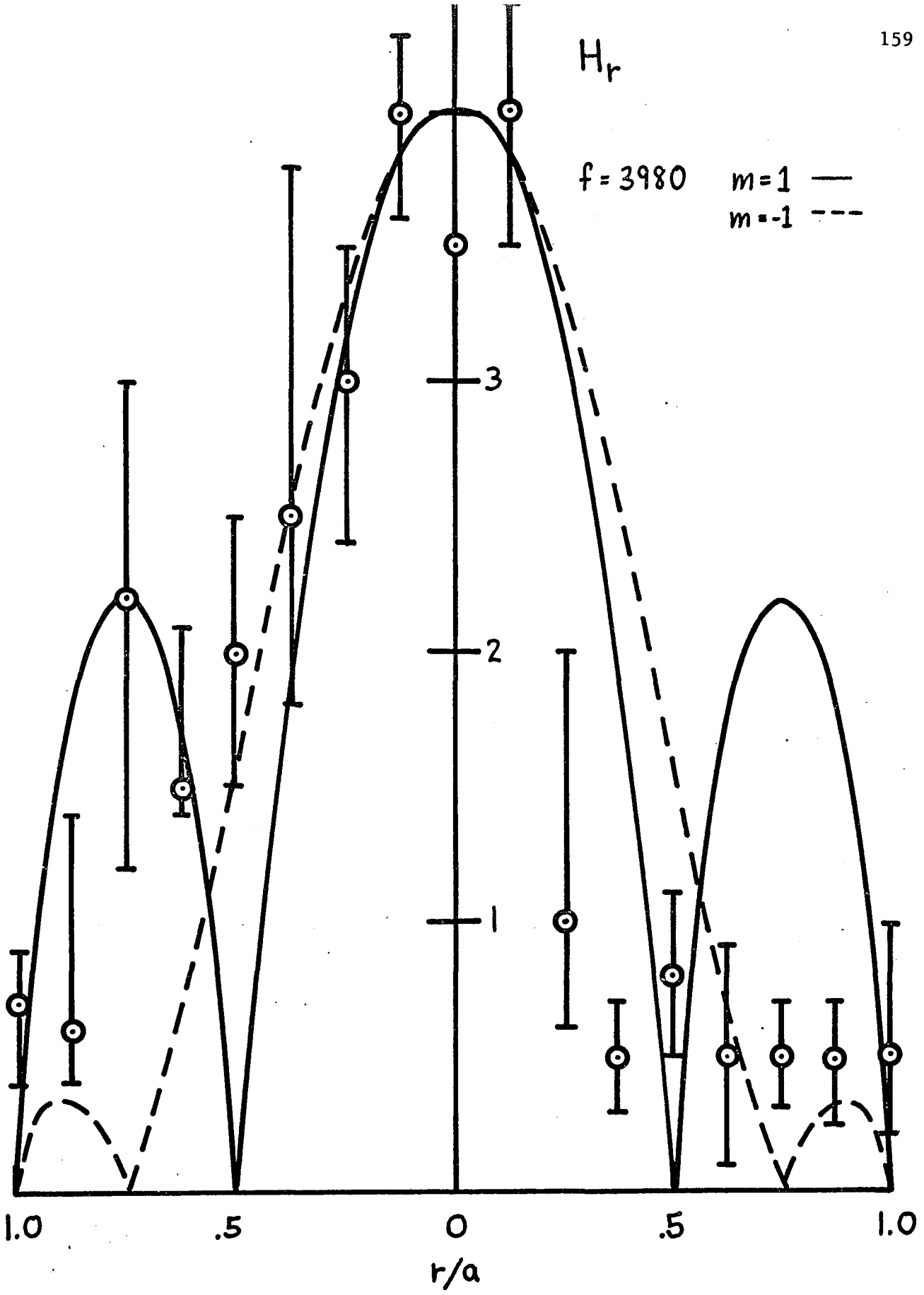

FIGURE 73

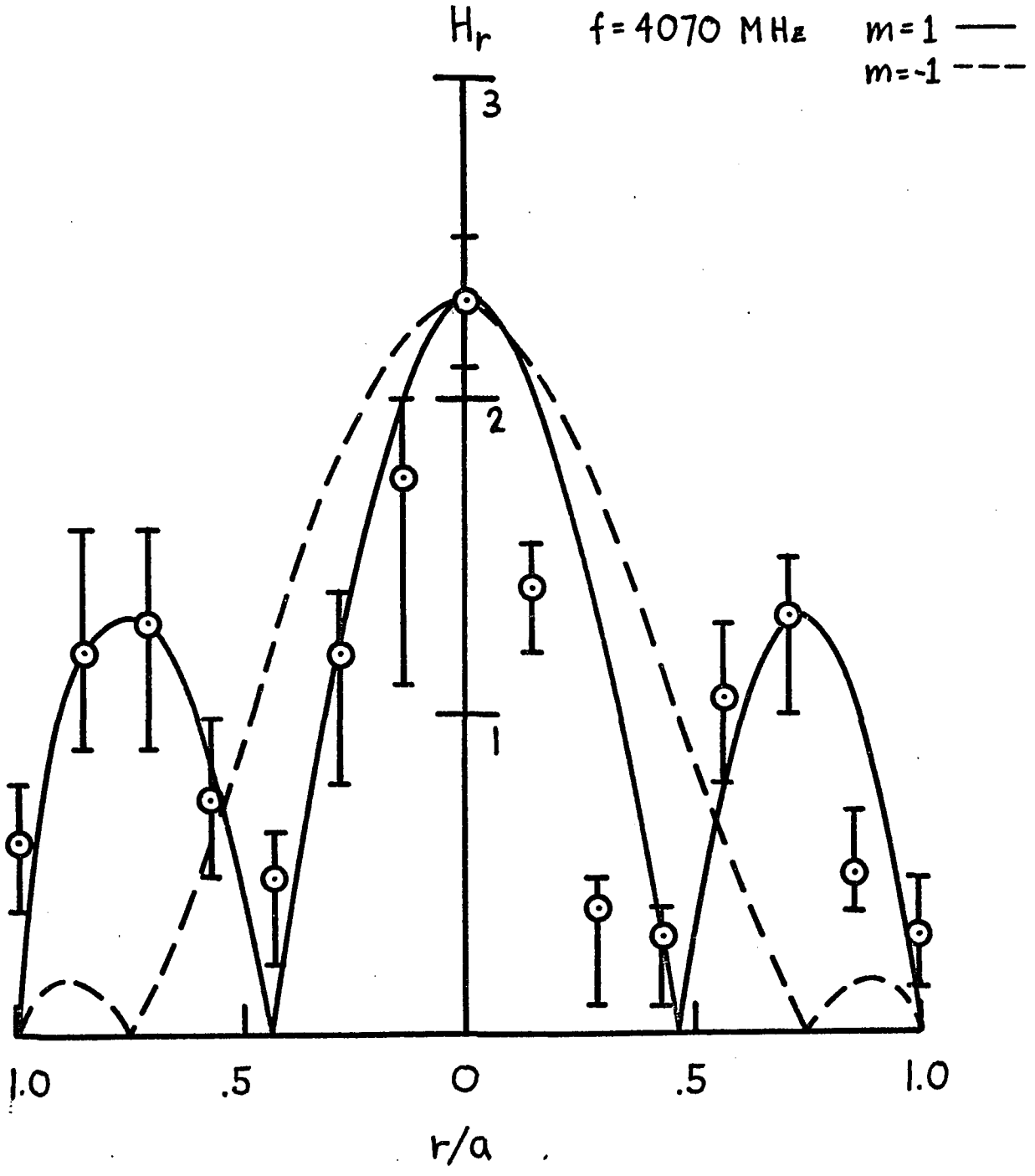

FIGURE 74

Finally we examine the H_θ profiles for the high frequency case (see Figures 76, 77, 78 and 79). The results here are poor. It was hoped to fit these data points to the m = 1 high frequency profile in order to be consistent with the other data, however, none of the results seem to approximate this calculated profile (see Figure 14), nor do they agree with any of the calculated profiles. It is noted however, that the data for f = 3880 MHz and f = 4070 MHz (Figures 77 and 79) do seem to exhibit well defined profiles, but again no resemblance to any of the calculated electrostatic plasma modes can be seen. Figure 80 again demonstrates that the well known vacuum guide fields appear when the probe is moved out of the plasma volume.

FIGURE CAPTIONS

Fig. 76. H_θ radial profile for f = 3780 MHz.

Fig. 77. H_θ radial profile for f = 3880 MHz.

Fig. 78. H_θ radial profile for f = 3980 MHz.

Fig. 79. H_θ radial profile for f = 4070 MHz.

Fig. 80. H_θ radial profile for f = 4070 MHz at z = -30 cm is shown along with the computed field profile for the TE_{11} waveguide mode.

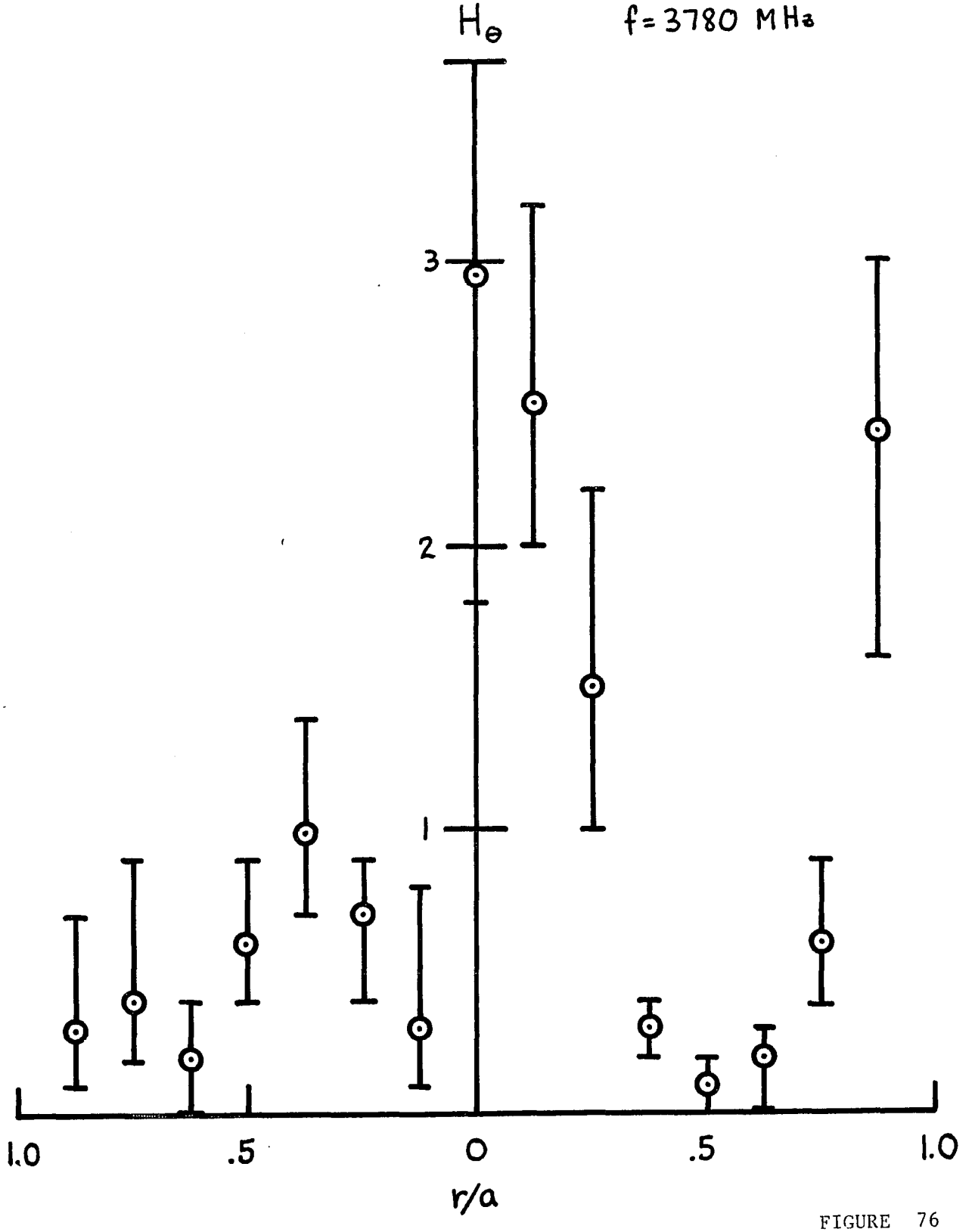

FIGURE 76

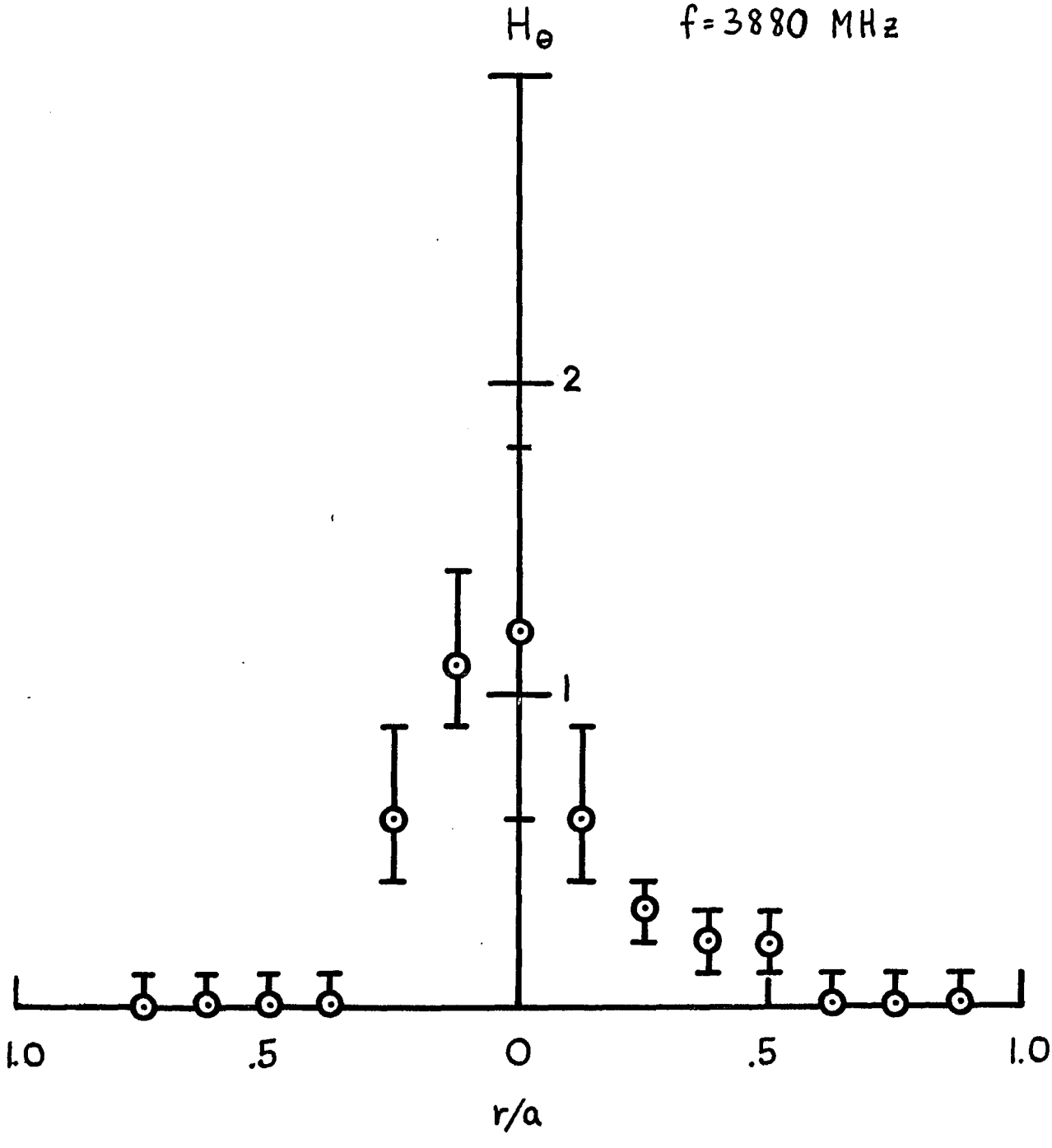

FIGURE 77

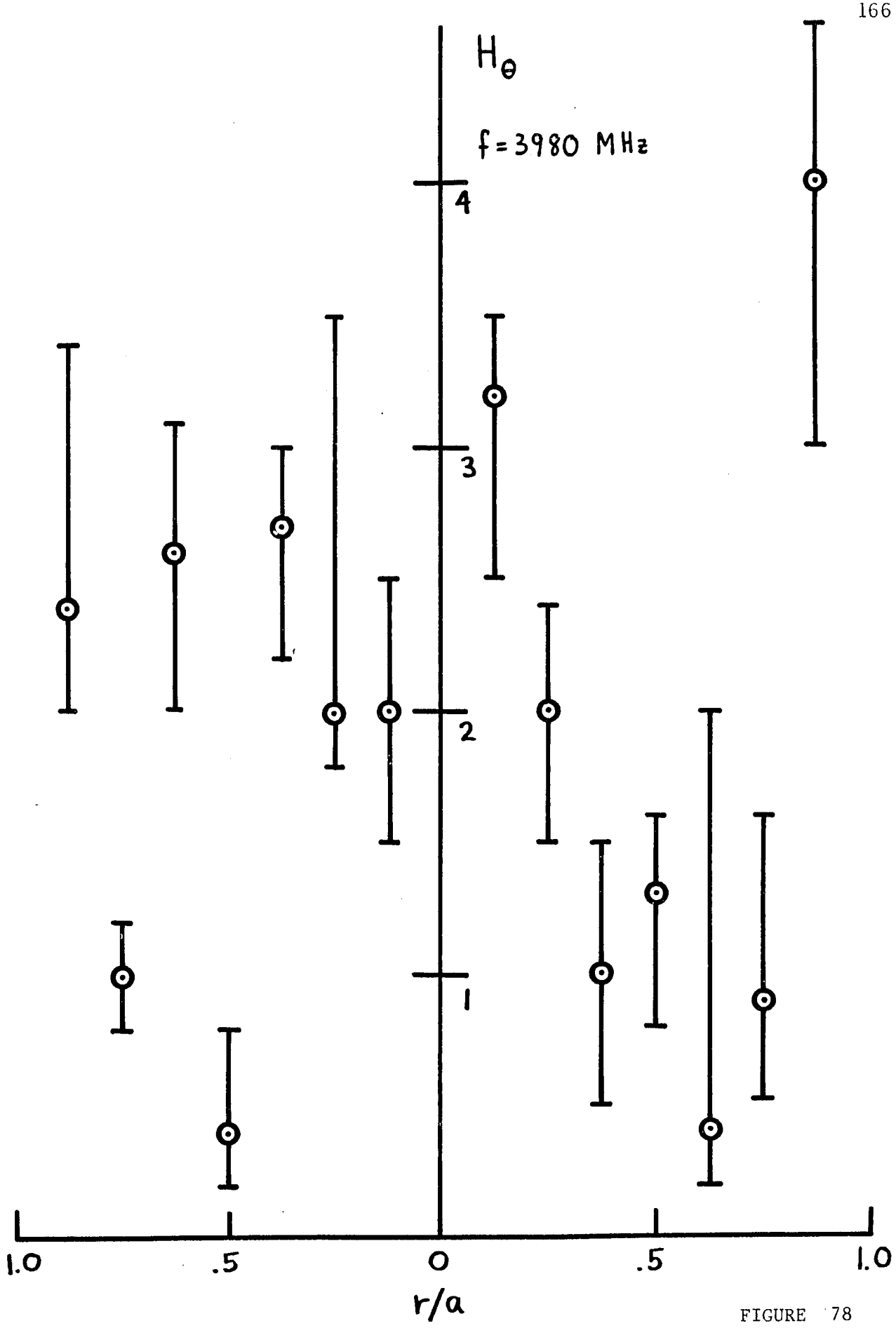

FIGURE 78

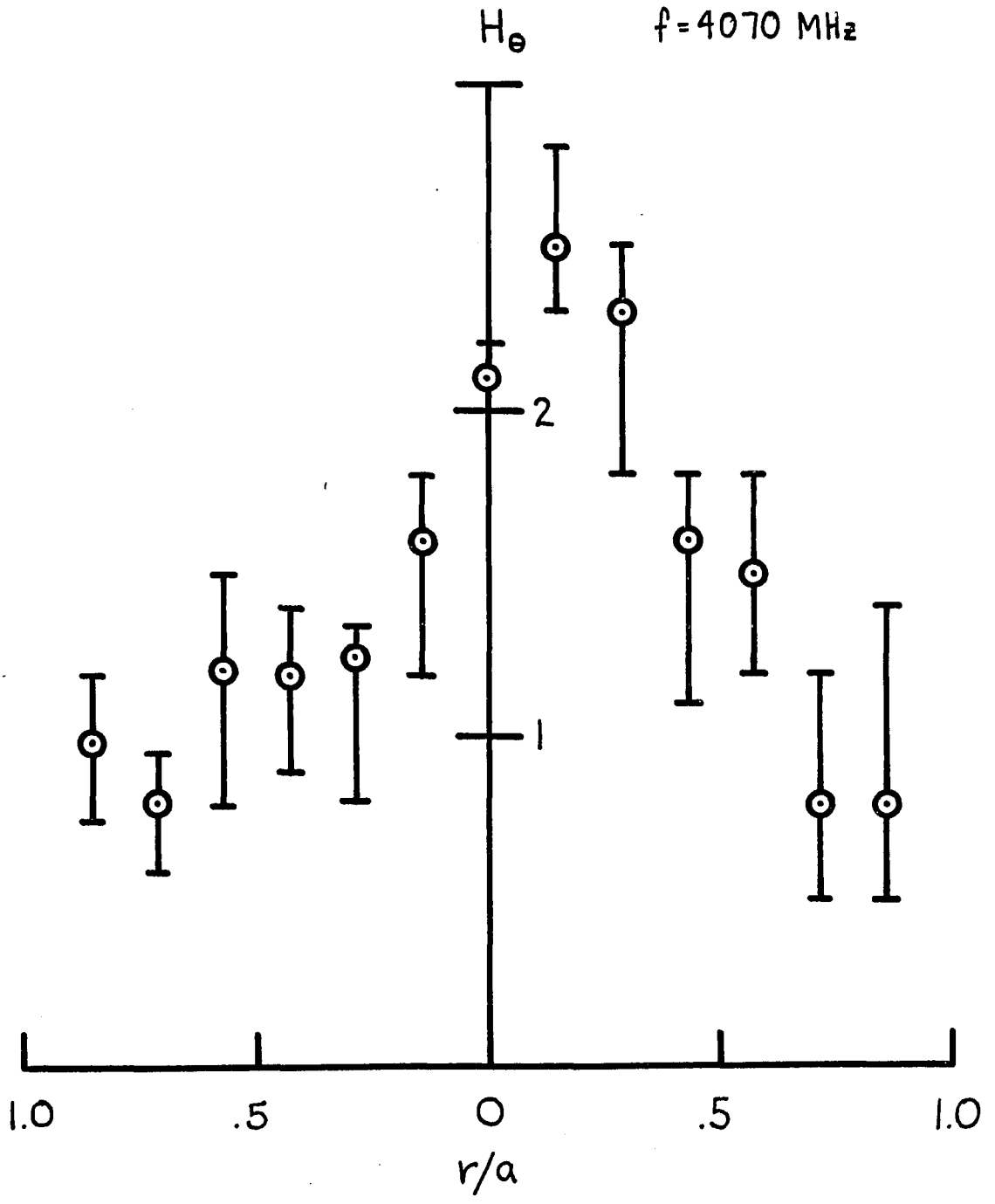

FIGURE 79

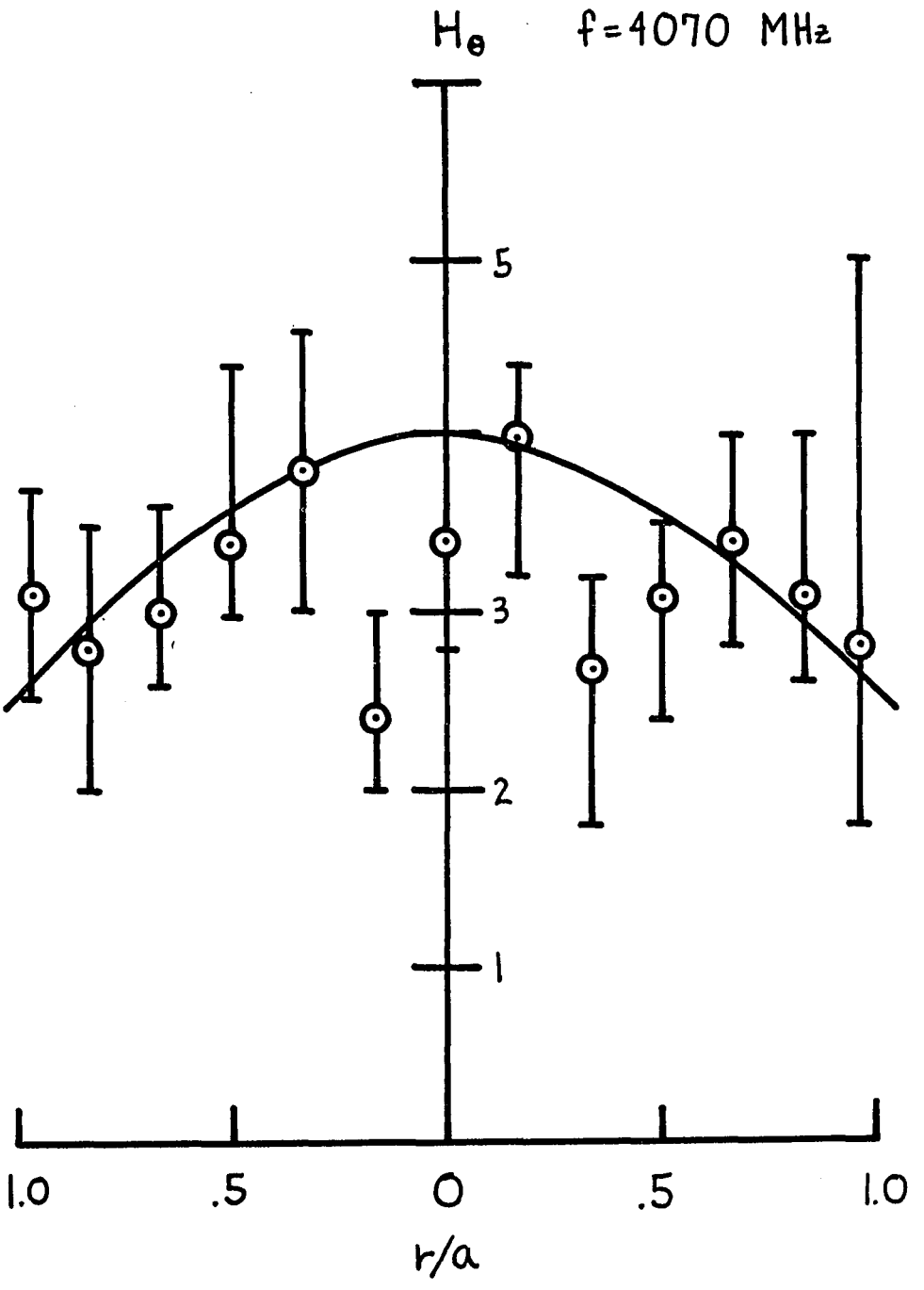

FIGURE 80

5 - REFERENCES

1. L.A. Ferrari, A. W. McQuade, and R. J. LaHaye, Physics of Fluids 17, 1785 (1974).

2. T. Stix, The Theory of Plasma Waves, McGraw-Hill Book Co. (1962) pp. 22-25.

3. A. W. Trivelpiece and R. W. G ould, Journal of Applied Physics 30, 1784 (1959).

V - CONCLUSIONS

Evidence has been presented that when the left hand wave is absorbed, it has in fact converted into electrostatic modes of the Gould - Trivelpiece [1] type. These modes have two branches, one below the electron cyclotron frequency and the other above the electron plasma frequency. It has been demonstrated from the wave magnetic field profiles that the low frequency branch has an azimuthal order of m = 0 while the high frequency branch has an order of m = +1. The incident left wave also has an order of m = +1; therefore, it is seen that the azimuthal order selection rule [2] is obeyed.

In designing the apparatus for these experiments, care was taken to insure that multiple waveguide modes [3] did not exist as was possible with other waveguide propagation experiments. [4] The input frequency of f = 2.45 GHz and the waveguide radius of a = 4.39 cm was chosen so that only the dominant H_{11} mode could propagate in the vacuum guide. This mode has a cutoff frequency of 2.00 GHz while the next highest mode (E_{10}) has a cutoff frequency of 2.62 GHz. Unfortunately, the existence of a single mode of propagation can only be guaranteed for the vacuum guide.

As was seen, the left wave at 2.45 GHz excites modes having frequencies both above and below the vacuum cutoff frequency of 2.00 GHz. The modes in the high frequency branch (3.7 - 4.1 GHz) are capable of propagating in the empty guide and thus they can propagate

out of the plasma volume. The modes in the low frequency branch (1.4 - 1.9 GHz) however are not free to propagate out of the plasma region because they are below the vacuum cutoff frequency. These modes are thus "trapped" in the plasma volume.

Since these trapped modes are confined to exist only in regions with sufficiently high plasma density, they act similarily to cavity modes; that is, a standing wave pattern is set up within the plasma volume and the oscillations build in amplitude until an equilibrium is reached between the input microwave power and the ohmic heating of the plasma. To verify this, the classical Spitzer[5] resistivity of the plasma was calculated in order to compare the rate of ohmic heating with the incident power. It was found that the measured electric field amplitude within the plasma is approximately 2.6 v/m. This value agrees reasonably with a calculated field amplitude of 1.6 v/m which would be the electric field amplitude commensurate with the incident microwave power. It is thusly suggested that ohmic heating of the plasma due to the trapped plasma modes is a viable mechanism to explain the observed absorption of the left wave and the subsequent heating of the plasma.

1 - REFERENCES

1. A. W. Trivelpiece and R. W. Gould, Journal of Applied Physics 30, 1789 (1959).

2. D. Phelps, G. Van Horen, N. Rynn, Physics of Fluids 16, 1078 (1973).

3. L. A. Ferrari, Plasma Physics 13, 257 (1970).

4. I. R. Gekker and O. V. Siyukhin, JEPT 9, 243 (1969).

5. L. Spitzer, Physics of Fully Ionized Gases, Second Revised Addition, Interscience Publishers (1962) pp. 136-143.